Scattering processes in quantum dot devices with the example of an amplifier

Dissertation

presented by

Sabine Dommers

to the Institute of Physics of

technische universität
dortmund

Dortmund, September 2009

Contents

List of publications

Publications and conference contributions based on this work:

Scientific papers

1. S. Dommers, V.V. Temnov, U. Woggon, J. Gomis, J. Martínez-Pastor, M. Laemmlin and D. Bimberg, *Complete ground state gain recovery after ultrashort double pulses in quantum dot based semiconductor optical amplifier*, Appl. Phys. Lett. **90**, 033508 (2007).

2. J. Gomis-Bresco, S. Dommers, V. V. Temnov, U. Woggon, M. Laemmlin, D. Bimberg, E. Malic, M. Richter, E. Schöll and A. Knorr, *Impact of Coulomb Scattering on the Ultrafast Gain Recovery in InGaAs Quantum Dots*, Phys. Rev. Letters. **101**, 256803, Dec 2008.

3. J. Gomis-Bresco, S. Dommers, V.V. Temnov, U. Woggon, J. Martínez-Pastor, M. Laemmlin and D. Bimberg, *InGaAs Quantum Dots Coupled to a Reservoir of Nonequilibrium Free Carriers*, IEEE J. Quantum Electron. **45**, 1121 2009

4. J. Gomis-Bresco, S. Dommers, V. V. Temnov, U. Woggon, M. Laemmlin, D. Bimberg, E. Malic, M. Richter, E. Schöll and A. Knorr *InGaAs quantum dot population and polarisation dynamics for ultrafast pulse train amplification*, 2008 CONFERENCE ON LASERS AND ELECTRO-OPTICS and QUANTUM ELECTRONICS and LASER SCIENCE CONFERENCE, VOLS 1-9 Book Series: IEEE Lasers and Electro-Optics Society (LEOS) Annual Meeting Pages: 3599-3600 Published: 2008

Contribution to conferences (own presentation)

1. *Ultrafast carrier dynamics in an InAs quantum dot amplifier emitting at 1.3 μm* Oral contribution at "The Spring Meeting of the German Physical Society" (DPG 2005), Berlin, Germany, March 2005

2. *Linewidth enhancement factor of an InAs quantum dot amplifier emitting*

at 1.3 μm Poster contribution at workshop of "Self-Assembled semiconductor Nanostructures for new Devices in photonics and Electronics (SANDiE-Network of Excellence) 05", Kühlungsborn, Germany, June 2005

3. *Operating conditions of a LCD-based pulse-shaper producing pulse sequences for coherent control* Oral contribution at workshop of "GK 726: Materials and concepts for quantum information processing", Riezlern, Germany, September 2005

4. *Linewidth enhancement factor and ultrafast dynamics of InAs qunatum dot amplifiers emitting at 1.3 μm* Oral contribution at workshop of "Self-Assembled semiconductor Nanostructures for new Devices in photonics and Electronics (SANDiE-Network of Excellence) 06", Berlin, Germany, January 2006

5. *THz operation of semiconductor optical amplifiers* Oral contribution at "SANDiE Workshop: Growth, Electronic and Optical Properties of Low-Dimensional Semiconductor Quantum Structures", Berlin, Germany, January 2007

6. *THz operation of semiconductor optical amplifiers* Poster contribution at "The Spring Meeting of the German Physical Society" (DPG 2007), Düsseldorf, Germany, March 2007

7. *Gain dynamics after ultrashort pulse trains in quantum dot based semiconductor optical amplifiers* Oral contribution at "Conference on Lasers and Electro-Optics" (CLEO/QELS 2007), Baltimore, USA, May 2007

8. *Amplification of coherent pulse trains using quantum dot based SOAs* Oral contribution at workshop of "GK 726: Materials and concepts for quantum information processing", Riezlern, Germany, September 2007

9. *Amplification of ultrafast trains in InGaAs quantum dot based SOAs* Poster contribution at conference "Nonlinear Optics and Excitation Kinetics in Semiconductors" (NOEKS08), Klink/Müritz, Germany, June 2008

Motivation

During the last decade quantum dot based devices and their application in optical communication technology have made great progress. In particular semiconductor lasers and amplifiers have entered the focus of interest. They were theoretically predicted in 1961 [1] and realized technically the year after [2]. Today semiconductor lasers are found in several every-day devices like CD- and DVD- players, hard drives or laser printers. For the further development of these lasers improved methods for creating semiconductors and semiconductor based devices play a great role. In the past the effect of quantum confinement allowed to decrease the dimensions of the active material systematically. One expects best performance of the current zero-dimensional quantum dots (QDs). A high gain, a low and temperature-independent threshold current density and discrete energy levels are their advantages.

In this work the ultrafast optical characteristics of quantum dot based devices are studied regarding GHz application using advanced pump-probe techniques. Our device consists of InAs quantum dots embedded in a wave guiding diode-structure. This quantum dot amplifiers groundstate emits at $1,3\mu$m, one of the wavelength for communication applications. To measure phase and amplitude of the signal at the same time all experiments were done with heterodyne technology. The gain dynamics of the system where measured in dependence of temperature, bias current and signal intensity to model several working conditions.

To clarify if devices like the ones studied during this work are suited to be used in modern communication technology an additional point is of importance.

The question is if the relaxation times of the ground state are provided also for high pulse rates. Here it becomes more important which processes dominate the refilling of the ground states and how fast or efficient they are than how fast the ground state itself is refilled. Customizing our pump-probe setup to run with femtosecond pulse trains (of up to four pulses) to study directly the behavior of the ground-state recovery after GHz operation (up to 1 THz) and choosing the device carefully (e.g. p-doping and quantum dot in a well structure) we achieved a deeper understanding of the refilling processes. To anticipate some of the results we found direct carrier capture from the surrounding 2D-reservoir build by the well and wetting layer to be the guiding process in contradiction to a cascade-like recovery that involves the excited state proposed some time ago by theory [3].

The experimental conclusions are supported by two different models. Once a model using optical Bloch equations and microscopically calculated Coulomb scattering rates and second a rate equation model are compared to the measure-

ments with good agreement.

This work is structured in five chapters with the first one centering on the theoretical background, the explanation of the sample and the experimental implementation. It starts with an introduction of semiconductors and nanostructures in general, goes on with the description of semiconductor optical amplifiers and the heterodyne pump-probe setup and ends with providing the theoretical tools used in the course of this thesis.

The second chapter introduces our way of implementing pulse trains. It starts with the description of general pulse shapers, focuses at second on our first approach using a liquid crystal based phase mask to create pulse trains and ends with the final solution based on a two-stage Michelson interferometer.

In the third chapter first results are presented showing the usability of quantum dot amplifiers for high-speed applications. E.g. the complete gain recovery of a double pulse is shown here.

The fourth chapter includes an advanced model based on optical Bloch equations including microscopically calculated Coulomb scattering rates. The interpretation leads to a coupled dynamics of population and polarization.

A rate equation model is introduced in chapter five for understanding the mostly population dependent section of the gain recovery. This model takes propagation effects of the device into account.

I will conclude with a summary and outlook showing possible applications how this work can help to create more powerful optical devices.

Chapter 1

Introduction to experimental and theoretical fundamentals

All experiments performed in this work deal with a device that is a quantum dot based semiconductor optical amplifier. This chapter explains why especially InAs quantum dots in a waveguide were chosen to perform them. In addition all basics necessary to understand the experimental methods, the setup and the models will be described.

The first section will deal with semiconductors and the special terminology used for describing them. After that the advantages of quantum dots in comparison to other semiconductor nanostructures are clarified.

In the third section the device itself is focused, the Semiconductor Optical Amplifier (SOA) and its characteristics. First the design will be discussed then the optical characteristics.

The performed experiments are described in detail in the fourth section of this chapter. Both the technical setup and the used methods will be explained. This sections is completed with a first characterization of the sample.

At last I introduce the theory necessary for following the models used in chapter 4 and 5 of this thesis.

1.1 Semiconductors

Talking about semiconductors a special class of material is addressed whose electrical conductivity lies between the one of metal and insulator. But more interesting for our purpose is that some semiconductors are well suited for using them in optical telecommunication networks provided they are processed accordingly. E.g. quantum dot lasers have proved to be appropriate to achieve a telecommunication wavelength of 1.3 μm at room temperature (300 K) [4, 5]. They show a small and temperature independent threshold current density [6, 7] and a high amplification factor [8]. In this section the structure of semiconductors in general and in special of InAs, the material used for our device, are explained.

1.1.1   Crystal
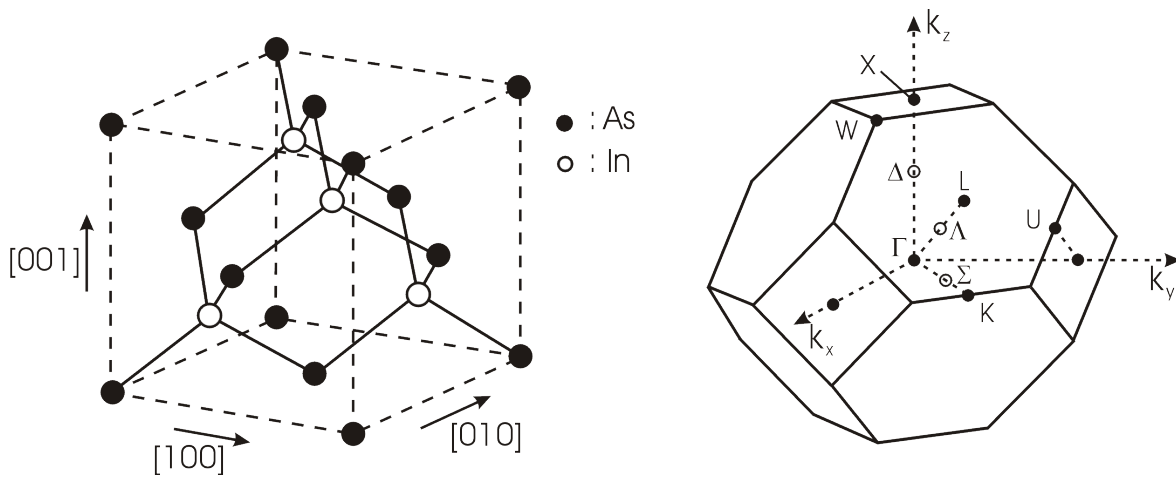
Figure 1.1:   Left: Unit cell of the Bravais lattice of a zinc blende structure, e.g. of InAs. Right: First Brillouin-zone of the reciprocal zinc blende lattice.

Our semiconductor has a crystalline zinc blende structure. "Crystal" refers to a material that has a periodic structure. The structure of InAs for instance is shown in figure 1.1(left). InAs has a diatomic base, i.e. its unit cell contains two different atoms indium and arsenic. Zinc blende structure describes a configuration in which there are two fcc (face centered cubic) lattices shifted against each other by a quarter of the body diagonal (see fig. 1.1). The lattice constant of InAs, i.e. the edge length of its unit cell, is $a = 0,606$nm.

Taking a closer look at the first Brillouin zone of the reciprocal lattice there are points of special geometry, marked in fig. 1.1 (right). In the further course of the consideration the Γ-point, i.e. the center of the Brillouin zone, is of special interest.

1.1.2   Band model

Figure 1.2: a) Band structure of InAs, calculated with the method of non-localized pseudopotentials [9]. b) Parabolic approximation of the band structure in the environment of the Γ-point.
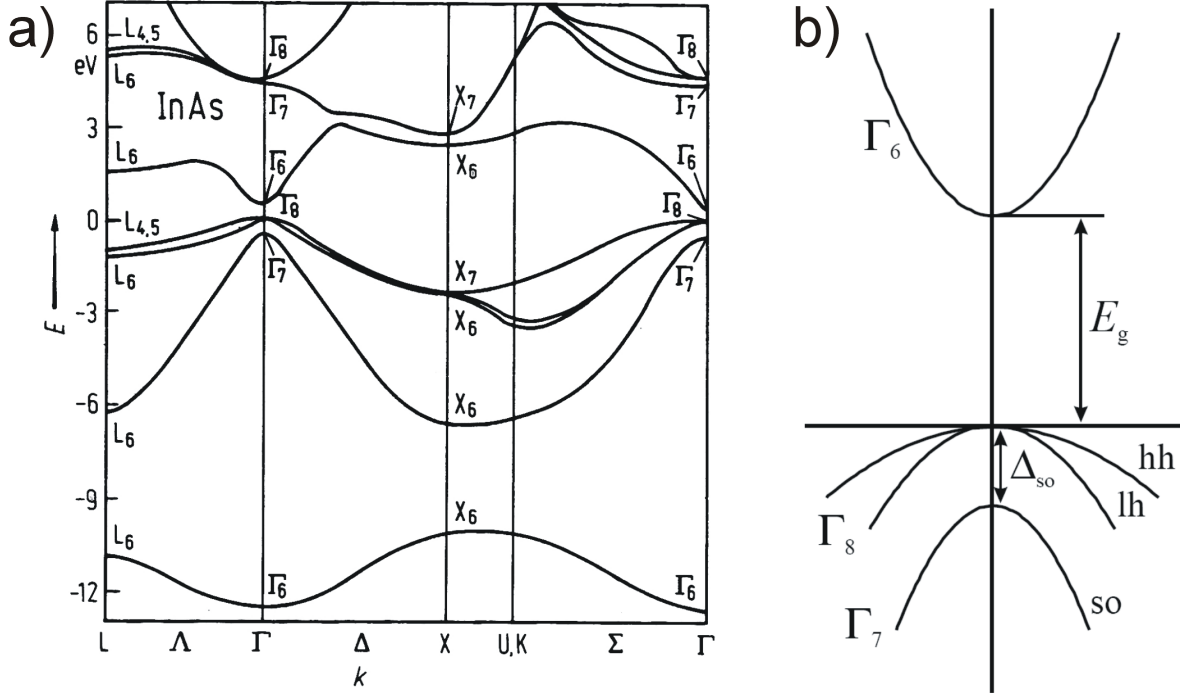
In a quantum mechanical approach to describe a crystal, ionic nuclei and electrons are represented by wavefunctions, with Hamilton operators accounting for the interaction between them. In the one-electron-approximation the ionic bodies are set to their stationary values. The effect that the ions and the electrons of the inner shell have over the external electrons is calculated assuming a periodic lattice potential U($\mathbf{r}$), whose influence on a single electron is observed. The Hamilton operator is:

$$H = -\frac{\hbar^2}{2m_0}\nabla^2 + U(\mathbf{r}) \tag{1.1}$$

where m_0 is the mass of the free electrons.

The corresponding Schrödinger equation is:

$$H\psi_{n\mathbf{k}}(\mathbf{r}) = \mathbf{E}_{n\mathbf{k}}\psi_{n\mathbf{k}}(\mathbf{r}) \tag{1.2}$$

where $\mathbf{k}$ is the wave vector and $\psi_{n\mathbf{k}}(\mathbf{r})$ is the wave function. The energy eigenvalues with equal quantum number n that belong to $\psi_{n\mathbf{k}}$ are combined to so called energy bands.

In fig. 1.2 a) the energy bands of InAs are shown schematically. One differs between valence- and conduction-bands. With increasing energy the valence-
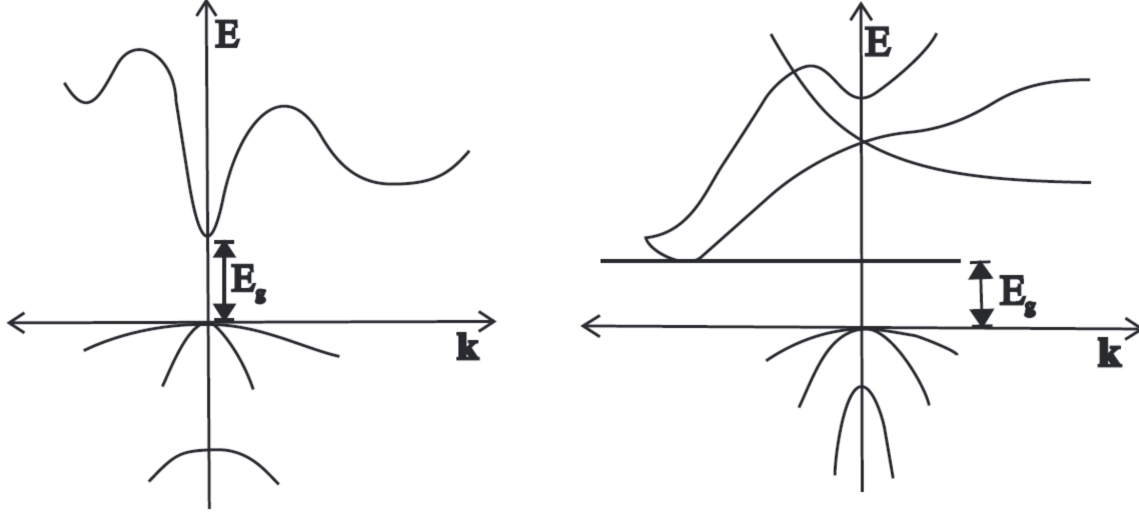
Figure 1.3: Band structure of a direct semiconductor (e.g. InAs) (left) in comparison with the band structure of an indirect semiconductor (e.g. Si)(right).

bands are filled with electrons following the Pauli-principle. The highest valence-band is the last completely filled and the lowest conduction-band is the first emptied band.

The energetic distance between the highest valence- and the lowest conduction-band is a characteristic feature of every semiconductor. It is called energy gap E_g. It is important to distinguish between direct and indirect semiconductors. InAs is a direct semiconductor. It differs from an indirect semiconductor (e.g. silicon) in such a way, that the minimum of the highest valence-band has the same value of the wave vector as the maximum of the lowest conduction-band. For visualization see fig. 1.3.

For optical concerns only the region around the Γ-point, the origin of the wave vector, is important. Given a direct semiconductor another approximation is applicable. In adjacencies of the Γ-point the structure of the bands' shape is approximately parabolic. It follows that the energy eingenvalues are:

$$E_{n\mathbf{k}} = E_{n\mathbf{k_0}} + \frac{\hbar^2 \mathbf{k^2}}{2m_n^*} \, , \tag{1.3}$$

with the effective electron mass defined by:

$$\frac{1}{(m_n)^*} = \frac{1}{\hbar^2} \frac{\partial^2 E_{n\mathbf{k}}}{\partial \mathbf{k_i^2}} \, , \tag{1.4}$$

The approximated band structure is shown in fig. 1.2 b). One can notice that the valence-band is degenerated at the Γ-point. The strong bent band is named light hole (lh) band, the one with the smooth band curvature is called heavy hole (hh) band. This nomenclature results from the definition in equation 1.3, 1.4,

because the band curvature equates the effective mass. In addition there exists a split off (so) band.
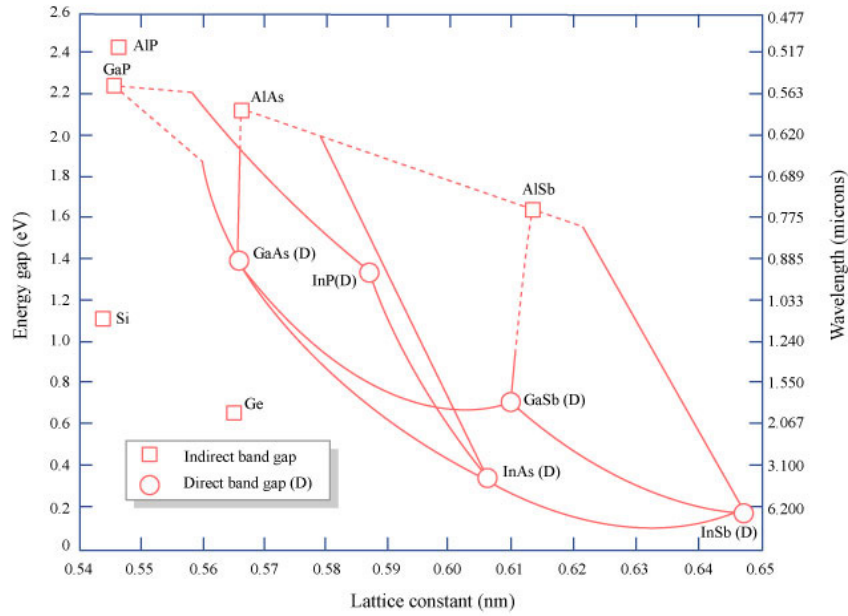
Figure 1.4: Lattice constants and energy gaps of some semiconductors with zinc blende structure at roomtemperature. Courtesy of www.flickr.com/photos/mitopensourceware

In fig. 1.4 the band gaps of some material combinations are shown in dependence of their lattice constant. The two materials most important for this work have, corresponding to their lattice constant, band gaps of $E_{g(InAs)} \approx 0.36$ eV and $E_{g(GaAs)} \approx 1.42$ eV at roomtemperature.

1.1.3   Excitons
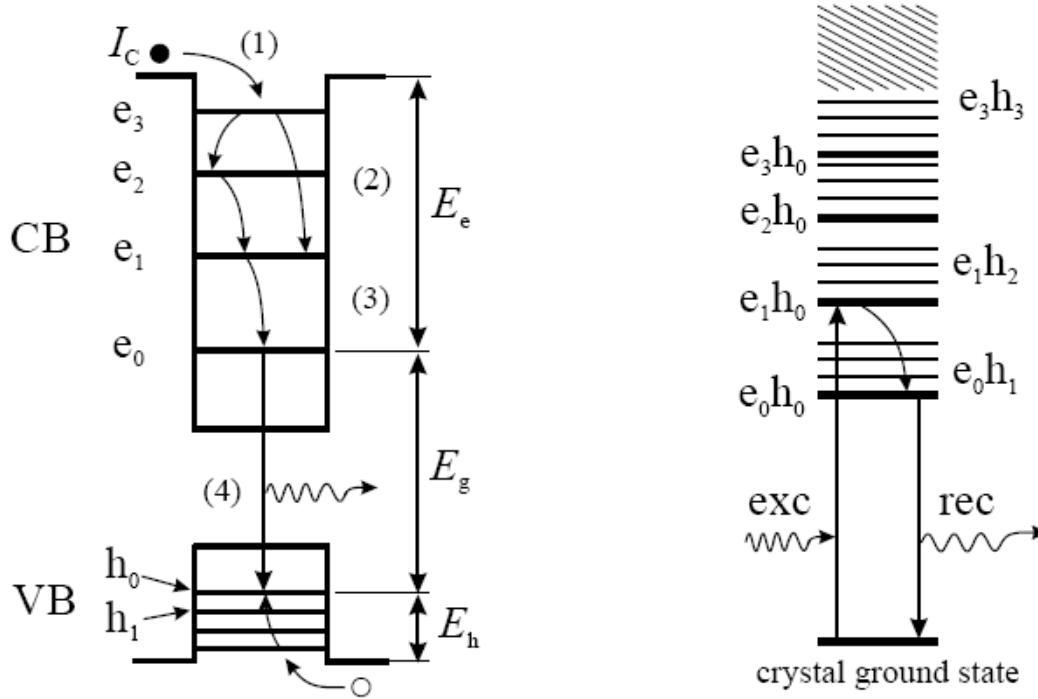
Figure 1.5: Schematics of the two-particle-picture (electron and hole) on the left and of the one-particle picture (exciton) on the right. [10]

For having a semiconductor emitting light one has to shift electrons from the valence- to the conduction-band so that their subsequent recombination creates a photon. There are two possible ways of describing the new situation. First there is the two particle picture where the electron now situated in the conduction-band is the one particle and the hole which it leaves in the valence band is considered as a second particle. The charge of the hole is the negative equivalent of the electron charge. This charge is essential to the implementation of the one particle picture, which is the second possibility to describe the excitation. Because of the charges and the Coulomb exchange interaction there is an attractive connection between the electron and the hole. For the purpose of simplification the electron-hole pair is considered as a quasiparticle which is named exciton. In fig. 1.5 the potentials for both pictures are shown schematically.

To assure the validity of the approximation made in this work with the introduction of the effective mass it has to be clarified that the excitons are considered to be Wannier-excitons. That is, the electron-hole pair, which represents the exciton, extends through the distance of some lattice constants. This definition is contrary to the so called Frenkel-excitons, where electron and hole a located within one lattice constant.

1.2 Quantum dots

If one is working with semiconductors it is important to clarify in which dimension they are existent.
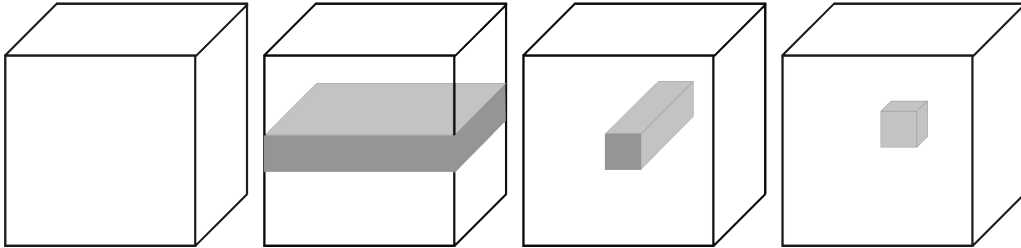
Figure 1.6: Different semiconductor nanostructures: bulk-material, quantum-well, quantum-wire and quantum-dot.

Semiconductors with quantum confinement in zero to three dimensions are shown in fig. 1.6. The simplest form of a semiconductor is the bulk-semiconductor which is limited in no spatial direction and is therefore three-dimensional. If the extend is prevented in one dimension one gets a flat semiconductor-film, namely a quantum well. Decreasing the structure to one dimension one gets a semiconductor-line, a quantum-wire. The smallest existing nanostructure is the one used in this work, the zero-dimensional quantum dot whose extend is limited in all three dimensions.
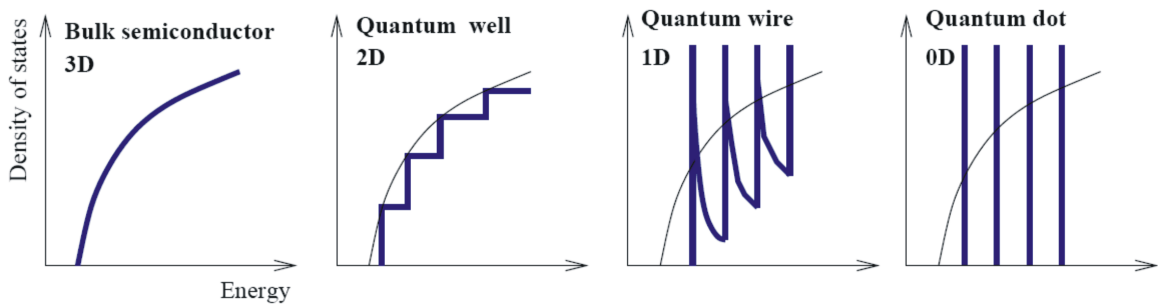
Figure 1.7: Density of states for three-, two-, one- and zero-dimensional systems.

The different nano-structures can be described through a so called confinement potential. Because of the restriction of the dimensions of extension there are energy edges between the single materials that build the potential. Thereby the movement of the carriers is restricted. This potential has influence on the density of states. In fig. 1.7 the relation between the energy and the density of states is shown. The density of states of an unrestricted bulk-semiconductor (3-dimensional) goes with $\sqrt{E}$. A step-like density of states is given for a restriction in one dimension (quantum well). The density of states of the here relevant quantum dots has discrete energy-levels. Because of this characteristic, quantum dots are often referred to as artificial atoms.

1.2.1   Creation of quantum dots
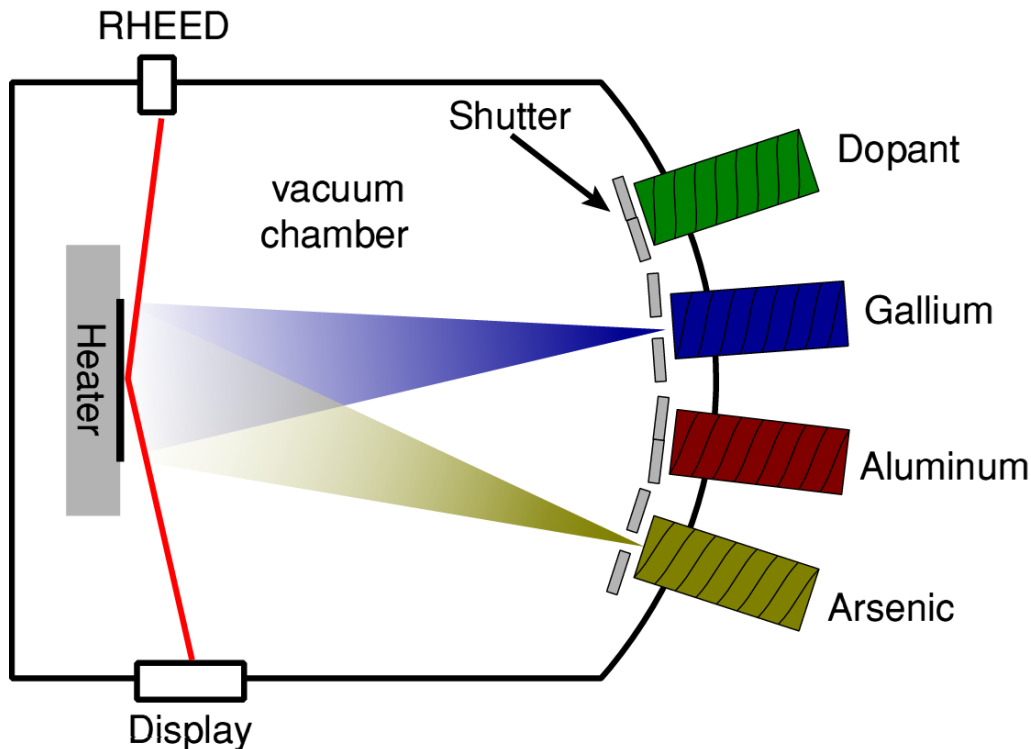
Figure 1.8: Schematic presentation of a MBE-chamber which can be used to produce self-assembled quantum dots. Courtesy of M. Gerbracht

There are three major methods known to build up quantum dots: 1. Etching, where the dots are literally cut out of quantum wells. 2. Colloidal quantum dots, that are created in liquids by chemical processes. 3. Self-assembling, were the dots grow by themselves because of a sufficient mixture of different materials having suitable properties. The latter is how the quantum dots used in this work are created. More concrete the dots where made by using molecular beam epitaxy (MBE) [11], that is explained in the following. A schematic drawing of a MBE-chamber is shown in fig. 1.8. At first the material for application is evaporated in the effusion-chambers, which is in our case indium, arsenic and gallium. At second the molecular-beam is aligned to the substrate (GaAs). The atoms of the molecular beam settle on its surface. With the temperature of the substrate and the timing of applying material one can finally control the growth. Usually some layers of the substrate material are grown in advance of the nanostructures to overcome substrate irregularities.

There are two kinds of phenomena corresponding to the self-organized growth of layers, layer- and island-growth. Which one appears depends on the lattice constant of the different materials that have been introduced in section 1.1. If the lattice constant of the substrate and the applied material are similar smooth layers are formed. Is there on the other hand a significant difference between the lattice constants strain is created which can prevent the growth of closed layers
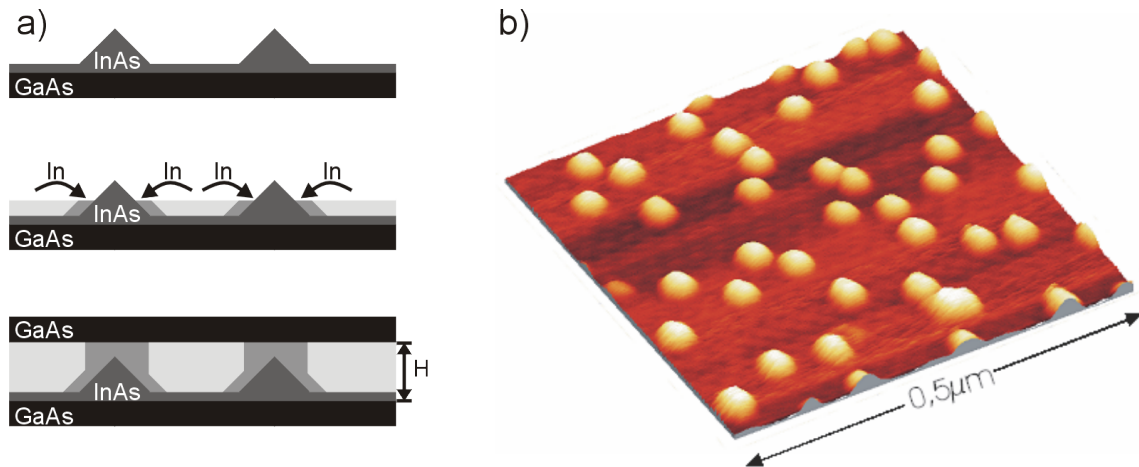
Figure 1.9: a) Scheme of the growth of quantum dots. Top) Wetting layer with quantum dots. Middle) Application of a well meant to shift the emission wavelength. Bottom) Application of a spacer. b) AFM-picture of an ensemble of self-assembled quantum dots. Courtesy of A. Wieck, Ruhr-Uni Bochum

and lead to the appearance of islands. In most cases, which is true also for the current, first a closed coating of few mono-layers is formed which is called wetting layer. Only when the strain is big enough islands grow on top of it, see fig. 1.9 a) top). In fig. 1.9 b) an AFM-picture of an ensemble of such self-assembled quantum dots can be seen. Furthermore, chosen the right environmental conditions, i. e. giving the material not enough time to react to the stress, it is possible also to grow highly stressed quantum-wells.

After creation of the quantum dots either a spacing layer is applied to the sample that acts as a barrier (mostly the substrate material is used) or, like in our case, a well is grown on top of the dots shifting the emission wavelength to more desired ones followed by the spacer (as can be seen in fig. 1.9 a)). Such a nanostructure is called quantum dots in a well (DWELL). After that another layer of dots can be applied following the same methods. In our case 15 layers of quantum dots in a well where grown, the nominal density of the dots is n_{QD} $2x10^{10}$cm^{-2} and the thickness of the spacer layer is 33-35 nm.

1.3   Quantum dot amplifiers
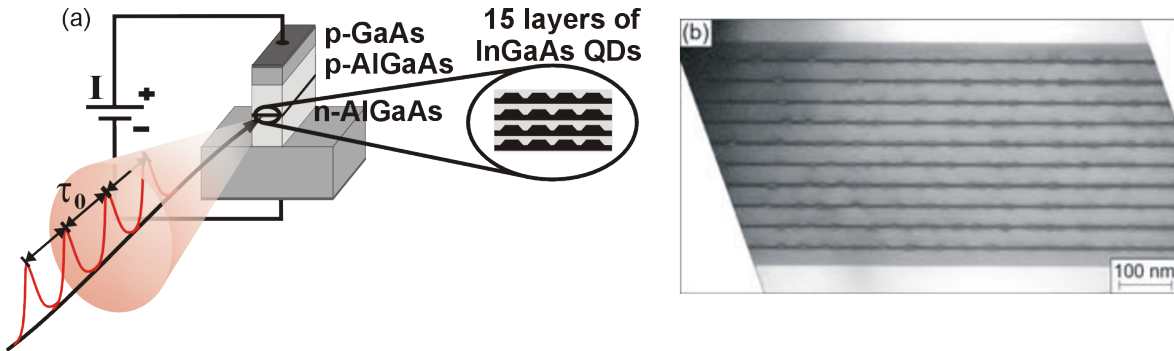
Figure 1.10: Sketch of a quantum-dot amplifier with fifteen layers of quantum dots. The quantum-dot-layers are surrounded by GaAs-layers which are embedded in AlGaAs. The facet of the waveguide are antireflex-coated to avoid multiple-reflection.

The formerly explained quantum dots were integrated into a device for studies. This device (fig. 1.10) is a semiconductor optical amplifier. The quantum dot layers form a waveguide situated in the intrinsic region of a positive-intrinsic-negative diode-structure. Whose cladding layers are made from AlGaAs. Furthermore the device consists of a deeply edged ridge structure to provide optical confinement and waveguiding. Two metal contacts are attached in a way that a current can be applied for injecting carriers, one on top of a p-doped GaAs contact layer, the other one is connected to the GaAs wafer as a bottom contact. Both contacts are top contacts to allow easy access for wiring (see fig. 1.11 for clarification). The length of the device is 1mm; the width of the ridge is 2μm. The endfacets of the waveguide are coated with an anti-reflex coating which avoids multiple-reflections and therefore lasing allowing single pass experiments.
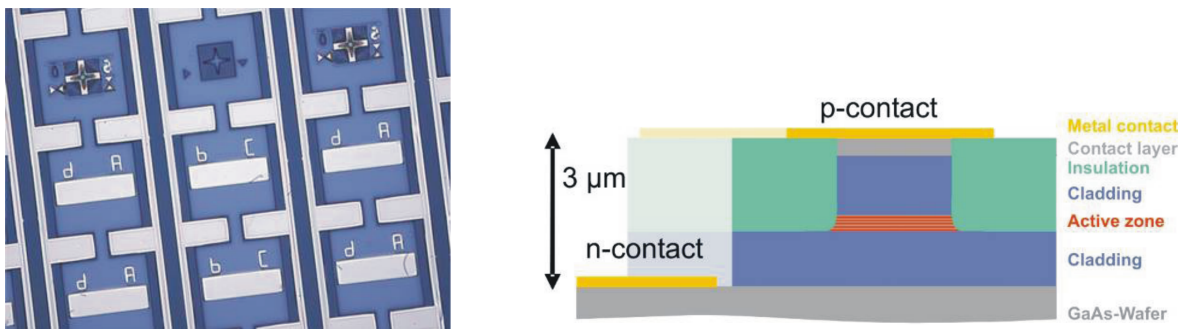
Figure 1.11: Left: Photograph of a topview of the sample. Only one of the visible waveguides is contacted and used. Right: Sketch of a cut trough the device.

In fig. 1.11 a photograph of the sample topview and a schematic of a cut trough the sample are shown. As the picture shows each sample contains more than one waveguide but only one of them is contacted, either A/b (4 μm) or C/d (2 μm). The contact pads directly connected to the waveguide provide the top contact,

the disconnected ones with the letters are the bottom contact. The dark blue material provides isolation.
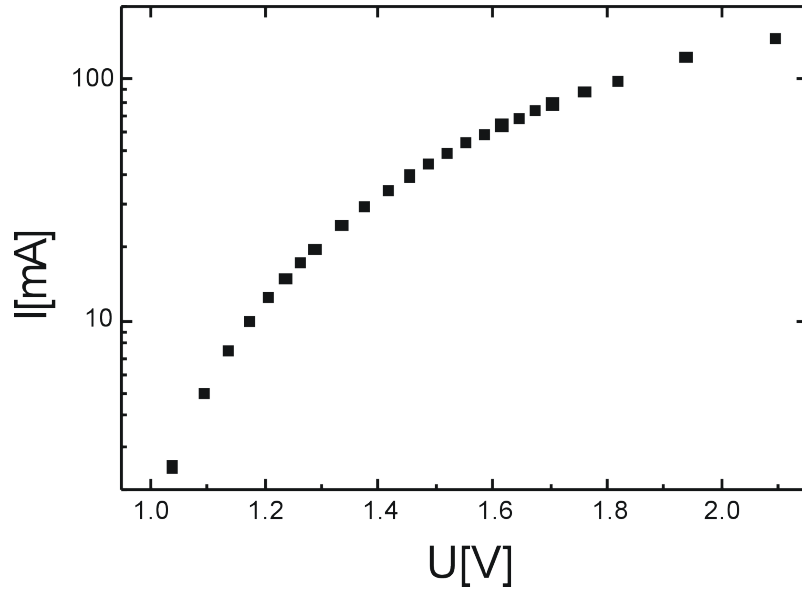
Figure 1.12: Current-voltage graph of the device. The diode structure of the sample is well represented by its characteristics

A proof of the diode-structure of the device is given by taking a look on its characteristics which is shown in fig. 1.12. The diode-like behavior is clearly obvious.

1.4   Experiment and sample characteristics

1.4.1   Experimental setup
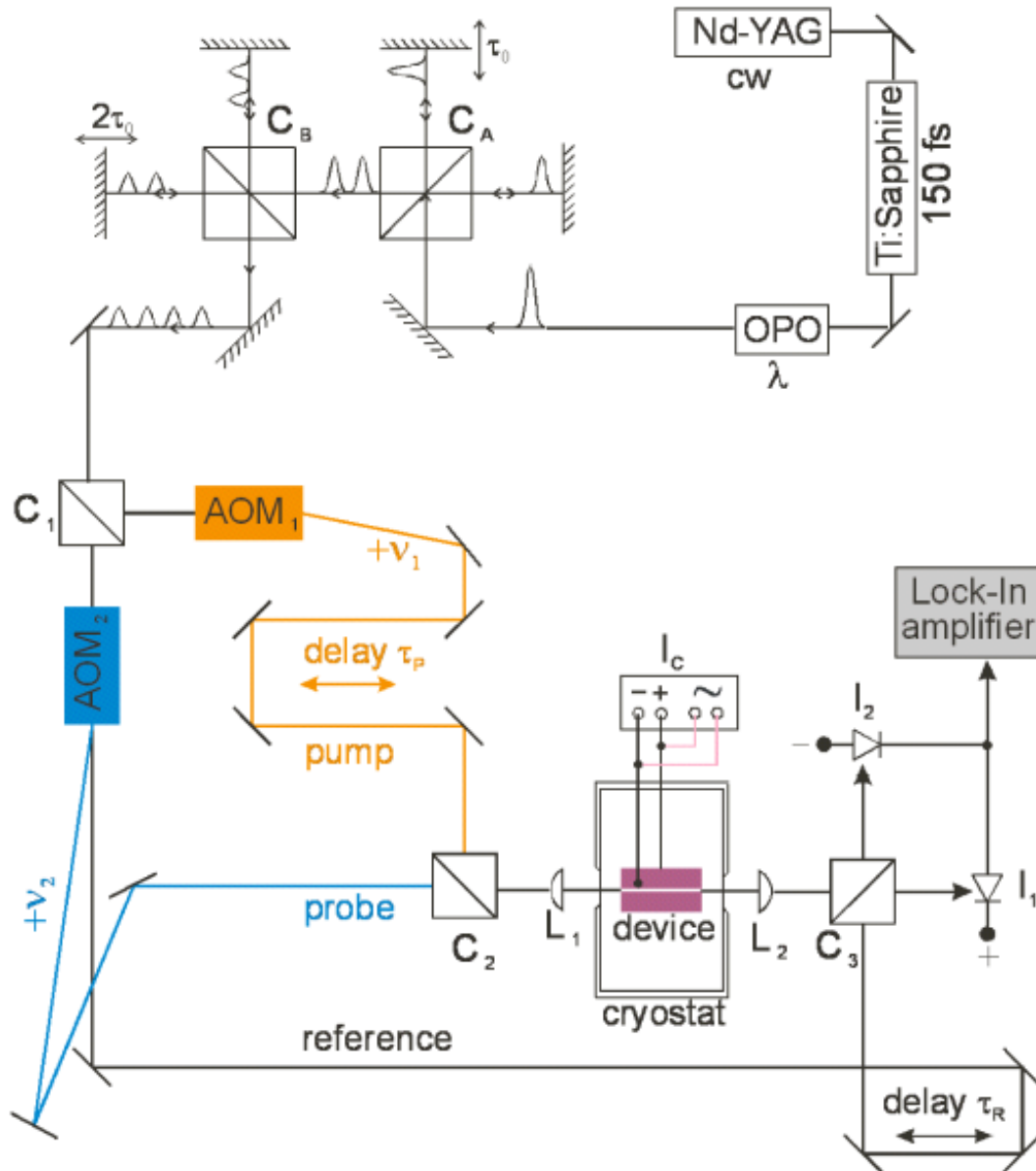
Figure 1.13: Schematic drawing of the experimental setup.

The setup used to analyze the device contains three main parts. The laser-source, a pulse-train generation unit being able to create pulse trains of different repetition rates and a heterodyne pump-probe setup whose specialty is the sensitivity corresponding to amplitude and phase [12, 13]. This provides the opportunity to study several properties of the semiconductor optical amplifiers.

Fig. 1.13 shows the complete setup including the laser-source, the pulse train creation and the heterodyne-setup itself.

Laser source and pulse train generation

We use a diode-pumped Nd:YVO$_4$ laser (cw) as a pump-laser in our laboratory. It pumps a Titan:Sapphire-laser, that provides the necessary 150 fs long laser pulses with a repetition rate of 76 MHz. In order to reach a wavelength in the telecommunication range (around 1.3 μm) we use an optic parametric oscillator (OPO). A two-stage Michelson interferometer is used to create a pulse train (see chapter 2 for details).

Heterodyne-setup

Following the beam path in fig. 1.13 the beam (for better understanding, I keep referring to the pulse-train as a single beam) is split into two parts after entering the setup and each of them passes through an acousto-optic modulator (AOM). This creates a pump- (orange), a probe- (blue) and a reference-beam (black).

Acousto-optic modulator
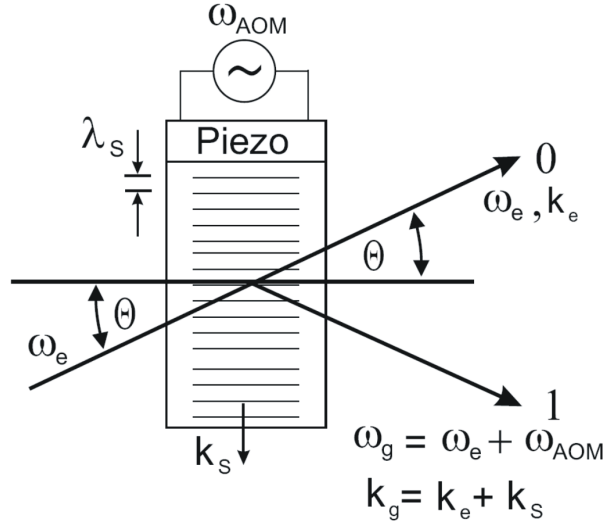
Figure 1.14: Schematic drawing of an acousto-optic-modulator.

The purpose of the acousto-optic modulator is to shift the frequency of each incoming beam. Following the sketch in fig. 1.14 the mode of operation will be explained. In essence an acousto-optic modulator is build of an optically permeable crystal and an attached piezo-crystal, which can be stimulated to oscillate. The oscillations of the piezo create acoustic waves in the crystal, which can be understood as a grating, that diffracts the incoming beams. A beam with the frequency ω_e hits the crystal under the angle Θ that leads to a beam in the

zero order direction with the same frequency and in addition a deflected beam is created in the direction $k_g = k_e + k_s$ with the frequency $\omega_g = \omega_e + \omega_{\mathrm{AOM}}$.

The reference beam and another beam going to an autocorrelator for diagnostic purpose have the same frequency like the beam that enters the setup. The pump-beam is frequency-shifted by AOM2 by $\omega_2 = 79\mathrm{MHz}$ the probe-beam by AOM1 by $\omega_1 = 80\mathrm{MHz}$. Pump and probe beam are reunited and form the collinear beam focused by a lens onto the device. An aperture placed after the device makes sure, that the signal contains only desired modes. For the balance-detection the signal coming from the device and the reference-beam are united and split in two equal parts.

Balanced detection

Considering two beams that interfere in a beam splitter, while one beam (a) is phase shifted against the other beam (b):

$$E_a(t) \sim \exp\{-i\omega_a t\} \tag{1.5}$$

$$E_b(t) \sim \exp\{-i\omega_b t + \phi\} \tag{1.6}$$

The easiest way of describing the process of transmission in the beam-splitter is the matrix-formalism [14, 15]:

$$\begin{pmatrix} E_1(t) \\ E_2(t) \end{pmatrix} = \begin{bmatrix} \sqrt{1-T} & \sqrt{T} \\ \sqrt{T} & -\sqrt{1-T} \end{bmatrix} \begin{pmatrix} E_a(t) \\ E_{b(t)} \end{pmatrix} \tag{1.7}$$

T is the transmission coefficient of the beam-splitter. The beams leaving the beam-splitter (beam 1 and beam 2) are in case of a 50:50 ratio:

$$E_1(t) = \frac{E_a + E_b}{\sqrt{2}}, \ E_2(t) = \frac{E_a - E_b}{\sqrt{2}} \tag{1.8}$$

Calculating now the intensity of these beams $I_i = |E_i|$, one gets:

$$I_1 = (1-T)I_1 + TI_2 + \sqrt{T(1-T)}P \tag{1.9}$$

$$I_1 = (1-T)I_1 + TI_2 - \sqrt{T(1-T)}P \tag{1.10}$$

where both fields are only present in P:

$$P \sim E_a(t)E_b^*(t) \sim \exp\{(\omega_a - \omega_b)t - \phi\} \tag{1.11}$$

With a lock-in amplifier it is possible to detect the amplitude and the phase because of the beating $\omega_a - \omega_b \approx 1\mathrm{MHz}$. If one of the electric fields is constant (reference beam) changes in amplitude and phase of the other one (either pump or probe beam) are detectable. This is the case for our setup.

The two beam-parts of the balanced detection are detected by using two InGaAs-PIN-photo diodes. The detectors are switched contrariwise. That filters constant parts from the signal. Such an arrangement with one beam-splitter and two detectors is named balanced two-channel-detection.

One of the advantages of the setup, if not the advantage at all, is the sensitivity of the setup corresponding to amplitude and phase of the signal.

In addition to the balanced detection there exists the possibility to direct the signal of the device instead of uniting it with the reference-beam on a single germanium-detector or the signal can be directed to a spectrometer.

1.4.2   Measurement methods

Measurement of emission spectra

To get the spectra of the amplified spontaneous emission injection currents of different strengths are applied to the device. For this type of measurement no laser-beam is required. The signal emitted by the device is guided to a spectrometer. A nitrogen-cooled germanium-detector is attached to the spectrometer which collects the signal. A corresponding graph is shown in fig. 1.17

Single pulse transmission

Only one of the signal-beams (pump- or probe-) is used for this kind of measurements. The light which is transmitted through the device is collected by the germanium detector, the balanced-detection is not involved here. The variable parameter is the intensity of the incoming beam that is manipulated with the corresponding acousto-optic modulator. Fig. 1.20 shows a graph measured using this method.

Differential transmission spectroscopy

I start with the explanation of a slightly differently constructed setup, which makes it easier to illustrate the principle of differential transmission spectroscopy. This setup is shown in fig. 1.15.
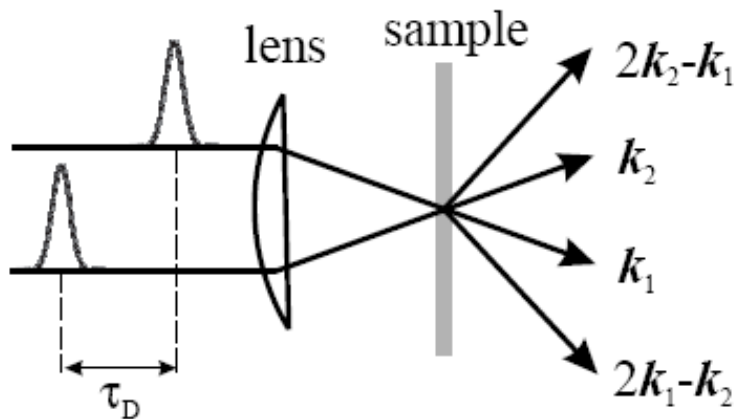
Figure 1.15: Sketch of an experiment of differential transmission spectroscopy with direction selection.

The beam coming from the laser is split into two parts as already explained. One of the split beams hits the sample directly. The other one is delayed by a delay stage about a time span τ. Both of the beams are directed towards the sample and focused onto it by a lens. The beams are hitting the sample under two directions $\mathbf{k_1}$ and $\mathbf{k_2}$. One of the beams (probe) is used to detect the changes of the optical properties of the sample induced by the other beam (pump). Therefore the power of the probe beam is chosen to be weak enough to

not disturb the system by itself. In the geometry shown in fig. 1.15 the beams are distinguished by their direction. In addition to the beams at $\mathbf{k_1}$ and $\mathbf{k_2}$ additional dispersed beams can be detected at $2\mathbf{k_1} - \mathbf{k_2}$ and $2\mathbf{k_2} - \mathbf{k_1}$. They can be used to study the polarization evolution of the sample. In our case the transmitted electric field of the probe-pulse is the thing of interest and is therefore detected. It has the form

$$\mathbf{E}(\mathbf{r}, \omega) = \mathbf{E_0}\exp\{i[n(\omega)\mathbf{kr} - \omega\mathbf{t}]\}\exp\{-\kappa(\omega)\mathbf{kr}\} \qquad (1.12)$$

where $\mathbf{r}$ is the position vector, $\mathbf{E_0}$ the amplitude of the field, ω the frequency, $\mathbf{k}$ the wave vector, c the vacuum speed of light, $n(\omega)$ the refractive index and $\kappa(\omega)$ the extinction coefficient. If eq. 1.12 is considered as a decay of a intensity propagating through a material $I(r) = I(0)\exp\{-\alpha r\}$ the variables used in eq. 1.12 and the absorption coefficient α are linked by the relation $\alpha(\omega) = \frac{2\omega}{c}\kappa(\omega)$. This absorption coefficient is directly connected to the situation inside of the sample, more precisely with the carrier density of the electrons and holes. As will be shown later the pump-pulse creates excited states that affect the probe-pulse. If one compares the transmitted signal with a previous pump-pulse (T) with the transmitted signal without a previous pump-pulse (T_0) one gets information about the absorption coefficient and therefore about κ. More precise is

$$d\Delta\alpha = \frac{T - T_0}{T_0} \qquad (1.13)$$

where d is the length of the sample, in our case 1 mm.
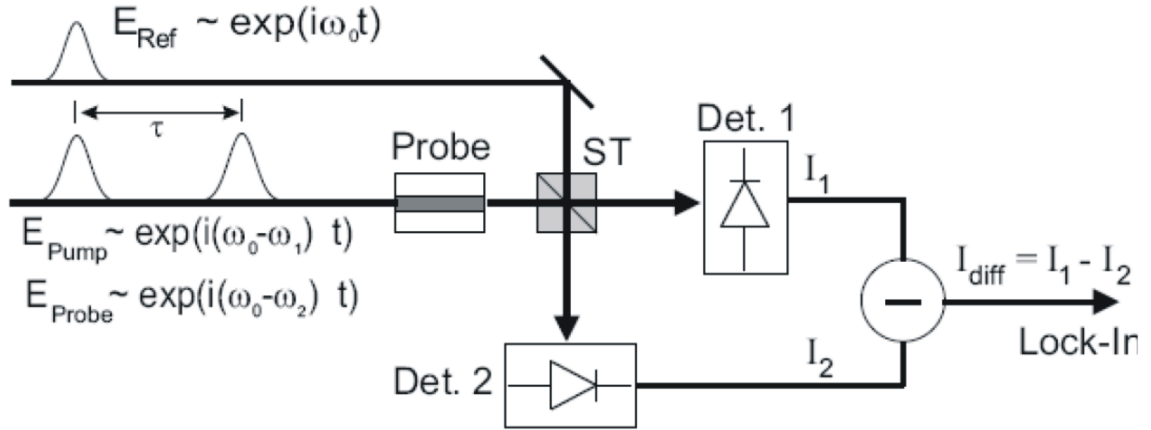
Figure 1.16: Sketch of an experiment with differential transmission-spectroscopy with frequency selection.

Hence our device is a single-mode-waveguide where pump- and probe-beam are traveling through the same mode there is no possibility to use direction selection. To approach this problem the heterodyne setup is used. The clue in this is that the beams are now distinguished by their frequency instead of their direction. In fig. 1.16 the essential parts of the heterodyne-setup are shown once again to make the explanation easier.

As already mentioned pump- and probe-beam experience an acousto-optic modulator controlled frequency-shift (ω_1 and ω_2) corresponding to entrance- and reference-beam. Exactly like for direction selection the probe-beam is delayed compared to the pump-beam. The actual selection takes place after the union of the three beams inside the beam-splitter (C3)and the re-splitting into two signals send to the detectors. The form of the two signals is already known from eqs. 1.9 and 1.10. Their shared mixed term is, (see in addition eq. 1.11)

$$P \sim E_{Probe}(t)R^*_{Ref}(t) \sim \exp\{\mathrm{i}(\omega_2\mathrm{t} - \phi)\}\,. \tag{1.14}$$

To give a complete overview about the possible experiments that can be performed using this setup I have to ad four-wave-mixing which was done some time ago [16]. Since we did not keep on with this I abstain from explaining it.

1.4.3 Sample characteristics

First characteristic features of the device such as its energetic structure and differential gain are shown in this subsection.

Amplified spontaneous emission

Spectra of the room temperature amplified spontaneous emission (ASE) are shown in fig. 1.17 for different injection currents. The emission wavelength for the quantum dot ground state lays at 1,29 μm. The first exited states emits at 1,22 μm. Therefore the energetic gap between the quantum dot ground state and the first excited state is 70 meV. For low injection currents it can be clearly seen, that the quantum dot ground state is the only populated state. We call this case low-density-case because the quantum dots are filled with few excitons only. With increasing current the first excited state is populated too and exceeds the ground state for injection currents higher than 75 mA. This is called the high-density-case in which nearly all quantum dots are filled with some excitons. If it was possible to increase the current further without destroying the device it is likely that the excited state would show the same saturation behavior as the ground state.

In addition to the two cases of high and low density there exists the in-between-case of transparency. In transparency the quantum dots are filled with one exciton in average leading to a balanced situation between absorption and gain. In the spectra of the amplified spontaneous emission one can not notice this case, but it will become important and be shown in a later part of this work.

To identify the energy of the two states the spectra were fitted with a double Gaussian function for each injection current. In addition an estimation of the population of the single states was done by calculating the area below the Gaussian fits. The scale was chosen to have two as maximum of the ground-state population corresponding to the Pauli principle. The four of the excited state maximum turns out naturally, as seen in the inset of fig. 1.17.
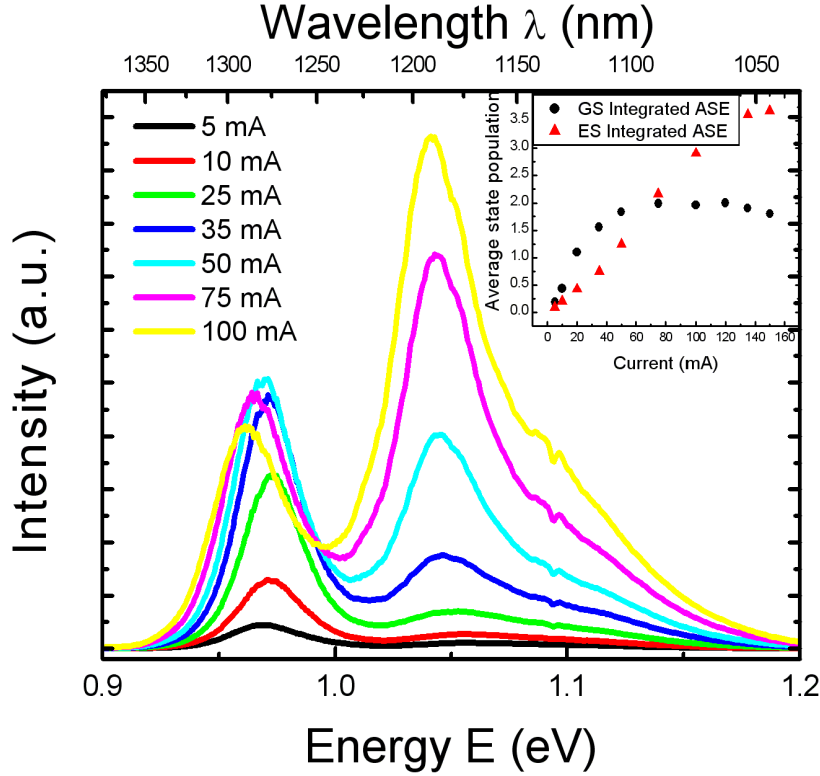
Figure 1.17: Spectra of the amplified spontaneous emission at room temperature for different injection currents and, in the inset, the corresponding populations of the two excitonic quantum dot states.

Temperature determination with interferometry

As mentioned earlier the device was antireflex coated in order to prevent reflections. Since this method is not perfect a small amount of light is still reflected and causes a ripple of the amplified spontaneous emission that becomes visible if one uses a high enough spectral resolution. Some spectra with such a resolution are shown on the left side of fig. 1.18.

If one takes smaller steps in current and observes only a small part of the spectra one can clearly see, that the ripple experiences a phase shift with changing injection current, see fig. 1.18 right.

On the left side of fig. 1.19 this phase shift is plotted in dependence of the injection current. The phase of the device is connected with its refractive index as follows

$$\Delta n = \frac{\lambda}{4\pi \mathrm{L}} \Delta\Phi \,, \tag{1.15}$$

We did measurements of the current-dependent phase shift at different regions of the ASE-spectrum to determine a dependence of the wavelength which we did not find. So we attribute the phase shift to the refractive index only and its dependence of the temperature. To calibrate our thermometric measurement we kept the injection current fixed and changed the temperature externally. That
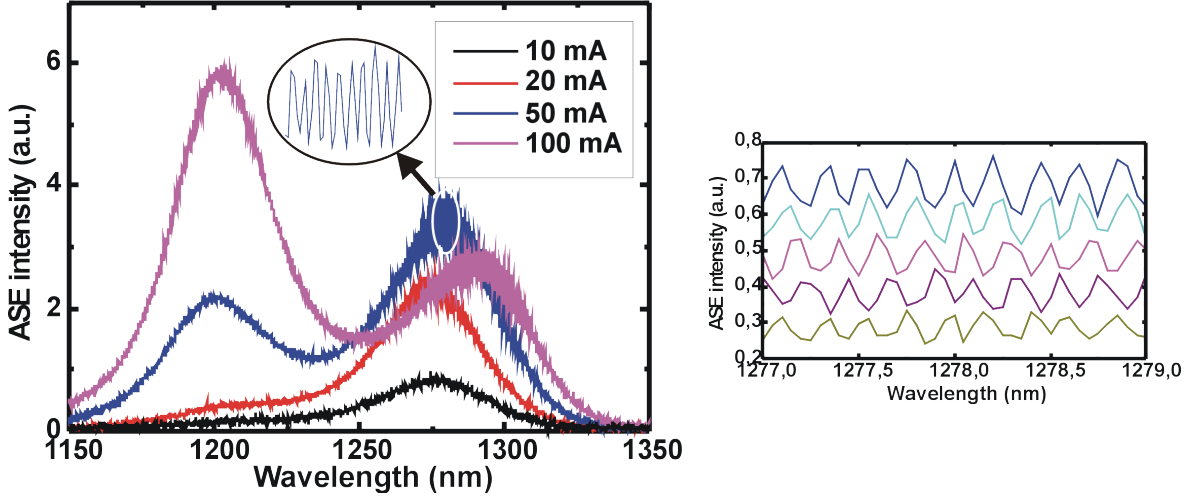
Figure 1.18: Left: High resolution ASE for four different injection currents with obvious gain ripple. Right: Phase shift of the ASE for small injection current steps; curves are displaced for enhanced visibility.
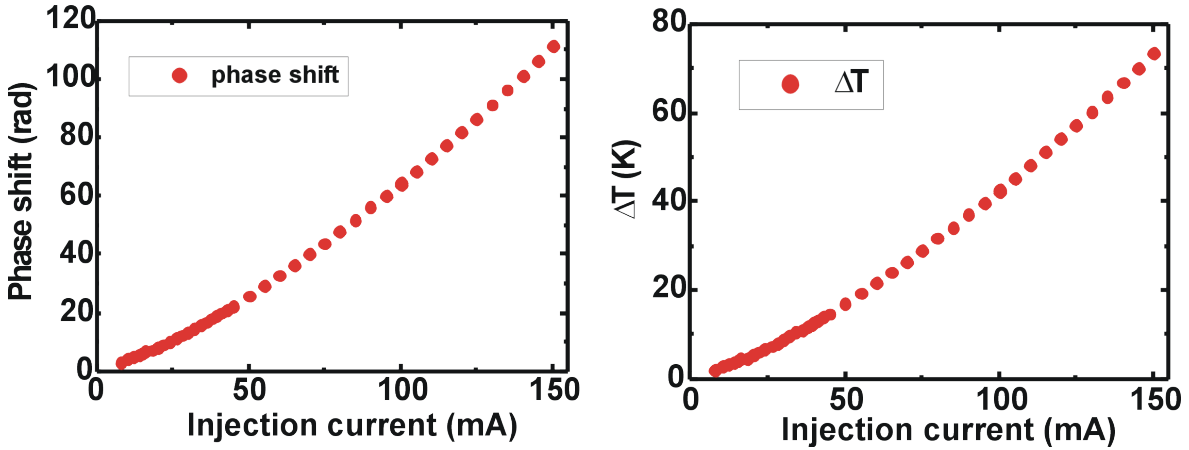
Figure 1.19: Injection current induced phase- (left) and temperature-shift (right).

yields a temperature-dependence of the refractive index of

$$\frac{\partial n}{\partial T} = 1.4 \text{x} 10^{-3} \text{K}^{-1} \,, \tag{1.16}$$

The literature value for pure GaAs at a wavelength of 1μm is $1.5\text{x}10^{-3}\text{K}^{-1}$. The difference results from the waveguide-structure, the impurity of indium and temperature induced changes of the device length. Finally the change of temperature in the device induced by the injection current is shown in fig. 1.19 right), the temperature changes by almost 80 K for a change in injection current from zero to 150 mA.

Differential gain characteristics

In fig. 1.20 the ratio of the incoupled and transmitted energy is shown in dependence of the incoupled energy. This ratio is called gain G. This data was taken for different injection currents. Just as for the spectra of the amplified spontaneous emission one can distinguish between a high- and a low-density case.
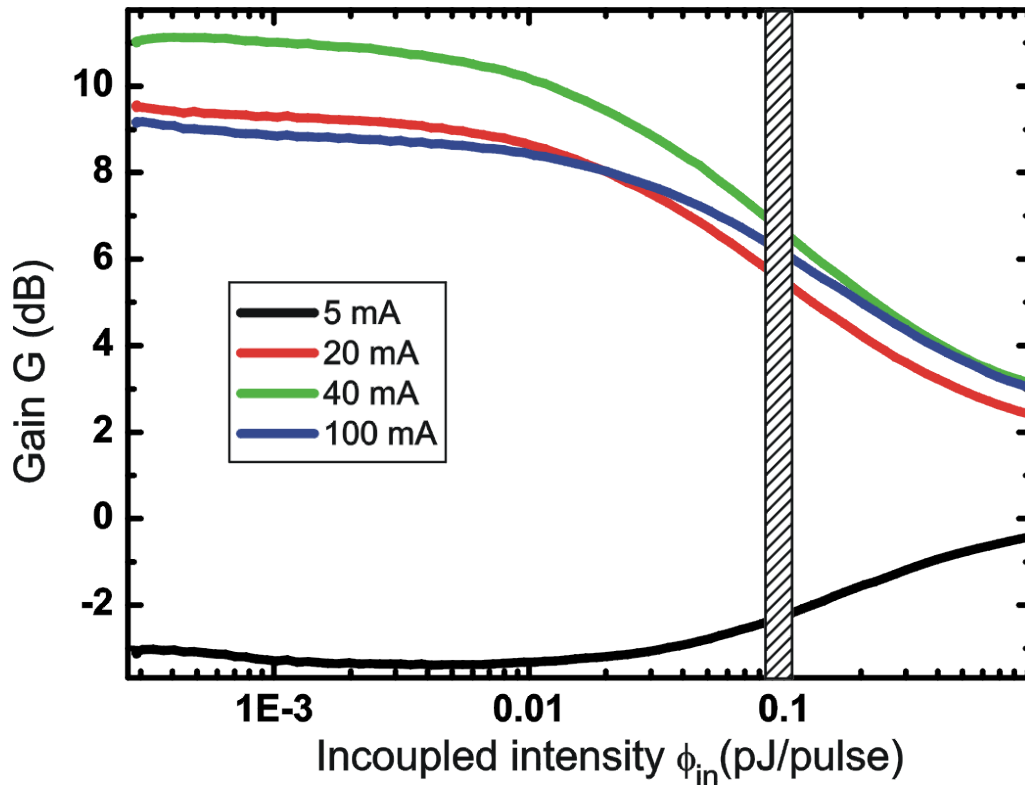
Figure 1.20: Gain in dependence of the incoupled energy for different injection currents.

At first we want to examine the low-density case: Most of the quantum dots are empty, i.e. the incoming laser-pulse is absorbed creating excitons. With increasing intensity of the incoming pulse stimulated transitions become likely. This effect is called bleaching and leads to a saturation of the gain. If the incoming power increase further (above 1 pJ) a process called two-photon absorption where carriers can escape into the surrounding bulk-material by the absorption of two photons, is possible.

The high-density-case differs from the low-density one mostly for low energies. Because of the injected current most of the quantum dots are filled with two excitons. If more energy is coupled in, there will not be anymore excitons created because of their fermionic character. The existing excitons will radiatively recombine instead. This leads to an increase of photons in the pulse which means that it is amplified. With increasing intensity the effects of bleaching and two-photon-absorption take place like in the case of low density. Independent of the injected current the signal will disappear at high input powers.

At a gain factor of 1 the case of transparency is present, i.e. that each quantum

dot in average is filled with one exciton. The incoming beam can on one hand create another exciton and lose therefore energy or on the other hand it can lead an already existing exciton to stimulated recombination and therefore gain energy. Because none of this processes is more likely the energy of the beam stays equal in average. For the device studied in this work the transparency current of the ground state was determined to be at $7.5\,\mathrm{mA}$.

To calibrate the axes some results of the differential transmission, discussed in chapter 3, were used. The transparency current was found there. The axes were chosen in a way that for low incoming energies and at transparency the gain G=1.

The mathematical relation between the gain G and the modal gain factor g_{mod} is the following.

$$\frac{E_{\mathrm{out}}}{E_{\mathrm{in}}} = e^{g_{\mathrm{mod}} L} \,, \tag{1.17}$$

where L is the length of the device.

The modal gain factor is known from the differential transmission spectroscopy measurements. However equation 1.17 is only true inside of the device, for the calibration of the axes reflection losses at lenses and the entrance of the waveguide have to be taken into account.

1.5 Theoretical description of gain dynamics and Coulomb scattering processes

This section describes briefly the formalism of the density matrix theory, a powerful method allowing the microscopic calculation of expectation values of any observable. To facilitate this theoretical basis the following is a short review of the PhD-thesis of Dr. Ermin Malić (chapter 2) whose simulations are discussed in chapter 4.

At first the Hamilton operator of the system is determined. It allows a straight-forward inclusion of many-body interactions, such as electron-electron or electron-phonon coupling, as well as the description of nonlinear effects.[17]. From there the semiconductor Bloch equations are derived. Finally, the absorption coefficient is calculated and used to determine the gain dynamics.

Since the measurement of a complete set of commuting observables necessary for an exact description of a quantum confined solid state structure can not be performed the state vector of that system stays unknown. Instead a statistical mixture of possible states and their probability can be described by the density operator ρ

$$\rho = \sum_i p_i |\Psi_i\rangle\langle\Psi_i| \quad \text{with} \quad \sum_i p_i = 1\,, \tag{1.18}$$

which is a sum of projectors onto the possible state vectors $|\Psi_i\rangle$, each weighted by a classical probability p_i with $0 \leq p_i \leq 1$ [18, 19]. The state vector $|\Psi(t)\rangle$ of a system is given in the Schrödinger picture by $|\Psi(t)\rangle = \sum_i c_i(t)|u_i\rangle$, where the vectors $|u_i\rangle$ form an orthonormal basis of the state space. The evolution of the state vector is described by the Schrödinger equation

$$i\hbar \frac{d}{dt}|\Psi(t)\rangle = H|\Psi(t)\rangle \tag{1.19}$$

with the Hamilton operator H. The expectation value of an observable A is defined as $\langle A\rangle(t) = \langle\Psi(t)|A|\Psi(t)\rangle = \sum_{i,j} c_i^*(t)c_j(t)\langle u_i|A|u_j\rangle$. It is determined by the coefficients $c_i(t)$. Under certain circumstances it can be expressed as the trace over the density operator

$$\langle A\rangle(t) = \text{Tr}[\rho(t)A]\,, \tag{1.20}$$

since $\langle A\rangle(t) = \langle\Psi(t)|A|\Psi(t)\rangle = \sum_{i,j}\langle u_i|\rho(t)|u_j\rangle\langle u_i|A|u_j\rangle = \sum_i\langle u_i|\rho(t)A|u_i\rangle$. (for further details see [20] sec.2.1) The time evolution of the density operator is given by the Von Neumann equation

$$i\hbar \frac{d}{dt}\rho(t) = [H, \rho(t)]\,. \tag{1.21}$$

A system consisting just of one valence- and one conduction-band (see sec. 1.1.2) provides already good information about the optical properties of many struc-

tures. In such a case, the state vector is given by $|\Psi(t)\rangle = c_1(t)|u_1\rangle + c_2(t)|u_2\rangle$ and the density operator can be written as a 2×2 matrix

$$\rho = \begin{pmatrix} c_1^*(t)c_1(t) & c_1^*(t)c_2(t) \\ c_2^*(t)c_1(t) & c_2^*(t)c_2(t) \end{pmatrix} = \begin{pmatrix} \rho_{11}(t) & \rho_{12}(t) \\ \rho_{21}(t) & \rho_{22}(t) \end{pmatrix} . \tag{1.22}$$

The positive real number $\rho_{ii}(t) = |c_i(t)|^2$ expresses the probability for finding the system in the state $|u_i\rangle$. It describes the population dynamics of the states i. The non-diagonal elements $\rho_{12}(t) = \rho_{21}^*(t) = c_1^*(t)c_2(t)$ express the interference effects between the states $|u_1\rangle$ and $|u_2\rangle$ which can only appear when $|\Psi\rangle$ is a coherent linear superposition of these states. They correspond to the probability amplitude for an optical transition, and are often called coherence or microscopic polarization.

The second quantization formalism used in this calculations bases on creation $a_{\boldsymbol{l}}^+$ and annihilation $a_{\boldsymbol{l}}$ operators with the compound index $\boldsymbol{l} = (\lambda, k)$, the band index λ and with the index k representing all quantum numbers of the system. The symmetry conditions are expressed in fundamental commutation relations between these operators

$$[a_{\boldsymbol{l}} , a_{\boldsymbol{l'}}^+]_{\mp} = a_{\boldsymbol{l}} \, a_{\boldsymbol{l'}}^+ \mp a_{\boldsymbol{l'}}^+ \, a_{\boldsymbol{l}} = \delta_{\boldsymbol{l},\boldsymbol{l'}} , \tag{1.23}$$

$$[a_{\boldsymbol{l}} , a_{\boldsymbol{l'}}]_{\mp} = [a_{\boldsymbol{l}}^+, a_{\boldsymbol{l'}}^+]_{\mp} = 0 . \tag{1.24}$$

The fermion's operators anti-commute $([\ ... \ ]_+)$, while the boson's operators commute $([\ ... \ ]_-)$. All many-particle states can now be traced back to a vacuum state $|0\rangle$. For example, an N-particle state can be expressed by creation operators as follows [21]

$$| \phi_{\boldsymbol{l}_1} \cdots \phi_{\boldsymbol{l}_N} \rangle^{\pm} = \frac{1}{\sqrt{N!}} a_{\boldsymbol{l}_1}^+ a_{\boldsymbol{l}_2}^+ \cdots a_{\boldsymbol{l}_N}^+ |0\rangle .$$

The notation of the population probability is changed correspondingly to $\rho_k^\lambda(t) = \langle a_{\lambda,k}^+ a_{\lambda,k}\rangle$ and the microscopic polarization is simplified to $p_k(t) = \langle a_{\lambda,k}^+ a_{\lambda',k}\rangle$. These parameters allow the calculation of expectation values of any observable, e.g. the macroscopic polarization $P(t)$ or the macroscopic current density $j(t)$. These observables are necessary to determine the absorption coefficient $\alpha(\omega)$ fundamental for the description of non-linear pump-probe experiments. To complete the formalism the observables expressed by operators need to be transformed into the second quantization notation, too. All physically relevant N-particle observables A_N can be described by a sum of one-particle A_1^i and two-particle operators $A_2^{(i,j)}$ yielding[21]

$$\begin{aligned} A_N & = \sum_{i=1}^{N} A_1^i + \frac{1}{2} \sum_{i,j}^{i \neq j} A_2^{(i,j)} = \sum_{\boldsymbol{l},\boldsymbol{l'}} \langle \phi_{\boldsymbol{l}}|A_1|\phi_{\boldsymbol{l'}}\rangle \, a_{\boldsymbol{l}}^+ \, a_{\boldsymbol{l'}} \\ & \quad + \frac{1}{2} \sum_{\boldsymbol{l}_i,\boldsymbol{l'}_i} \langle \phi_{\boldsymbol{l}_1} \phi_{\boldsymbol{l}_2} |A_2^{(1,2)}|\phi_{\boldsymbol{l'}_1} \phi_{\boldsymbol{l'}_2}\rangle \, a_{\boldsymbol{l}_1}^+ \, a_{\boldsymbol{l}_2}^+ \, a_{\boldsymbol{l'}_2} \, a_{\boldsymbol{l'}_1} . \end{aligned}$$

The starting point for deriving the temporal evolution of the microscopic polarization $p_{\boldsymbol{k}}(t)$ and the population probabilities in the conduction $\rho_{\boldsymbol{k}}^c(t)$ and the valence band $\rho_{\boldsymbol{k}}^v(t)$ is the Hamilton operator for a many-particle system within the formalism of the second quantization

$$
\begin{aligned}
H &= H_{0,\text{c}} + H_{\text{c-f}} + H_{\text{c-c}} \\
&= \sum_{\boldsymbol{l}} \varepsilon_{\boldsymbol{l}} a_{\boldsymbol{l}}^+ a_{\boldsymbol{l}} + \sum_{\boldsymbol{l},\boldsymbol{l'}} \boldsymbol{d}_{\boldsymbol{l},\boldsymbol{l'}} \cdot \boldsymbol{E}(\boldsymbol{t}) a_{\boldsymbol{l}}^+ a_{\boldsymbol{l'}} + \frac{1}{2} \sum_{\boldsymbol{l_1},\boldsymbol{l_2},\boldsymbol{l_3},\boldsymbol{l_4}} V_{\boldsymbol{l_3},\boldsymbol{l_4}}^{\boldsymbol{l_1},\boldsymbol{l_2}} a_{\boldsymbol{l_1}}^+ a_{\boldsymbol{l_2}}^+ a_{\boldsymbol{l_4}} a_{\boldsymbol{l_3}} .
\end{aligned}
\tag{1.25}
$$

The first two terms $H_{0\text{-c}}$ and $H_{\text{c-f}}$ describe the non-interacting carrier system in the presence of the external electromagnetic field. $H_{0\text{-c}}$ is the part of unperturbed free carriers and $H_{\text{c-f}}$ is the carrier-field interaction part. The last term of the Hamiltonian $H_{\text{c-c}}$ is given by the carrier-carrier interaction. (For a detailed discussion of the single contributions of the Hamiltonian see [20] section 2.2). The time evolution of an observable $\hat{O}$ can be obtained from the Heisenberg equation of motion

$$
i\hbar \frac{d}{dt} \hat{O}(t) = [\hat{O}(t), H]_- + \frac{\partial}{\partial t} \hat{O}(t) .
\tag{1.26}
$$

If $\hat{O}(t)$ has no explicit time dependence, the second contribution vanishes. In the Heisenberg picture the observables are considered to contain the entire time dependence. The equation of motion for the corresponding expectation value is called the Ehrenfest-theorem

$$
i\hbar \frac{d}{dt} \langle \hat{O}(t) \rangle = \langle [\hat{O}(t), H]_- \rangle .
\tag{1.27}
$$

Applying the Hamilton operator from (1.25), utilizing (1.27), and the commutation relations from eqs. (1.23)-(1.24), the equations of motion for the microscopic polarization $p_{\boldsymbol{k}}(t)$ and the population probabilities $\rho_{\boldsymbol{k}}^j(t)$ ($j = c, v$) can be derived

$$
\dot{p}_{\boldsymbol{k}}(t) = -i\omega_{\boldsymbol{k}} p_{\boldsymbol{k}}(t) - i\Omega(t)[\rho_{\boldsymbol{k}}^c(t) - \rho_{\boldsymbol{k}}^v(t)]
\tag{1.28}
$$

$$
- \frac{i}{\hbar} \sum_{\boldsymbol{k'}} [V_{ren}(\boldsymbol{k},\boldsymbol{k'}) p_{\boldsymbol{k}}(t) + V_{exc}(\boldsymbol{k},\boldsymbol{k'}) p_{\boldsymbol{k'}}(t) + V_{dep}(\boldsymbol{k},\boldsymbol{k'}) p_{\boldsymbol{k'}}(t)] - \frac{1}{T_2} p_{\boldsymbol{k}}(t)
$$

$$
\dot{\rho}_{\boldsymbol{k}}^j(t) = 2 Im\,[\Omega^*(t) p_{\boldsymbol{k}}(t)] + \frac{2}{\hbar} Im \left[p_{\boldsymbol{k}}(t) \sum_{\boldsymbol{k'}} V^j(\boldsymbol{k},\boldsymbol{k'}) p_{\boldsymbol{k'}}(t) \right] - \frac{1}{T_{1,j}} \rho_{\boldsymbol{k}}^j(t) + S_j^{in}
\tag{1.29}
$$

These three differential equations are called semiconductor Bloch equations.[22] The color illustrates, which part of Bloch equations origins in which section of the Hamilton operator (see eq. 1.25). The free-particle contributions are colored blue. The first term in (1.28) describes the free dynamics of the carriers. It leads to an

oscillation of the microscopic polarization with the frequency $\omega_{\boldsymbol{k}} = \omega_{c\boldsymbol{k}} - \omega_{v\boldsymbol{k}}$ corresponding to the band gap. The second part describes the carrier-field coupling which depends on the difference in population probabilities for the two involved states. Its strength is given by the Rabi frequency $\Omega(t) = \frac{1}{\hbar}\boldsymbol{d_{vc}} \cdot \boldsymbol{E(t)}$.

The carrier-carrier interactions (colored red) account for the fact that the set of equations obtained from the Heisenberg equation is not closed. The carrier-carrier interactions couple the dynamics of single-particle elements of the density matrix to higher-order correlation terms.In this calculations, the correlation expansion[23] is used to obtain the presented Bloch equations. The idea of this approximation is that higher-order terms involving an increasing number of carriers become less important.[24, 17] The four-operator term is factorized into products of two-operator terms.

This factorization leads to a closed set of equations of motion for the single-particle elements of the density matrix. If the correlation term is neglected, the truncation is called Hartree-Fock factorization or mean-field approximation. Then, the carrier-carrier interaction leads to: i) $V_{ren}(\boldsymbol{k}, \boldsymbol{k'})$ - renormalization of the single-particle energy, ii) $V_{exc}(\boldsymbol{k}, \boldsymbol{k'})$ - formation of excitons and iii) $V_{dep}(\boldsymbol{k}, \boldsymbol{k'})$ - depolarization part describing processes with no momentum transfer.

Since the correlation of carriers plays an important role for our investigations the Bloch equations (eqs. (1.28)-(1.29)) have been derived beyond the Hartree-Fock approximation going up to the second order in the carrier-carrier and carrier-phonon interaction. The evaluation of the correlation terms, i.e. the consideration of two-particle correlations (also known as the second Born approximation), describes the scattering contributions leading to the coherence decay time T_2 and the population scattering time T_1.

To minimize the necessary effort on time and calculation power several approximations were applied that will be discussed briefly in the following.

Within the rotating wave approximation (RWA) a rapidly oscillating part of the considered function is neglected because of resonance effects. The microscopic polarization $p_{\boldsymbol{k}}(t)$ as well as the Rabi frequency $\Omega(t)$ can be expressed as a product of a fast oscillating part and a slowly varying envelope function. If inserted into the Bloch equation (1.28) two exponents become interesting: for interactions near resonance, the exponential function with the relatively small argument $(\omega_l - \omega)$ contributes considerably more than the one with $(\omega_l + \omega)$. The second one oscillates fast and its contribution vanishes when integrated over a time interval which is long compared to the time of a single oscillation,[25, 26]. Therefore the corresponding term is neglected leading to the modified semiconductor Bloch equation

$$\dot{\hat{p}}_{\boldsymbol{k}}(t) = -i(\omega_{\boldsymbol{k}} - \omega)\hat{p}_{\boldsymbol{k}}(t) - i\tilde{\Omega}(t)[\rho_{\boldsymbol{k}}^c(t) - \rho_{\boldsymbol{k}}^v(t)]\,. \qquad (1.30)$$

This simplified equation is numerically less demanding.

The Markov approximation helps with solving the hierarchy problem mentioned earlier in this section. Key to this approximation is that the memory effects introduced by quantum mechanical smearing of the wave functions are neglected. This approximation is applicable for many-particle systems and systems

with short scattering time scales.

Applying the Markov approximation, yields the Boltzmann equation for the occupation probability of an arbitrary state. (see 4.4)

The random phase approximation uses the assumption that all non-diagonal elements $\langle a_{v,\boldsymbol{k}}^+ a_{c,\boldsymbol{k}'} \rangle$ and $\langle a_{c,\boldsymbol{k}}^+ a_{v,\boldsymbol{k}'} \rangle$ are not necessary to describe the investigated system. This is due to the assumption that the phase factors of these quantities are not correlated and therefore cancel each other out in a summation. This approximation leaves the microscopic polarization $p_{\boldsymbol{k}}(t) = \langle a_{v,\boldsymbol{k}}^+ a_{c,\boldsymbol{k}} \rangle$ and the occupation probabilities $\rho_{\boldsymbol{k}}^i(t) = \langle a_{i,\boldsymbol{k}}^+ a_{i,\boldsymbol{k}} \rangle$ with $i = c, v$ as the dominant $\boldsymbol{k}$ diagonal quantities for the description of the investigated system.

As will be seen later (see chapter 4) for having the possibility to compare theoretical modeled data with experimentally achieved data the absorption coefficient and the optical susceptibility are of interest. They can be achieved using the complex description of the wave vector

$$k(\omega) = k' + ik'' = \frac{\omega^2}{c^2}(\varepsilon' + i\varepsilon'') \qquad (1.31)$$

The Beer-Lambert law for the intensity $I(z, \omega)$ of an electromagnetic wave is

$$I(z, \omega) = |E(z)|^2 = e^{-2k''(\omega)z} = e^{-\alpha(\omega)z} \qquad (1.32)$$

with the absorption coefficient $\alpha(\omega) = 2k''(\omega)$. It determines the traveling distance of the light through a material.

The real part of the wave vector gives the refractive index $n(\omega)$ with $n(\omega) = \frac{c}{\omega} k'(\omega)$. It determines the change of the speed of light in a medium $c_m(\omega) = \frac{c}{n(\omega)}$. For most structures the real part of the dielectric function $\varepsilon(\omega)$ is larger than the imaginary part resulting in the widely used approximation $n(\omega) \approx \sqrt{\varepsilon(\omega)}$. Often, the refractive index has only a weak dependence on frequency. Therefore, the absorption coefficient can be simplified to

$$\alpha(\omega) \propto \omega Im\, \varepsilon(\omega) = \omega Im\, \chi(\omega) \qquad (1.33)$$

with the dielectric function $\varepsilon(\omega) = \chi(\omega) + 1$.

The optical susceptibility $\chi(\omega)$ can be calculated with the Fourier transform of the macroscopic polarization $P(\omega)$ and can be written as[27]

$$\chi(\omega) = \frac{P(\omega)}{\varepsilon_0 E(\omega)}\,. \qquad (1.34)$$

The classical macroscopic polarization $P(\boldsymbol{r}, t) = e \sum_i \boldsymbol{r} \delta(\boldsymbol{r} - \boldsymbol{r}')$ is defined as dipole density. In second quantization it can be written as a sum over the microscopic polarization $p_{\boldsymbol{k}}(t) = \langle a_{v\boldsymbol{k}}^+ a_{c\boldsymbol{k}} \rangle$ and the dipole matrix element $\boldsymbol{d}_{vc}(\boldsymbol{k})$

$$P(t) = \sum_{\boldsymbol{k}} d_{vc}(\boldsymbol{k}) p_{\boldsymbol{k}}(t) + \text{c.c.}\,. \qquad (1.35)$$

The dynamics of the microscopic polarization can be calculated with the Bloch equations [eqs. (1.28)-(1.29)]. The optical matrix element $d_{vc}(\boldsymbol{k})$ is often adjusted to experimental data.

Chapter 2

Concepts and realization of GHz optical pulse-train generation

An essential and advanced part of the experiments is the generation of the incoming optical pulse train in the range of 10 GHz to 1 THz. In this chapter different ideas how to generate pulse trains will be explained. At first the general idea of pulse-shaping is introduced. It follows a pulse shaper based on a liquid crystal display (LCD) in an improved 4f-geometry, which was used in our first attempt to generate pulse trains. At last the current used solution, a two-stage Michelson interferometer, will be explained. The advantages and disadvantages of the methods are discussed briefly at the end of the chapter.

2.1 Theoretical concepts related with pulse shaping

This section gives the theoretical background necessary for understanding the pulse shaping process. Its major element is the Fourier transformation. In addition the diffraction at a grating is very important for its functionality. Because interference effects played a roll in our ideas during the development they will be explained too.

2.1.1 Fourier transformation

It is well known [28] that a wave can be described as a linear combination of harmonic oscillations

$$f(x,t) = \frac{1}{(2\pi)^2} \int_{-\infty}^{\infty} \int_{-\infty}^{\infty} F(k,\omega) \exp\{-\mathrm{i}(\mathrm{kx} + \omega \mathrm{t})\} \mathrm{dkd}\omega \,, \qquad (2.1)$$

with

$$F(k,\omega) = \int_{-\infty}^{\infty} \int_{-\infty}^{\infty} f(x,t) \exp\{\mathrm{i}(\mathrm{kx} + \omega \mathrm{t})\} \mathrm{dxdt} \qquad (2.2)$$

being their Fourier transformation.

The beam entering the pulse shaper is supposed to be a linear combination of plane waves. At first we define the beam as dependent on space and time

$f(x,t)$. For later discussions keep in mind, that every lens induces a spatial Fourier transformation to the incoming beam.[28]

2.1.2   Diffraction at a grating

Each grating corresponds to a frequency Fourier transformation, diffracting the incoming beam depending on the included frequencies according to the grating equation

$$d(sin\Theta_{\text{out}} - sin\Theta_{\text{in}}) = n\lambda \qquad (2.3)$$

with d being the distance between two lines of the grating, λ the wavelength of the light, Θ_{in} the incoming, Θ_{out} the outgoing angle and n the order of the diffracted beam.

Diffraction can be depicted using the Huygens' principle. A wavefront hits an obstacle, a grating in our case, then each point of the wave is suggested to be the starting point of an elementary wave and the wave after the obstacle is described as the envelope of these elementary waves. The single waves gain a phase difference depending on the length of their specific path each wave travels between obstacle and the observation point. Corresponding to the interference principal explained in the following section there will be differences in the beams for different directions, beams with increased intensity and beams with up to zero intensity. Counting beams of high intensity one defines orders of beams, starting with zero.

2.1.3   Interference

The principle of superposition is valid for light, i.e. the electrical field strength at a given point is a sum of all corresponding field strengths. Two waves

$$\mathbf{E_1(rt)} = \mathbf{E_{01}cos(rk_1 - \omega t + \delta_1)} \qquad (2.4)$$

and

$$\mathbf{E_2(rt)} = \mathbf{E_{02}cos(rk_2 - \omega t + \delta_2)} \qquad (2.5)$$

meet at a certain point, then the intensity of the field in that point is given by

$$I \sim |\mathbf{E}|^2 = \frac{1}{2}\left[\mathbf{E_{01}^2 + E_{02}^2 E_{01}E_{02}cos(rk_1 + \delta_1 - rk_2 - \delta_2)}\right] \qquad (2.6)$$

with the argument of the cosine being the difference in phase between the beam parts. Summarizing slightly, $E_{01}^2/2 = I_1$ and correspondingly E_{02} as well as $\delta = \mathbf{rk_1 - rk_2} + \delta_1 - \delta\mathbf{2}$, one obtains

$$I \sim I_1 + I_2 + 2\sqrt{I_1 I_2}cos\delta \,. \qquad (2.7)$$

The last term in eq. 2.7 is called interference term and it is obvious that the overall intensity can reach all values between 0 and $I_1 + I_2$ in dependence of the phase difference of the beam parts due to this term. Destructive interference, meaning complete cancellation takes place at a phase difference of $\delta = \pm\pi, \pm3\pi, \pm5\pi, ...,$ constructive interference, i.e. $I = I_1 + I_2 + 2\sqrt{I_1 I_2}$, instead at a phase difference of $\delta = 0, \pm2\pi, \pm4\pi, ...$

2.2 Pulse shaper development

Starting from the simple pulse shaper introduced to the beam path directly after the OPO to compensate a possible chirp, over the classical 4f-geometry used for most pulse shapers and a modified version with a phase mask the development of the final solution to generate pulse trains with a two-stage Michelson interferometer will be explained.

2.2.1 Pulse shaper for chirp compensation

Directly after the laser pulse leaves the OPO it is aligned through a simple pulse shaper to compensate a possible chirp.
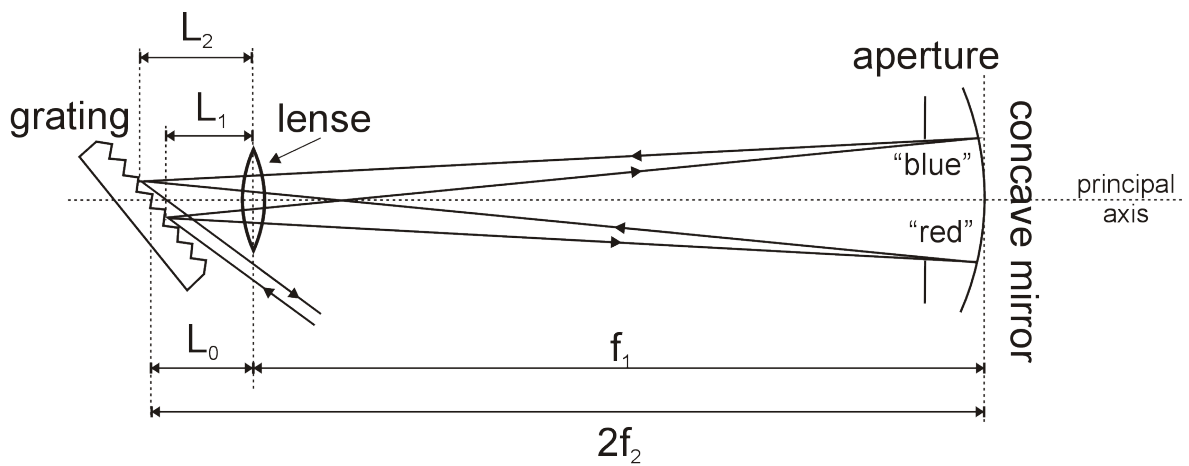

Figure 2.1: Schematic drawing of a simple pulse shaper.

A schematic of that pulse shaper is shown in fig. 2.1. It consists of one grating to separate the different parts of the spectrum, a lens for focusing the beam and a concave mirror.

The beam hits the grating slightly below the principal axis and is split in its spectral constituents as explained in the previous section. Using a lens the spectral parts are focused on a concave mirror and reflected back through the lens that transforms the beam back to being parallel. Next the beam hits the grating again this time slightly above the principal axis. There the spectral constituents are merged respectively the beam is transformed back.

The important parameter in the concern of compensating a chirp is the distance L_0 between the center of the grating and the lens. To have the image point in the center of the grating L_0 has to match the following condition.

$$L_0 = f_1 - \frac{f_1^2}{2f_2} \tag{2.8}$$

Fig. 2.2 shows an exaggerated version of a setup where is $L < L_0$. By shifting the grating relative to the lens the image point walks out of the center of the mirror. In the given example it moves to the left. For better visualization a longwave
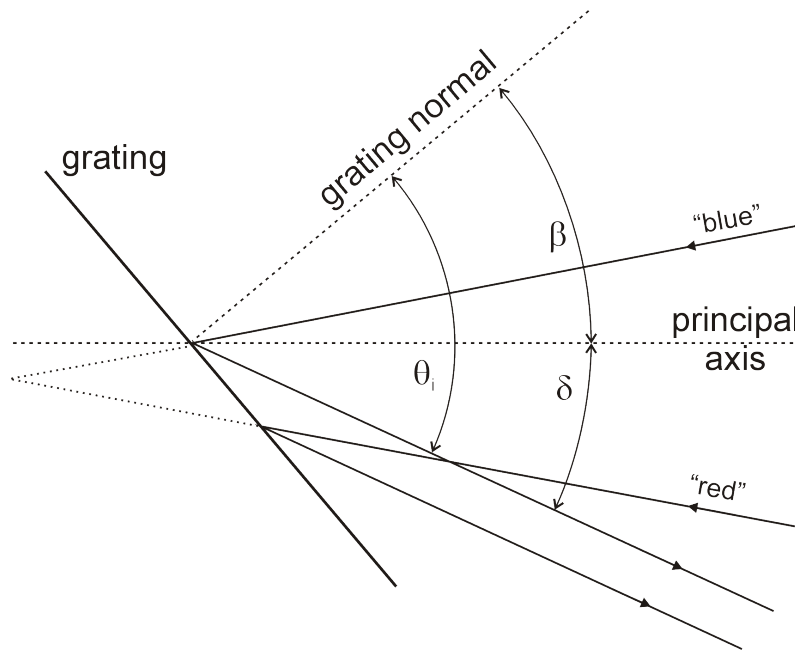
Figure 2.2: Schematic of the compensation of a negative chirp.

(red) and a shortwave (blue) part of the beam is plotted. It is obvious that the shortwave bundle has to travel a longer way than the longwave one, which would lead to a compensation of a possible negative chirp.

Using an adequate aperture in front of the concave mirror one can already shape the spectrum of the beam with such a pulse shaper by cutting its edges. Indeed this method is far away from being precise and does not allow for a controlled shaping. Therefore this method of pulse shaping is of no further interest here.

But basically all parts necessary in more advanced pulse shapers are already present in this simple one. One of the parts not yet explained is the liquid crystal display. This device, also referred to as mask, is available in two versions either as a phase- or as an amplitude-mask. The display we used is a phase mask. Its structure is shown in fig. 2.4.

2.2.2   Phase mask

The active region contains the liquid crystal. The orientation of the molecules of the liquid crystal can be modified by applying an electric field (see fig. 2.3). These manipulations control the effect the display has to an electro-magnetic wave traveling through it. Applying a field to the liquid crystal induces dipoles in the molecules. Their force moves the molecules from their stationary position and aligns them with the applied field. The refractive index of the liquid crystal depends on the orientation of its molecules. Therefore the optical path lengths of two beams hitting two differently aligned areas of the mask are different which leads to a phase shift between them. Thereby their delay depends linearly on the
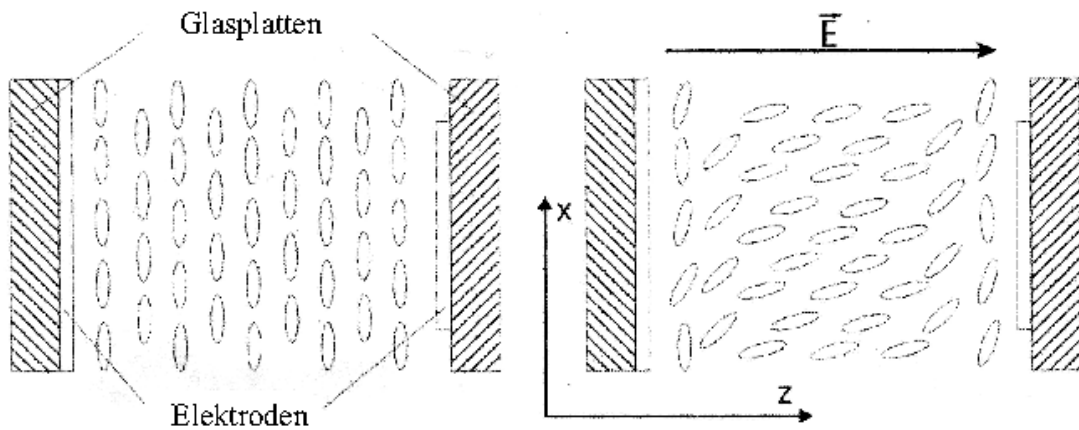
Figure 2.3: Sketch of a liquid crystal display. With the influence of applied voltage.

difference of the refractive indices.
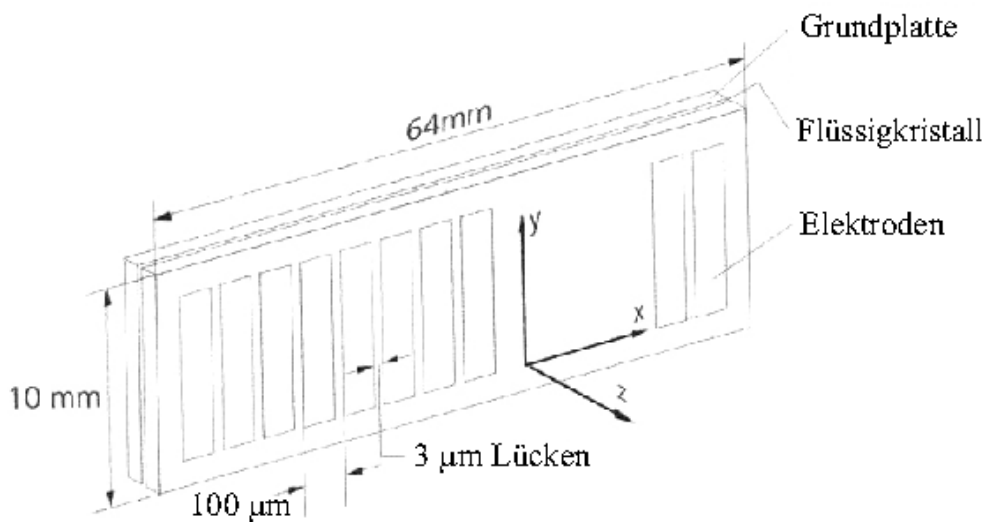
Figure 2.4: Sketch of a phase mask. [29]

The liquid crystal of our display is 9 μm thick. The length of the display is 64 mm, its hight 10 mm. The liquid crystal is placed between two glass plates on whose inner surface 640 transparent electrodes are attached. Each electrode has a width of 97 μm and there is a gap between them of 3 μm. I.e. we have 640 separately addressable pixels. The measures of the display are also shown in fig. 2.4.

Figure 2.5: Sketch of a pulse shaper with phase mask and lenses.

2.2.3   4f-setup

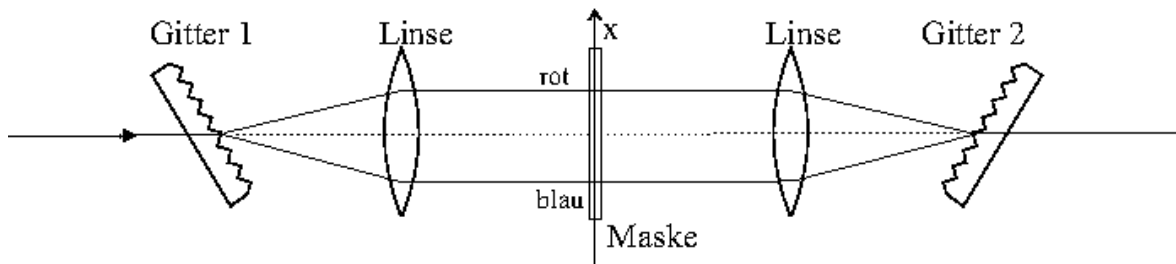The structure of the setup schematically shown in fig. 2.5 is known as 4f-geometry and is sufficient for describing the operating mode of our LCD shaper even if we modified it. The beam coming from the laser hits the grating and splits up spectrally. Then it is imaged on the mask similar to how it happens in the simple pulse shaper. After the separated spectral parts of the beam were manipulated by the mask, they are merged again by the mirror-symmetric setup. In case the mask is an amplitude mask the transparency of single pixels can be controlled and the intensity of the individual frequencies can be reduced. Is it instead a phase mask only the phases of the different frequencies can be shifted against each other.
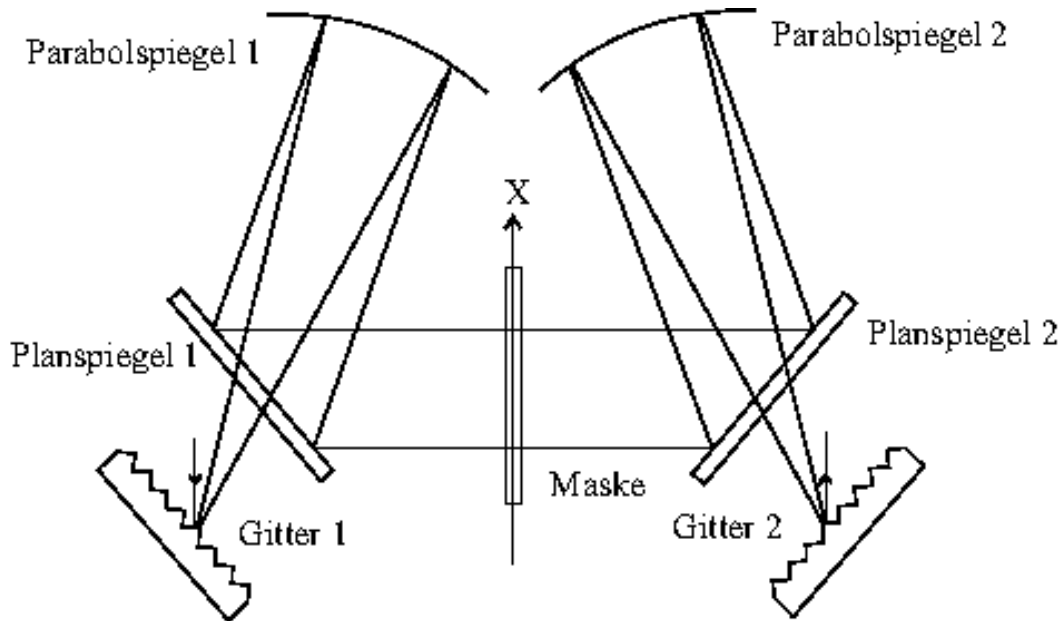

Figure 2.6: Sketch of a pulse shaper with phase mask and mirrors.

The weak spot of the 4f-geometry is the use of the lenses which are, corresponding to their spherical shape and also due to their complex production, a serious source for errors, not to mention chromatic aberration. We therefore replaced the lenses by parabolic mirrors. That rids us of the problems provided

that we keep in mind that imaging with a parabolic mirror is only more precise than it would be with a lens if the angle between incoming and outgoing beam is small. Since the mirrors have to be placed at the side of the mask only angles of at minimum 12° can be achieved being definitively too big. Therefore a reconstructed version of the setup, as schematically shown in fig. 2.6, is used. Here each lens is replaced by a combination of a parabolic and a plane mirror. This allows on one hand for beams close to the principal axis and is on the other hand a way of saving space.

2.2.4 Amplitude modulation with a phase mask

An important point is furthermore that even if we are using a phase mask we are still capable of doing amplitude modulation. With the previous considerations of this chapter the concept of this idea can now be explained.

The first idea for pulse shaping was to group the pixels in adjacent pairs, each assigned to one frequency. This idea bases on interference:

If the wave hitting the mask is known,

$$E_{\text{in}} = E_{0i}\exp\{\mathrm{i}\phi_{\text{i}}\} \tag{2.9}$$

and in addition the wave desired in the end,

$$E_{\text{out}} = E_{0o}\exp\{\mathrm{i}\phi_{\text{o}}\}\,, \tag{2.10}$$

one can define a transfer function out of it:

$$E_{\text{in}} \cdot E_{\text{trans}} = E_{\text{out}} \tag{2.11}$$

$$E_{\text{trans}} = \frac{E_{0o}}{E_{0i}}\exp\{\mathrm{i}(\phi_{\text{o}} - \phi_{\text{i}})\} = \mathrm{E}_{0t}\exp\{\mathrm{i}\phi_{\text{t}}\} \tag{2.12}$$

Unless only the phase lag induced by the display can be controlled, eq. 2.12 is transformed to

$$E_{\text{trans}} = E_{0t}\exp\{\phi_{\text{t}}\} = \exp\{\mathrm{i}\phi_{\text{y}}\} \tag{2.13}$$

where

$$\phi_y = \phi_o - \phi i \pm arccos\left(\frac{1}{2}\frac{E_{0o}}{E_{0i}}\right) \tag{2.14}$$

because of

$$\frac{1}{2}\frac{E_{0o}}{E_{0i}} = \operatorname{Re}\exp\{\mathrm{i}\phi*\} = \cos(\phi*)\,, \tag{2.15}$$

Observing two neighboring pixels, with + and - chosen contrary

$$E_{\text{out}}^{I} = I\exp\{\mathrm{i}\,\phi_{\text{i}}\} \cdot \exp\left\{\mathrm{i}\left((\phi_{\text{o}} - \phi_{\text{i}}) + \arccos\left(\frac{1}{2}\frac{\mathrm{E}_{0o}}{\mathrm{E}_{0i}}\right)\right)\right\} \tag{2.16}$$

$$E_{\text{out}}^{II} = I\exp\{\mathrm{i}\,\phi_{\text{i}}\} \cdot \exp\left\{\mathrm{i}\left((\phi_{\text{o}} - \phi_{\text{i}}) - \arccos\left(\frac{1}{2}\frac{\mathrm{E}_{0o}}{\mathrm{E}_{0i}}\right)\right)\right\} \tag{2.17}$$

and then letting the transmitted functions interfere, one gets

$$E_{\text{out}}^{I} \quad + E_{\text{out}}^{II} = E_{0i}\exp\{\text{i}\,\phi_{\text{i}} + \text{i}\,\phi\text{o} - \text{i}\,\phi\text{i}\}$$
$$\left(\exp\left\{\text{i}\arccos\left(\frac{1}{2}\frac{\text{E}_{0\text{o}}}{\text{E}_{0\text{i}}}\right)\right\} + \exp\left\{\text{i}\arccos\left(\frac{1}{2}\frac{\text{E}_{0\text{o}}}{\text{E}_{0\text{i}}}\right)\right\}\right) \quad (2.18)$$

$$= E_{0i}\exp\{\text{i}\,\phi_{\text{o}}\}\left(2\cos\left(\arccos\left(\frac{1}{2}\frac{\text{E}_{0\text{o}}}{\text{E}_{0\text{i}}}\right)\right)\right) = \text{E}_{0\text{o}}\exp\{\text{i}\,\phi_{\text{o}}\}\,. \quad (2.19)$$

That means that with a known entrance function a free selectable exit function can be generated using a transfer function defined by these two functions.

The transfer function was planned to be calculated by a self made program that should regulate the voltage to be applied to each pixel for realizing the function.

As it turned out, there is a much more simple method for amplitude modulation with a phase mask. Applying a continuous function to the pixels can do the trick as well. If one, for instance, puts a sinus-shaped function on the mask the back transformation of the manipulated beam gives a double-pulse. The preconditions thereby are ideal conditions such as a continuous phase modulation. Since in reality the phase function will be stepwise due to the limited pixel size a control program could compensate these errors.

Challenges and drawbacks of the setup based on a phase mask

As an example two possible sources for errors are mentioned here.

- The gratings are positioned with their center in the focus of the parabolic mirror on each side of the mask. Unfortunately the beam hitting the mirror has a certain width, i.e. a certain frequency can not be focused on a single pixel but instead to a group a several pixels. Therefore the phase shift of a single pixel is applied to several frequencies respectively spatially separated parts of a single frequency experience different phase shifts. The phase mask is quasi a grating on its own, with each pixel having a defined phase and leaving parts of the spectrum unmodified in between the pixels. Therefore diffraction effects are expected.

- It is not likely that the pulse leaving the pulse shaper after applying just a theoretically calculated function to the mask will show the desired shape. For this reason the function should be controlled by a computer and be modified by a self learning algorithm until the outgoing beam fits the given shape with a certain accuracy [30]. For this purpose the beam leaving the pulse shaper is directed towards an autocorrelator with an oscilloscope attached. The information about the pulse shape is sent back to the computer that recalculates the transfer function and modifies the voltage applied to the mask correspondingly.

2.3 Practical realization of a pulse shaper using a phase mask

In this section the individual parts of the setup are described. I will show the status of the hard- and software and conclude with some example figures.
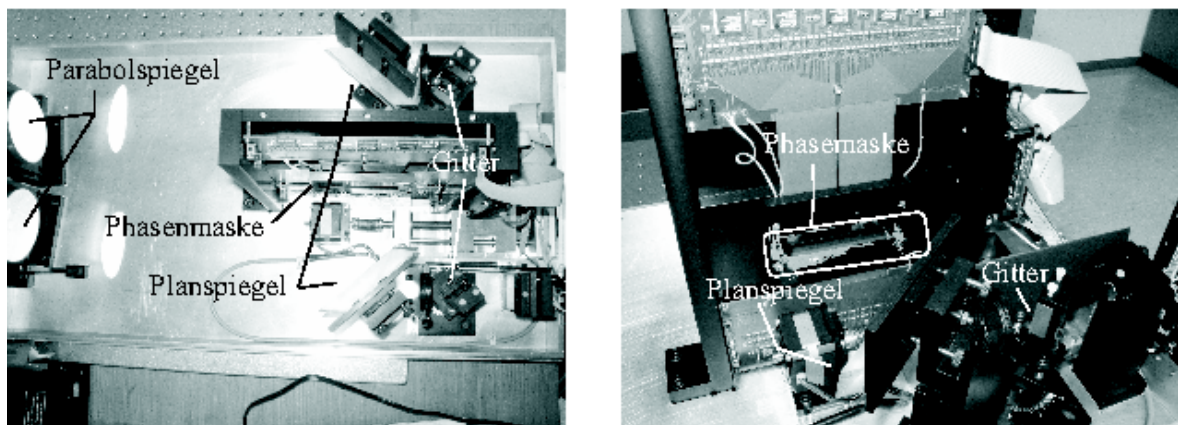
2.3.1 Hardware

Figure 2.7: Photography of the pulse shaper.

Fig. 2.7 shows a photography of the pulse shaper. All previously mentioned parts are labeled. Additionally the stepper motor is visible which turns the grating to move the central frequency of the beam to the central pixel of the device which allows for using the pulse shaper with beams of different wavelengths.

2.3.2 Software

The current status of the user interface is shown in fig. 2.8. It consists of several control units: In the upper right corner the user can choose the shape of the incoming and outgoing beam. At the moment one can choose between a Gaussian, Lorentz or sech shape or one can import a user-defined function. The two diagrams on the right show the chosen pulses. It is possible to plot either intensity or amplitude depending on time, frequency or space (either real space or k-space). The possibility of directing a certain frequency to a certain pixel is implemented at the center part of the left. The third diagram allows for monitoring the transfer function after its calculation and was planned to be removed with completion of the user interface. Some other boxes would not be part of the final version, too. They control function tests or are used for the calibration of the pulse shaper. No self-learning algorithm was implemented at the current state.
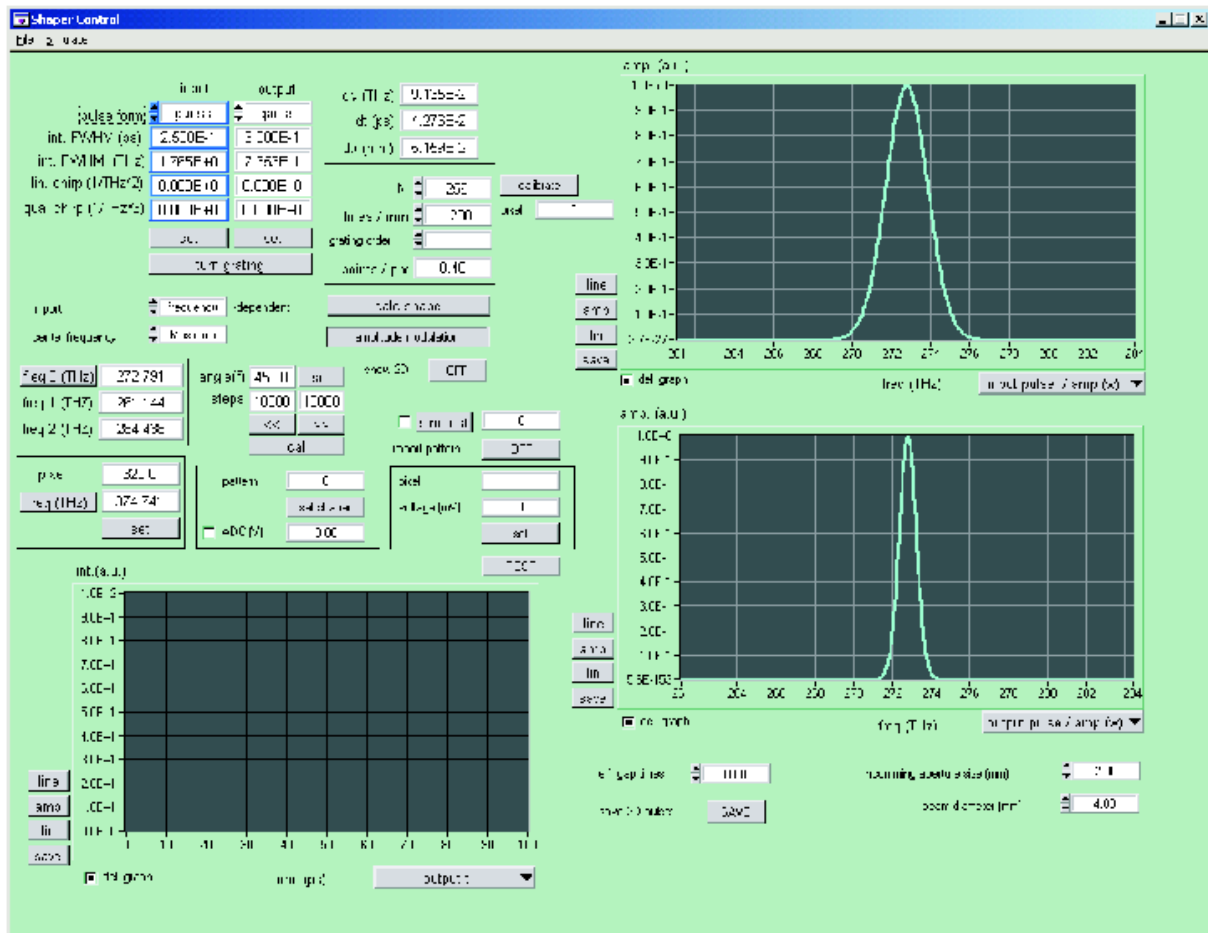
Figure 2.8: Screenshot of the user interface of the control program of the pulse shaper.
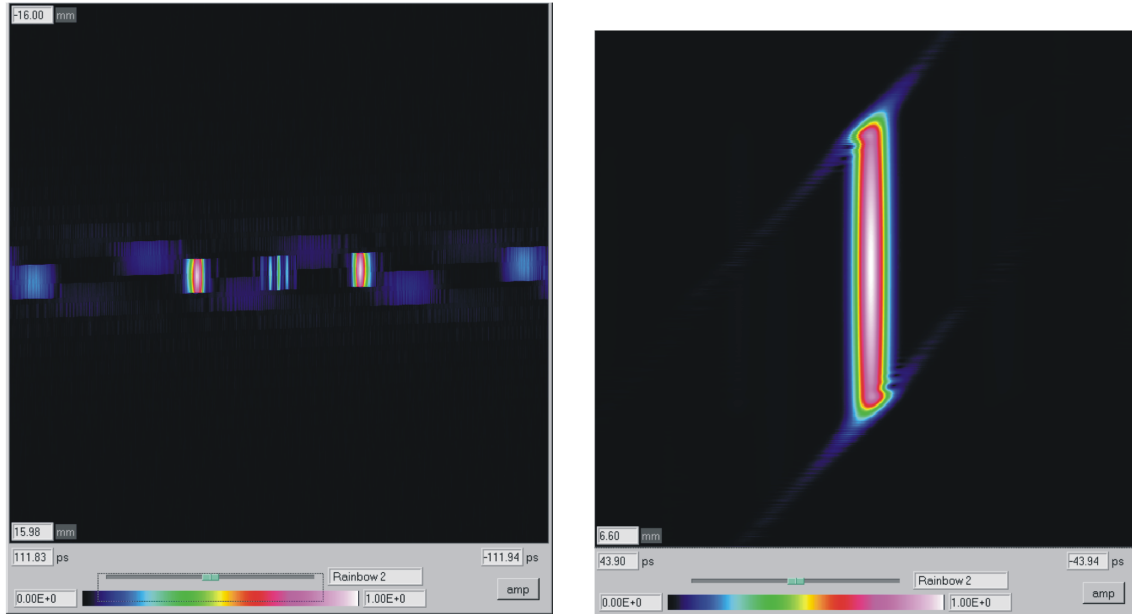
2.3.3 Examples

Figure 2.9: Screenshot of two different calculations made during the creation of the routine to determine the transferfunction.

In fig. 2.9 two typical pictures are shown, that were reached during the development of a routine to create the transfer function. The left of the figure shows what is expected to be the outcome if a Gaussian beam is transformed to be separated in three parts. The effect of the mask being a grating is clearly visible. The right part of this figure shows a close look to a central peak of another transformation. These calculation stay on a level, where the transfer function is calculated directly. No self-learning technic is implemented here. Things that where taken into account are the geometry of the liquid crystal mask (including the gaps between the single pixels) and the size of the aperture at the entrance of the pulse-shaper. Up to now, no measurements for comparison were performed.

2.4   Pulse train generation with a two-stage Michelson interferometer

In this section the final solution for generating the desired pulse-trains will be discussed.

Previous to the setup itself we introduced two Michelson-interferometers into the beam-path that allow us to create short pulse-trains of up to 4 pulses (one or two are still possible by blocking the corresponding mirrors) with a temporal separation between 0.5 and around 10 ps (This corresponds to repetition rates of up to 2 THz). To assure that all pulses have the same energy part of the beam is directed to an autocorrelator.

A schematic drawing of the Michelson-interferometers and the mechanism of pulse-train creation supported by autocorrelation-spectra are shown in figure 2.10.
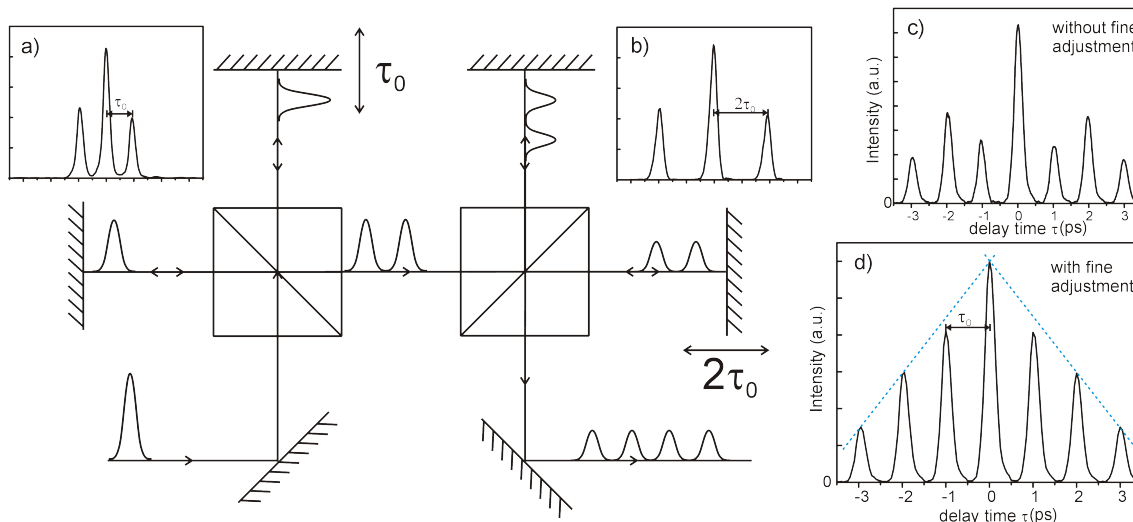

Figure 2.10: Sketch of the two stage Michelson-interferometer and autocorrelation spectra of different stages of the four-pulse train generation. In the final pulse train (d) each pulse contains the same energy.

The beam enters on the lower left and is split by a 50:50 beam-splitter cube. One of the beam parts hits a fixed mirror the other one a movable mirror. This mirror is displaced to the other one to generate a delay time τ_0 between the beam parts. Both beams hit again the beam splitter and enter the next Michelson interferometer. It works exactly the same as the first one with the difference being the delay time doubled. The process of pulse-train creation is controlled by checking the autocorrelation of the pulse train in each step.

The autocorrelations a) and b) are taken while using just one of the Michelson interferometers. This is achieved simply by blocking one mirror in the other Michelson interferometer. One can see that the delay times of the two Michelson interferometers is different, the first one has the desired delay time τ_0 and the other one the doubled. The autocorrelation is a convenient tool to estimate whether the beams contain the same energy although it can not provide a number. Part

c) of fig. 2.10 shows an autocorrelation of a complete four-pulse train with bad alignment. If all pulses contain the same energy the autocorrelation spectrum looks like fig. 2.10 d). In a separate measurement we calculated the energy per pulse to be 0.1 pJ.

The implementation and operation of a two-stage Michelson interferometer for pulse-train generation is easier by far than the construction and programming for using a LCD-mask based pulse shaper presented throughout the latter sections. Nevertheless the pulse shaper exists and waits for completion. Maybe further applications will need a more complex pulse shape than it can be provided by the Michelson interferometers which could lead to a revival of this project. In addition also the Michelson interferometers can be improved by automating the movement of the movable mirrors and allowing for a computer control of the pulse-train delays.

Chapter 3

Ultrafast gain dynamics of quantum dot based semiconductor optical amplifiers

In this chapter our first attempt to achieving a complete gain-recovery is shown and discussed. The pulses used for study here are single-pulse, double-pulse or four-pulse train. They are resonant to the ground or excited state. All measurements were performed at room-temperature (300 K) and under high optical pumping-conditions explained in the first chapter.

3.1 Interpreting differential transmission spectroscopy (DTS) graphs

Starting with simple single pulse experiments (resonant to the ground state) I want to explain how the graphs of the differential transmission spectroscopy have to be interpreted. In fig. 3.1 some graphs of such a measurement are shown for different injection currents. They represent the gain of the device in dependence of the delay between pump- and probe-beam. The gain is calculated from the measured amplitude A following the expression

$$\Delta G(\text{dB}) = 20 \log(\text{A}/\text{A}_0) \,, \tag{3.1}$$

where A is the amplitude of the probe-beam measured with the pump-beam running while A_0 is the amplitude without pump-beam. This description is equal to the picture of the ratio between the transmitted intensity and the intensity in front of the device.

3.1.1 Analyzing the graphs

The three population-cases already introduced in chapter one are distinguishable again. At low injection-currents in the case of low carrier-densities the graph (red) shows absorption. At currents around 7.5 mA the case of transparency is
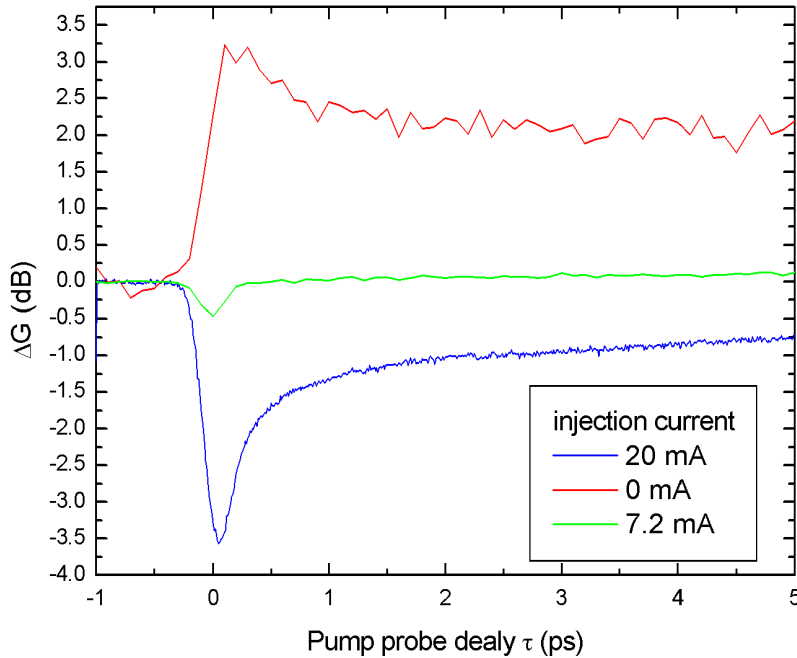
Figure 3.1: Pump probe curves measured at different injection currents to show the different cases of high (red) and low (blue) carrier densities and the case of transparency (green).

visible (green) and at high injection currents, that create the case of high carrier-densities, gain is visible (blue).

Following fig. 3.2 the effects creating the different curves will be explained. To keep things simple assume that the probe-beam enters the sample after the pump-beam.

First the case of *low carrier-density* is explained (see upper part of fig. 3.2):

All quantum dots are empty at the arrival of the pump-beam. Corresponding to the intensity of the beam excitons are created in the ground state of the quantum dots. The incoming probe-beam is amplified by the stimulated recombination of the available excitons. As the delay between pump- and probe-beam is extended, the probe-beam faces existing excitons more seldom. The excitons may have changed their energy-level to the excited state or to the surrounding material of the quantum dot or their carriers recombined already in advance of the probe-beams arrival.

The next case to be discussed is the case of a *high carrier-density* (see lower part of fig. 3.2):

At the arrival of the pump-beam the ground- and even the excited state are populated with excitons. Its photons stimulate a recombination of excitons leading to an amplification of the pump-beam. Therefore these excitons are not present anymore at the arrival of the probe-beam. Now the photons of the probe-beam

low carrier-density:
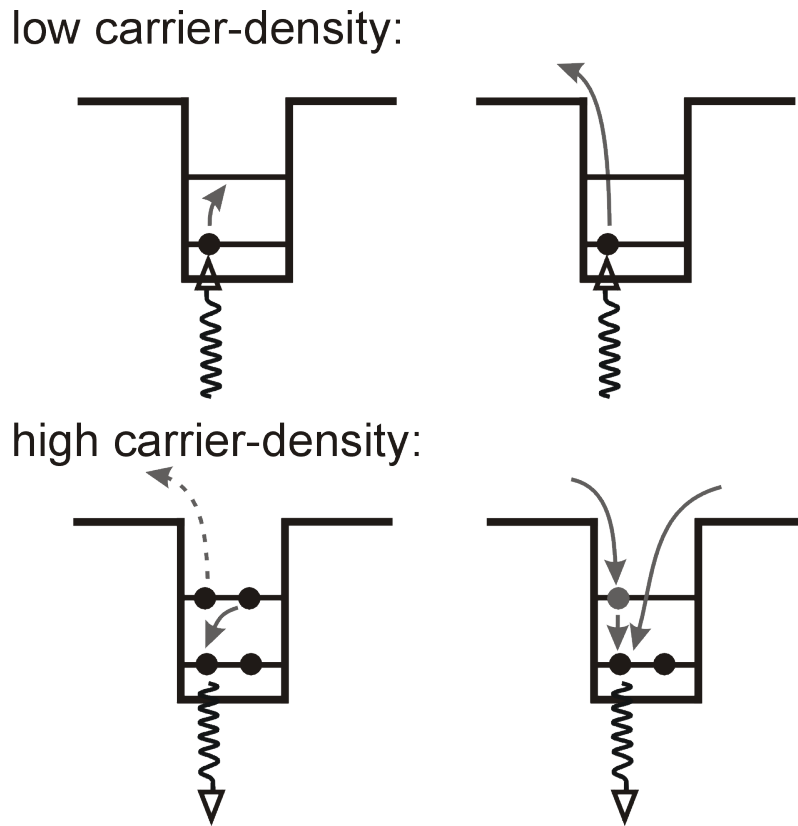

high carrier-density:

Figure 3.2: Schematic drawing of the different effects explaining the transmission of pump- and probe-beam in the case of low (top) and high (bottom) carrier density.

are absorbed creating excitons themselves. A delay between pump- and probe-beam offers scattering-processes the possibility to take place in the meantime repopulating the quantum dot ground state. The scattering can include again the excited state as well as the quantum dot surrounding material.

In case of *transparency* the curve seems to be uninfluenced by the transmission through the device:

This injection current region provides an amount of carriers to fill the quantum dot ground state with one exciton in average. That leads to an even possibility of pump- and probe-beam to be either amplified by stimulated emission or be absorbed to create another exciton.

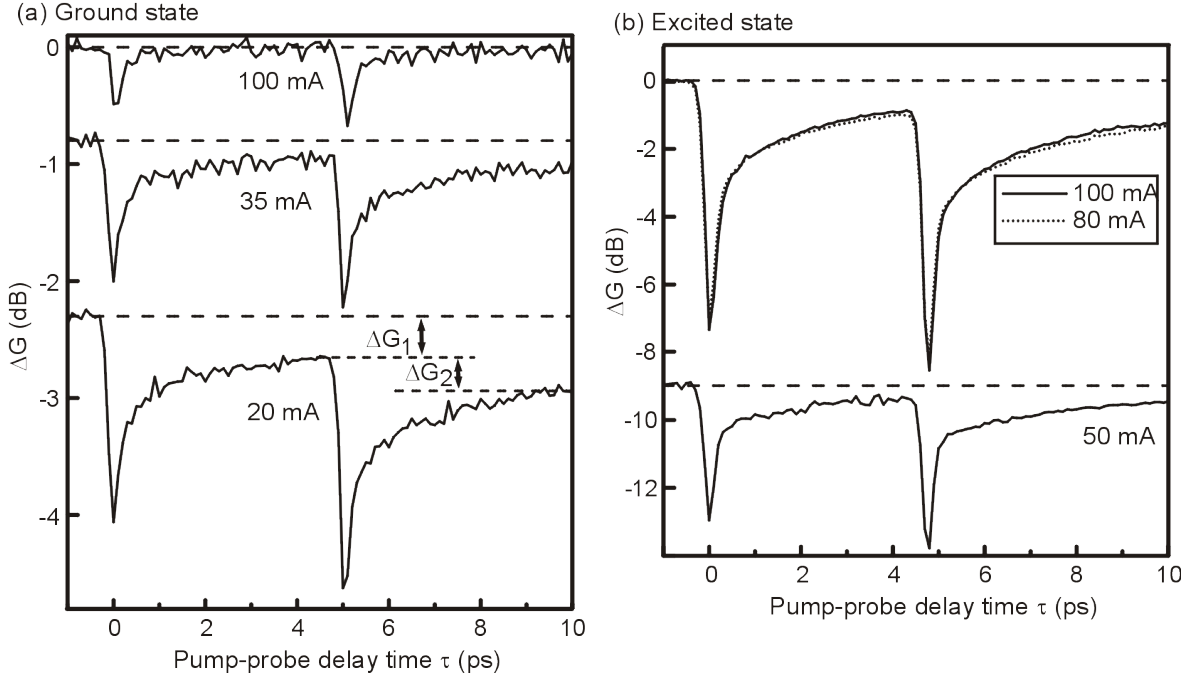## 3.2   Complete gain recovery and its conditions

Figure 3.3: Dynamics of gain recovery (a) in the ground state and (b) in the excited state, for different values of injection current.

Now having the tools to discuss more complex gain-curves I want to proceed with our first attempt of showing complete gain recovery after a 200 GHz double-pulse. Using one Michelson interferometer a pulse-train of two 150 fs long pulses having a temporal distance of 5 ps (equivalent to the 200 GHz repetition rate) was created and directed through our device. The measurements were done at wavelengths resonant to the ground and to the excited state.

The temporal evolution of the ground- and excited-state gain $\Delta G(\tau)$ induced by the two pump-pulses is shown in fig. 3.3 for different injection currents. An ultrafast and complete gain recovery is achieved for the ground state at high injection currents (100 mA in 3.3(a)) after both pump-pulses. Decreasing the injection current prolongates the gain recovery and the second beam faces a partial gain reduction compared to the first beam. For the excited state no complete gain recovery can be achieved for any available injection current (see 3.3(b)).

A quantitative comparison of the gain reduction factors induced by the first, $\Delta G_1 = \Delta G(5\text{ps})$, and second pump-pulse, $\Delta G_2 = \Delta G(10\text{ps}) - \Delta G_1$, is shown in fig. 3.4 and marks the first step toward an understanding of the amplification of longer (more than two pulses) pulse trains.

For low injection currents both absolute values of ΔG_1 and ΔG_2 decrease with increasing current up to $I_0 \simeq 20$ mA where a minimum is reached. While increasing more they reach values of zero at high currents around 100 mA when a complete gain recovery is achieved. Taking a look back at the spectra of the amplified spontaneous emission e.g. in fig. 1.18 one can observe that I_0 coincides

with the appearance of the excited state. This observation emphasizes the importance of the excited states population for the ultrafast refilling of the ground state. This fits with the conclusion Urayama et al. [31] stated, that the recovery of the ground state can be distinctly accelerated by a significant excited state population. For the excited state $\Delta G_{1,2}$ decreases until it saturates at $I_0 \sim 80 - 100$ mA (see also the curves for 80 and 100 mA in fig. 3.3). The zero-line transition of $\Delta G_{1,2}$ at around 40 mA corresponds to the transparency current of the excited state that in gain measurements was found to be at 37.5 mA.

$|\Delta G_1| > |\Delta G_2|$ is obvious for ground and excited state from fig. 3.4. If the intradot recovery, excited to ground state, would be the only source for refilling the ground state, the partial depletion of the excited state after the first beam would lead to an increasing reduction of the gain after the second beam [3]. This is contradictory to our observation. Therefore we conclude that direct capture from the wetting layer participates in the recovery of the ground state, too.

Following chapters will show studies in direction of proving this thought by comparison of experiment with two theories covering different areas of the delay time between pump- and probe-beam.
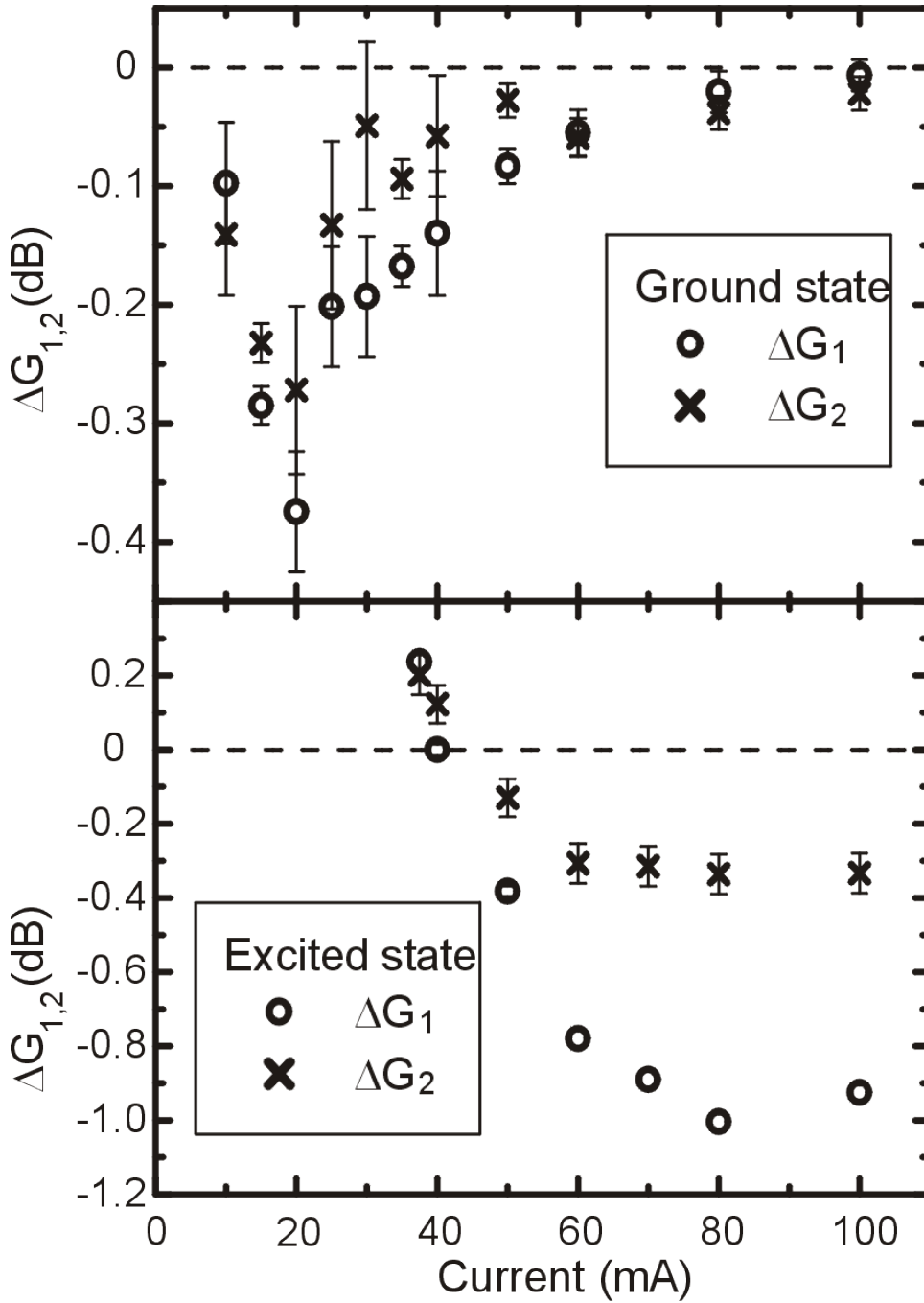
Figure 3.4: Gain reduction ΔG_1 and ΔG_2 induced by a double pump pulse in the ground and excited state.
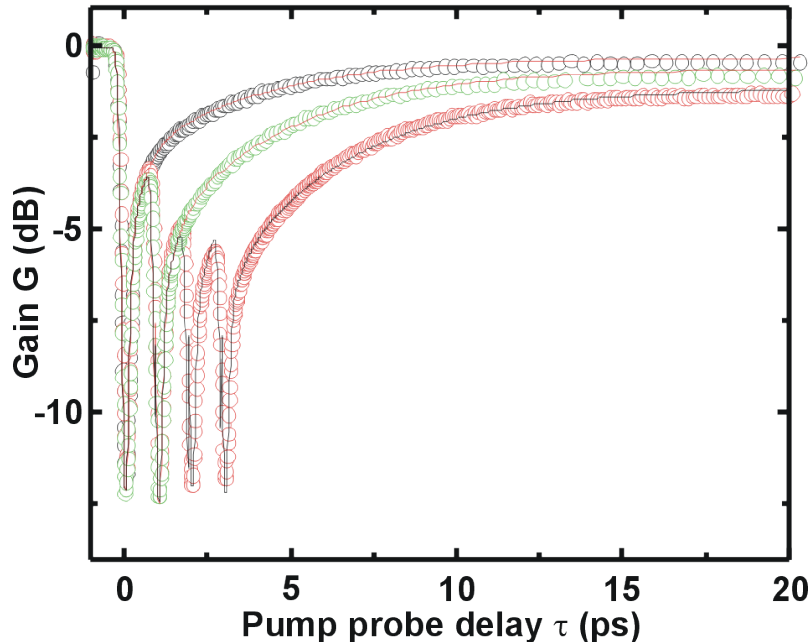
3.3 Multiexponential fit of DTS curves

Figure 3.5: Gain dynamics after amplification of 1, 2 and 4 pulses at an injection current of 40 mA. The solid lines correspond to multi-exponential fittings of the experimental data as described in the text.

In order to have a first quantitative analysis of the heterodyne pump and probe measurements, it is quite common to use a fitting expression [32, 33, 34]: three exponential decays plus an offset term analytically convoluted to the gaussian response of the system. We apply it to our pump and probe data for 1, 2 and 4 pulse trains in the gain regime (I_c=10-150 mA), see fig. 3.5. The physically interesting time constants retrieved from the fit are the two fastest, τ_1 and τ_2 which are plotted along with their relative weighting in fig. 3.6. The slowest component (τ_3) is in the range of quantum dots radiative lifetime and its relative weight decreases quickly with current, becoming negligible above I_c =20-30 mA.

The results obtained for τ_1 and τ_2 from the fitting routines are plotted in logarithmic scale in figure 3.6 (a). For single pulse experiments it holds a relation of $\tau_3 \approx 10 \cdot \tau_2 \approx 100 \cdot \tau_1$ for the retrieved time constants.

For $I_c < 30$ mA, i.e. carrier injection currents close to the transparency current I_{tr}, τ_1 and τ_2 increase with increasing I_c. Such a behavior can be assigned to an inhomogeneous absorption process during the propagation of pulses through the waveguide. Therefore the focus will be on the discussion of results from moderate to high injection currents, $I_c > 30$ mA, i.e. those accelerating the gain recovery, as seen in figure 3.6.

In that range of $30 < I_c < 40$ mA, both τ_1 and τ_2, strongly decrease with increasing I_c followed by a nearly constant behaviour for $I_c >60$ mA. In addition, the relative weight of the fastest component (the τ_1 weight) grows until it
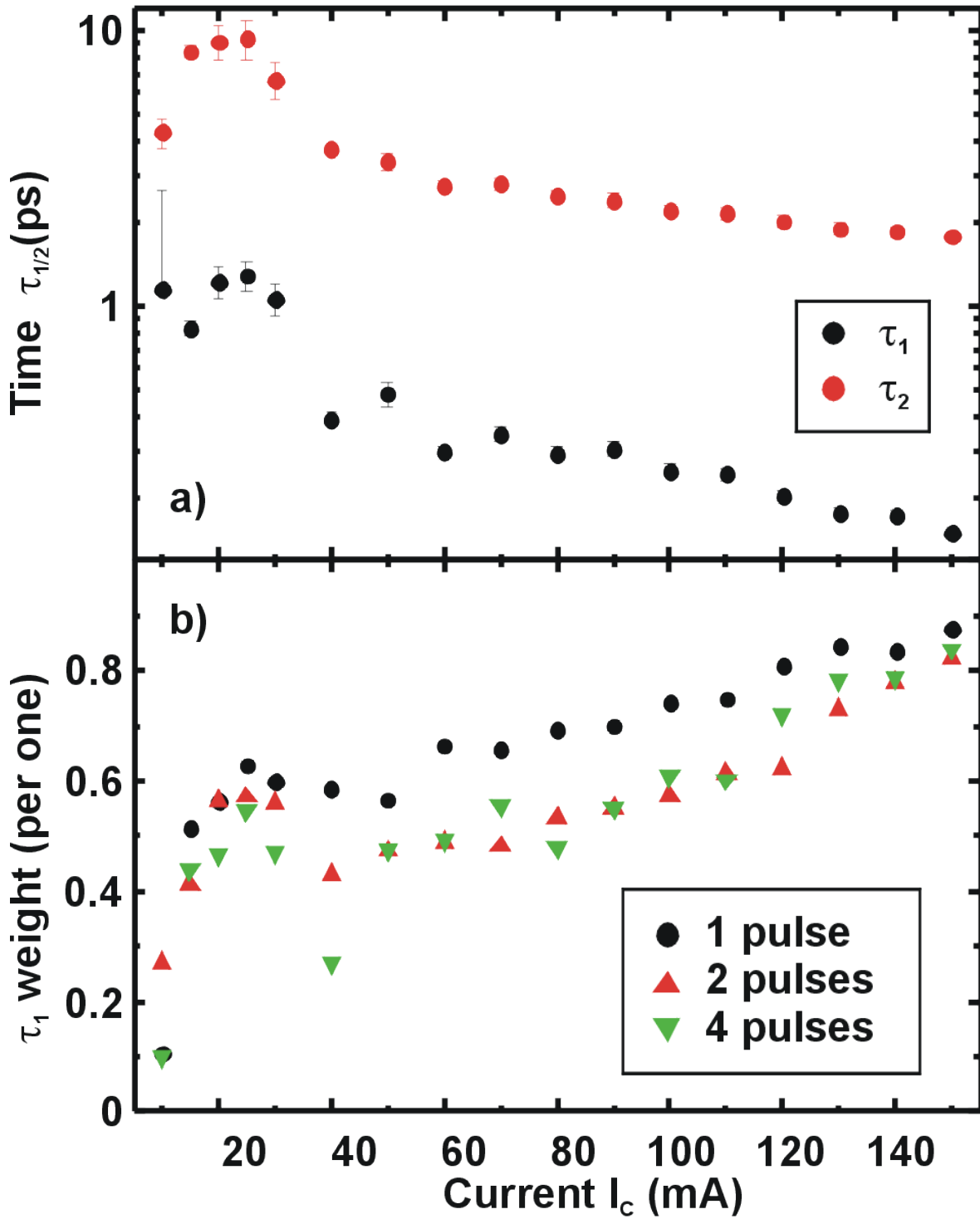
Figure 3.6: (a) Time constants τ_1 and τ_2 derived from the fitting as described in the text. (b) Relative weight of the fastest component, τ_1, as a function of injection current I_c.

comprises 90% of the total recovery dynamics at $I_c = 150$ mA.

For the following analysis of the experiments with 2 and 4 pulses in the train, τ_1 and τ_2 are fixed to the values obtained from the fits of the corresponding single pulse experiments. As can be seen in fig. 3.5, all fits, as described above, show good agreement with the experimental data.

For all three experiments with 1, 2 and 4 pulses, we found a systematic decrease of τ_1 along with an increase in its weight when I_c is increased. Therefore we discuss in the following only that fastest component τ_1 relative weight, as presented in figure 3.6 (b). From the experimental result we can state that an increase (decrease) of τ_1 relative weight corresponds to a speed up (slow down) of the gain recovery dynamics. Under conditions of powerful electrical injection, the τ_1 relative weight reduces only gradually after amplification, even if the power per pulse used is sufficient to fully deplete the ground state population inversion (see chapter 1). τ_1 weight decreases slowly from single pulse to double pulse experiments and remains almost unchanged when comparing 2 and 4 pulse trains dynamics. The microscopic background of that τ_1 time constant is nonlinear Coulomb scattering in a thermal non-equilibrium situation and subject of the next chapter.

Chapter 4

Impact of Coulomb scattering on the ultrafast gain recovery

In this chapter, the ultrafast gain recovery in quantum dot semiconductor optical amplifiers is addressed by a microscopic approach containing the semiconductor Bloch equations for the polarization and population dynamics. The incorporated microscopically calculated Coulomb scattering rates describe the Auger transitions between localized quantum dot and continuous wetting layer states. The Coulomb interaction is found to strongly influence the gain dynamics of quantum dot amplifiers. The calculations performed throughout this chapter were done by Dr. Ermin Malić performed under the supervision of Prof. Dr. Andreas Knorr.

4.1 Deriving Coulomb scattering rates

As described in chapter one our sample contains several layers of quantum dots. A sketch of a corresponding quantum dot-wetting layer system is shown in fig. 4.1 a).

Figure 4.1b demonstrates the dynamics of an electrically pumped quantum dot amplifier. If one considers the direct capture from the wetting layer to be important only the energetically lowest electron and hole levels in quantum dots have the main contribution to the system dynamics. That leads to a two-level system for electrons and holes. The continuous wetting layer states are filled with carriers by the injected current. The Coulomb interaction leads to a capture of electrons and holes into the bound quantum dot states from where they relax radiatively via spontaneous or induced emission. The corresponding scattering and radiative processes are described within an approach combining the semiconductor Bloch equations (derived in sec. 1.5) with microscopically calculated Coulomb scattering rates. These are determined by considering the Coulomb interaction up to the second order in the screened Coulomb potential. In the gain regime, where the carrier density in the wetting layer is high, the capture dynamics within the quantum dot-wetting layer structure is assumed to be dominated by Coulomb scattering (nonlocal Auger recombination).[35, 36]. Therefore electron-phonon processes are of less importance, and thus will be neglected.

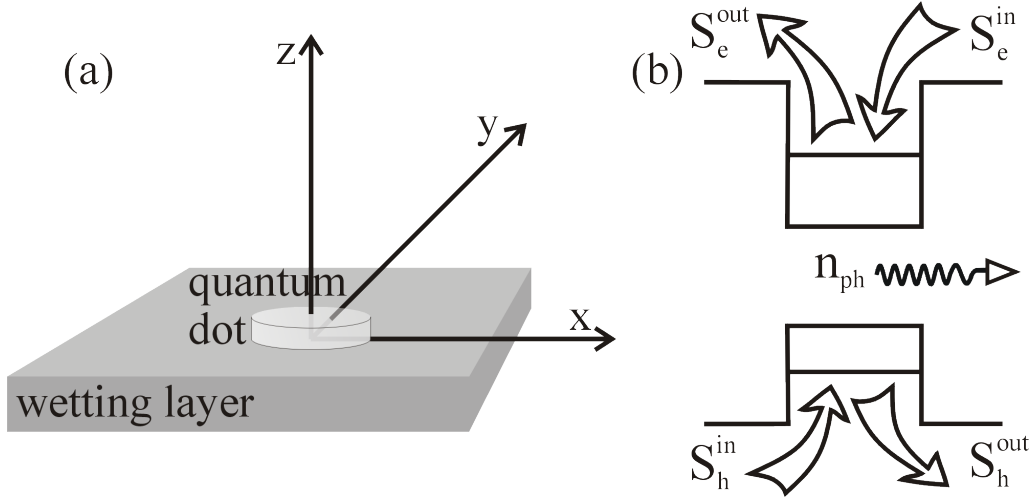The quantum dots in a layered structure such as ours are known to have

Figure 4.1: (a) Structure of a quantum dot and the surrounding wetting layer. (b) Sketch of the in and out scattering of electrons and holes due to Coulomb interaction described by the rates S^{in} and S^{out}. n_{ph} describes the density of the thereby generated photons.

lens-like shapes. In such a case the ground state wave function has cylindrical symmetry [37].

Since the confinement in the z-direction of our system is much stronger than within the x-y-plane (see fig. 4.1) the wave function of that system can be divided in an in-plane part and a z-component.

The in-plane energy of the charge carriers in wetting layer states is calculated within the effective-mass approximation [38], see sec. 1.1.2. The energy of charge carriers in quantum dots is determined by simple levels $E_{b,n}$ with $b = e, h$ and $n = 0, 1, 2, ...$. The energies of bound quantum dot states for a quantum dot of an assumed width of 17 nm is found to be for the electron ground state $\varepsilon_e = 240\,\text{meV}$ and for the hole ground state $\varepsilon_h = 105\,\text{meV}$ with respect to the energy of the wetting layer edge corresponding to [39].

The wave function for the entire quantum dot-wetting layer system yields within the effective mass approximation [38]

$$\Psi_{i,\sigma}^b(\boldsymbol{r}) = \varphi_i^b(\boldsymbol{\rho})\, \xi_\sigma^b(z)\, u^b(\boldsymbol{r})\,, \tag{4.1}$$

where $u^b(r)$ are Bloch functions with $b = e, h$, $\varphi_i^b(\boldsymbol{\rho})$ is the in-plane part of the wave function, and $\xi_\sigma^b(z)$ is the z-component of the wave function with the quantum number σ. The in-plane component of the wave function for lens-shaped quantum dot with a small aspect ratio (considered height: 4nm) can be approximated by the eigenfunctions of a two-dimensional harmonic oscillator[40, 19]. Assuming that only the ground state is of importance for scattering processes, the oscillator energy $\hbar\omega_b$ corresponds to the quantum dot ground state energy ε_b.

The z-component of the wave function corresponds to the eigenfunctions of a finite barrier well. These eigenfunctions are independent of the carrier type b.

For a small wetting layer thickness and a small quantum dot height, the energy spacing of the levels due to the confinement in the z-direction is large. Therefore,

it is sufficient to consider only the lowest quantum number $n = 0$. In addition it is assumed that the quantum dots and the wetting layer share the same height leading to the same z-confinement for both. In this case, the confinement of the investigated quantum dot-wetting layer system is completely given by the strain in the x-y plane[38].

The in-plane component of the wave function of the wetting layer states is described by orthogonalized plane waves (OPWs)[41]

$$\varphi_{\boldsymbol{k}}^b(\rho) = \frac{1}{N_b(k)} \left[\exp(i\boldsymbol{k} \cdot \boldsymbol{\rho}) - 2\alpha_b(k) \exp\left(-\frac{1}{2}\beta_b^2 \rho^2 \right) \right] \tag{4.2}$$

with

$$N_b(k) = \sqrt{1 - \frac{4\pi}{A\beta_b^2}\alpha_b^2(k)} \tag{4.3}$$

given by the the normalization condition $\langle \varphi_{\boldsymbol{k}}^b | \varphi_{\boldsymbol{k}}^b \rangle = 1$.

The OPW approach takes the influence of the confinement potential into account and is therefore more realistic than a plane wave description.
For describing the dynamics of quantum dot amplifiers the light-matter interaction and the Coulomb interaction are taken into account. Their strengths are given by the optical matrix element in the first case and the Coulomb matrix element in the second case. The optical matrix element is calculated using an interband dipole moment d_{vc} according to the experimental results, in the range of $0.3 - 0.6\,e_0$nm.

Starting with the carrier-carrier Hamiltonian (see also sec. 1.5) we consider the capture of carriers from one of the continuous wetting layer states denoted by the wave vectors $\boldsymbol{k}$ into the electron or hole quantum dot ground state. Since the carriers are completely localized within the quantum dots, the wave vector $\boldsymbol{k}$ can not be well defined.

These capture processes are described by the Coulomb matrix element $V_{b\boldsymbol{k}_1, b'\boldsymbol{k}_3}^{b,\ b'\boldsymbol{k}_2}$, using the wavefunctions calculated previously in this section. Figure 4.2 illustrates the Coulomb interaction. It involves always two particles. One carrier $((b, \boldsymbol{k}_1))$ is captured into a quantum dot state b and another carrier is shifted within the wetting layer to conserve the energy of the process.

The rates corresponding to the Coulomb scattering are calculated microscopically as a function of the wetting layer electron and hole density w_e and w_h. As shown in Sec. 1.5, the Coulomb contributions are taken into account up to the second order Born approximation, yielding the Boltzmann equation[22, 42]

$$\frac{d}{dt}\rho_b = S_b^{in}(1 - \rho_b) - S_b^{out}\rho_b = -\frac{1}{T_{1,b}}\rho_b + S_b^{in}. \tag{4.4}$$

where ρ_b is the occupation probability in the electron or hole quantum dot state ($b = e, h$) and T_1 is the population scattering time. The Boltzmann equation contains Coulomb in- and out-scattering rates S_b^{in} and S_b^{out}
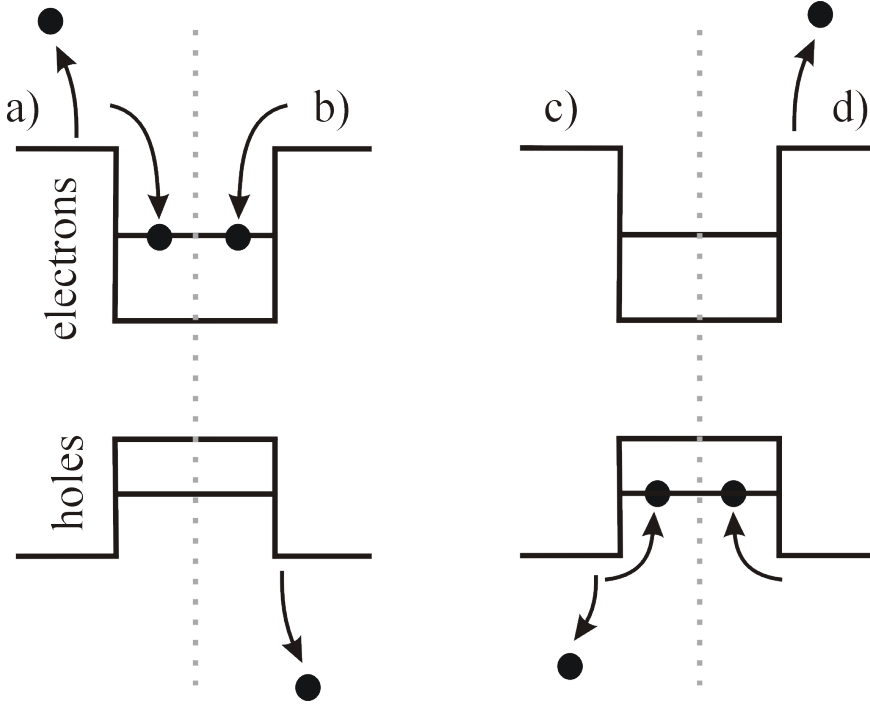
Figure 4.2: Illustration of the different scattering processes for electrons and holes. Figure parts (a) and (c) show pure scattering (electron-electron and hole-hole) and figure parts (b) and (d) show mixed scattering (electron-hole and hole-electron).

$$S_b^{in/out} = \frac{2\pi}{\hbar} \sum_{\boldsymbol{k}_1 \boldsymbol{k}_3 \boldsymbol{k}_2 b'} W_{b\boldsymbol{k}_1, b'\boldsymbol{k}_3}^{b, \ b'\boldsymbol{k}_2} \left(2 W_{b\boldsymbol{k}_1, b'\boldsymbol{k}_3}^{b, \ b'\boldsymbol{k}_2 *} - \delta_{b,b'} W_{b'\boldsymbol{k}_3, b\boldsymbol{k}_1}^{b, \ b'\boldsymbol{k}_2 *}\right)$$

$$f_{\boldsymbol{k}_1 \boldsymbol{k}_2 \boldsymbol{k}_3 b'}^{in/out,b} \delta\left(\varepsilon_0^b + \varepsilon_{\boldsymbol{k}_2}^{b'} - \varepsilon_{\boldsymbol{k}_1}^b - \varepsilon_{\boldsymbol{k}_3}^{b'}\right) \tag{4.5}$$

with the characteristic functions for in- and out-scattering

$$f_{\boldsymbol{k}_1 \boldsymbol{k}_2 \boldsymbol{k}_3 b'}^{in,b} = \rho_{\boldsymbol{k}_1}^b \rho_{\boldsymbol{k}_3}^{b'} (1 - \rho_{\boldsymbol{k}_2}^{b'}) \ \text{ and } \ f_{\boldsymbol{k}_1 \boldsymbol{k}_2 \boldsymbol{k}_3 b'}^{out,b} = \rho_{\boldsymbol{k}_2}^{b'} (1 - \rho_{\boldsymbol{k}_3}^{b'})(1 - \rho_{\boldsymbol{k}_1}^b). \tag{4.6}$$

The sum in eq. (4.5) runs over all wetting layer states (occupation probabilities $\rho_{\boldsymbol{k}_1}^b, \rho_{\boldsymbol{k}_3}^{b'}$, and $\rho_{\boldsymbol{k}_2}^b$). The respective single particle energies in the wetting layer are denoted by $\varepsilon_{\boldsymbol{k}_1}^b, \varepsilon_{\boldsymbol{k}_2}^{b'}, \varepsilon_{\boldsymbol{k}_3}^{b'}$ and in the quantum dot by ε_0^b. The summation over spin leads to a factor 2 in front of the direct term assuming that the wetting layer population is independent of the carrier spin. It also accounts for the Kronecker symbol in front of the exchange term. In case electrons and holes with anti-parallel-spin collide the interference vanishes leaving only contributions of pure electron-electron and hole-hole scattering processes [43].

In addition, it is assumed that the carrier distributions are close to the quasi-equilibrium Fermi distributions, i.e. $\rho_{\boldsymbol{k}}^b = f_{\boldsymbol{k}}^b + \delta f_{\boldsymbol{k}}^b$ with $\delta f_{\boldsymbol{k}}^b \ll 1$ and the Fermi-

Dirac distribution

$$f_{\boldsymbol{k}}^b = \frac{1}{1 + \exp\left(\frac{1}{k_b T}\left(\varepsilon_{\boldsymbol{k}}^b - \mu_b(T, w_b)\right)\right)} \tag{4.7}$$

and the quasi-Fermi level $\mu_b(T, w_b)$. This can be obtained analytically in the two-dimensional case [44], yielding

$$\mu_b(T, w_b) = k_B T \, \ln\left[\exp\left(\frac{\hbar^2 \pi w_b}{m_b \, k_B \, T}\right) - 1\right]. \tag{4.8}$$

According to the relaxation rate approximation,[26] it can be assumed that the influence of $\delta f_{\boldsymbol{k}}$ on the scattering rates S^{in} and S^{out} is negligible, i.e. $S^{in}(\rho_{\boldsymbol{k}}) \approx S^{in}(f_{\boldsymbol{k}})$ and $S^{out}(\rho_{\boldsymbol{k}}) \approx S^{out}(f_{\boldsymbol{k}})$. To find an expression for the Coulomb scattering rates finally the previously mentioned Coulomb matrix elements are unserted into eq. (4.5). Unfortunately, the integrals cannot be solved analytically. They are evaluated using the Simpson rule, a numerical method for solving definite integrals by approximating the function by a quadratic polynomial.[45]

Since the efficiency of scattering processes depends on the amount of available scattering partners the scattering rates S_b^{in} and S_b^{out} depend on the wetting layer carrier density w_b. Following fig. 4.2 it is necessary to take the carrier densities of holes and electrons into account for both carrier types' scattering rates since the scattering partner can be electron as well as hole. The electron in-scattering rate S_e^{in}, e.g., is consequently a function of both the electron and hole wetting layer carrier density $S_e^{in}(w_e, w_h)$. However the dynamics of $w_e(t)$ and $w_h(t)$ are similar [20] and their different stationary values suggest the relation $w_e(t) = g_c(j)w_h(t)$ with the ratio coefficient $g_c(j)$, which varies with the injection current density j[46]. During these calculations $g_c = 2.3$ for an injection current density of $1.9 j_{th}$, where j_{th} is the threshold current density. The fact, that the scattering rates can be now calculated as a function of w_e respectively w_h reduces the numerical calculation effort drastically.

A figure with the Coulomb scattering rates for electrons and holes is shown later in the chapter (see fig. 4.5) as a function of the carrier density in the respective wetting layer. The figure shows that the Coulomb scattering rates become larger for increasing wetting layer carrier densities w_b as expected with the increase of available scattering partners. For high w_b the increase is stopped by the Pauli exclusion principle that leads to a maximum in the scattering rates. The effect is more pronounced for the out-scattering processes (fig. 4.5 left axes) and influences the electron scattering rates stronger. The first observation corresponds to the proportionality of the Pauli blocking terms to $(1 - \rho_l^b)(1 - \rho_m^{b'})$, see eq. (4.6). The second one relates on the fact that the hole bands have a smaller curvature (see sec. 1.1.2) and thus the population of hole wetting layer states is distributed over a larger k-range. As a result, the Pauli exclusion principle influences the electrons stronger.

The in-scattering rates are small for low w_b where just a few scattering partners are available and increases with increasing carrier density up to a point

where almost all the wetting layer states are filled and scattering becomes improbable again. The in-scattering rates are proportional to the product of two occupation probabilities in the wetting layer states $\rho_l^b \rho_m^{b'}$, see eq. (4.6). Consequently, they become dominant at higher wetting layer carrier densities at which the out-scattering is already diminished by Pauli blocking.

As mentioned earlier the electron w_e and hole wetting layer carrier density w_h are connected by the relation $w_e(t) = g_c(j) w_h(t)$. The value of $g_c(j)$ has an important influence on the in-scattering rates [46]. For out-scattering processes, the mixed contributions turn out to have an influence on the height of the scattering rates, but less on their qualitative shape, since the out-scattering is only important at low wetting layer densities and decreases strongly right after the maximal value is reached.

4.1.1 T_1 and T_2 times

According to eq. 4.4 the $T_{1,b}$ time determining the decay of the electron and hole population ($b = e, h$), respectively, is given by $(S_b^{in} + S_b^{out})^{-1}$. The T_2 time describes the decay of the coherence. Both times are calculated microscopically using the Boltzmann equation including Auger transitions between wetting layer and quantum dot states. Figure 4.3 shows both times as a function of the wetting layer carrier density w_b.

In agreement with the discussion of the scattering rates in the last section, both $T_{1,b}$ times decrease with increasing w_b, accounting for the stronger Coulomb scattering. The times are the shortest ($\approx 1\,\text{ps}$) in the range of $(1-5) \times 10^{12}\,\text{cm}^{-2}$. Then, the scattering rates are reduced and $T_{1,b}$ increase.

The T_2 time follows the equation

$$
T_2 = \left[\frac{2\pi}{\hbar} \sum_{k_1 k_2 k_3 b'} \left(|W_{h\boldsymbol{k}_1,\, b'\boldsymbol{k}_3}^{h0,\, b'\boldsymbol{k}_2}|^2 \; \delta(\varepsilon^e + \varepsilon_{\boldsymbol{k}_2}^{b'} - \varepsilon_{\boldsymbol{k}_3}^h - \varepsilon_{\boldsymbol{k}_1}^{b'}) - |W_{e\boldsymbol{k}_1,\, b'\boldsymbol{k}_3}^{e0,\, b'\boldsymbol{k}_2}|^2 \right. \right.
$$

$$
\left. \left. \delta(\varepsilon^h + \varepsilon_{\boldsymbol{k}_2}^{b'} - \varepsilon_{\boldsymbol{k}_3}^e - \varepsilon_{\boldsymbol{k}_1}^{b'}) \right) \left(f_{k_1}^{b'} f_{k_3}^e (1 - f_{k_2}^{b'}) + (1 - f_{k_1}^{b'})(1 - f_{k_3}^e) f_{k_2}^{b'} \right) \right]^{-1} \quad (4.9)
$$

that was calculated by Kim et al. [47]. It shows a similar behavior as the $T_{1,b}$ times. After a strong decrease at low wetting layer carrier densities, the T_2 time remains approximately constant ($\approx 2\,\text{ps}$).

The destruction of the coherence (also called dephasing) is known, for conventional three-dimensional systems, to arise from transitions between different states, i.e. from thermalization, energy relaxation, or recombination processes. In quantum dots, however, the dephasing of optical coherence is mainly due to virtual transitions [48]. These do not change the population dynamics. Therefore, this contribution is often called pure dephasing. Since the energy separation between quantum dot states can be few hundreds of meV, the probability for transitions between real states is suppressed, and pure dephasing plays an important role [49]. The dephasing time in quantum dots can be determined experimen-
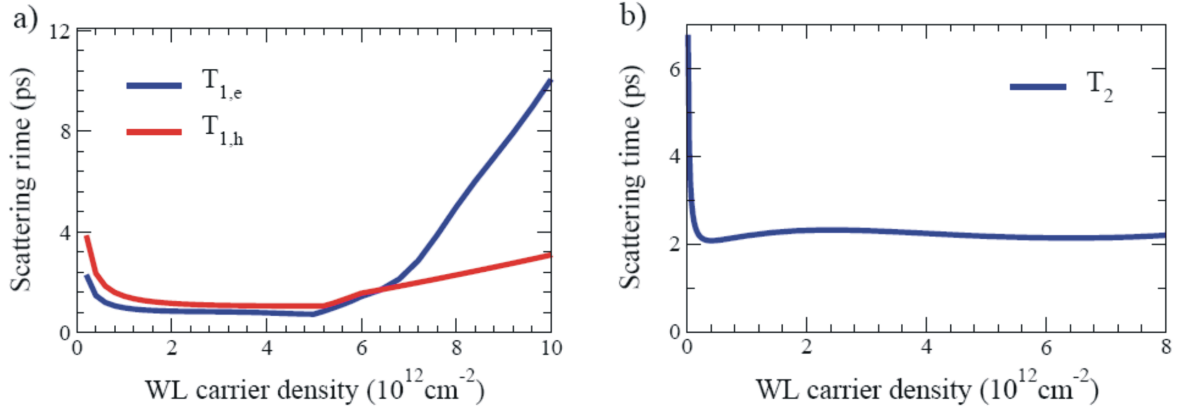
Figure 4.3: (a) The Coulomb scattering times $T_{1,e}$ and $T_{1,h}$ for electrons and holes and (b) the dephasing time T_2 are plotted as a function of the wetting layer carrier density. [20]

tally and lies in the range of picoseconds to femtoseconds and depends on the temperature strongly [50].

The expression for the dephasing time can be separated into a Coulomb scattering related part and a part connected to pure dephasing:

$$\frac{1}{T_2} = \frac{1}{T_{2,\text{scat}}} + \frac{1}{T_{2,\text{pure}}} \, . \tag{4.10}$$

The first term corresponds to the microscopically calculation shown in fig. 4.3b. The second term has been discussed in Lorke et al. [36]. The temperature dependence of the overall dephasing time T_2 is assumed to be guided by the Coulomb part $T_{2,\text{scat}}$. Thus, it is sufficient to obtain the T_2 time for one temperature and then calculate microscopically the corresponding values for other temperatures. Starting from $T_2 = 25\,\text{fs}$, determined experimentally for room temperature, the T_2 times at $350\,\text{K}, 400\,\text{K}, 450\,\text{K}$, and $500\,\text{K}$, are calculated using eq. (4.9), yielding $T_2 = 20\,\text{fs}, 17\,\text{fs}, 15\,\text{fs}, 13\,\text{fs}$, respectively.

4.2 Gain dynamics in model and experiment

Since we want to compare our experimental data to the theoretically achieved, they have to be presented in a similar way. Usually we provide gain curves such as shown in chapter three. Measurements can be performed in dependence of several parameters. We can control the temperature of the device, the injected current and the intensity of the incoming beam. The gain dynamics in quantum dot semiconductor optical amplifiers can be theoretically described by the semiconductor quantum dot Bloch equations (derived in sec. 1.5).

To model the gain dynamics, the absorption coefficient $\alpha(\omega, \tau)$ is calculated as a function of the pulse frequency ω and the delay time τ between the pump and probe pulse. The system is in the gain regime, if the absorption coefficient $\alpha(\omega, \tau)$ is negative, i.e. the imaginary part of the optical susceptibility $\chi(\omega)$. Within the $\boldsymbol{r} \cdot \boldsymbol{E}$ approach the absorption coefficient can be expressed in the frequency space as the ratio between the macroscopic polarization $P(\omega)$ and the electrical field $E(\omega)$

$$\alpha_{pp}(\omega, \tau) \propto \omega Im \left[\frac{P_{\text{pump+probe}}(\omega, \tau) - P_{\text{pump}}(\omega)}{E_{\text{probe}}(\omega)} \right] . \tag{4.11}$$

Key of pump-probe experiments is to measure the changes of the probe signal inflicted by the pump pulse. Therefore, the macroscopic polarization $P_{\text{pump}}(\omega)$ describing the contribution arising from the pump pulse alone needs to be subtracted from $P_{\text{pump+probe}}(\omega, \tau)$ obtained when considering both the pump and the probe pulse. This method gives the response coming from the probe pulse only, but taking into account the influence of the pump pulse [51].

As shown in sec. 1.5, the macroscopic polarization $P(t) = d_{vc}p(t)$ is determined by the optical dipole moment d_{vc} and the microscopic polarization $p(t)$. The first is known from experiments, the second is calculated using the semiconductor Bloch equations.

Within the rotating wave approximation, and for the resonant case with $\hbar\omega = \hbar\omega_{qd} = 0.95\,\text{eV}$ equations of motion for the microscopic polarization $p(t)$, and the quantum dot population probability of electrons $\rho^e(t)$ and holes $\rho^e(t)$ are obtained

$$\dot{p}(t) = -i\Omega(t)[\rho^e(t) + \rho^h(t) - 1] - \frac{1}{T_2}p(t), \tag{4.12}$$

$$\dot{\rho}^e(t) = -2Im[\Omega(t)p^*(t)] - \frac{1}{T_{1,e}}\rho^e(t) + S_e^{in}, \tag{4.13}$$

$$\dot{\rho}^h(t) = -2Im[\Omega(t)p^*(t)] - \frac{1}{T_{1,h}}\rho^h(t) + S_h^{in}. \tag{4.14}$$

Since the carriers are localized completely in the quantum dots the described dynamics is $\boldsymbol{k}$-independent. As mentioned earlier the phonon-coupling will be neglected in eqs. (4.12)-(4.14) due to the fact that the experiments are performed within the gain regime where wetting layer carrier densities are in the range of

$10^{12} - 10^{13}\,\mathrm{cm}^{-2}$ where the Coulomb interaction can be assumed as dominant. However, the influence of phonon induced processes for the dephasing is taken into account during the T_2 time calculation, see sec. 4.1.1. It should be mentioned that in this first study, excitonic effects and memory contribution in the electron-electron scattering are not considered. Since only the region around the resonance is of interest the rotating wave approximation is applicable here. The stationary values before the arrival of the pulse are given by $\rho_0^e(0) = S_e^{in}T_{1,e}$, $\rho_0^h(0) = S_h^{in}T_{1,h}$, and $p_0(0) = 0$.

Then, the gain condition $\rho_0^e(0) + \rho_0^h(0) > 1$ can be expressed in terms of the scattering rates

$$\frac{S_e^{in}}{S_e^{in} + S_e^{out}} + \frac{S_h^{in}}{S_h^{in} + S_h^{out}} > 1 \,. \tag{4.15}$$

The gain condition is independent of the T_2 time, since the stationary values are reached long after the polarization has decayed. All values for the wetting layer carrier densities used in the following meet the gain condition from eq. (4.15) that represents the operation of a quantum dot semiconductor optical amplifier in the gain regime. The strength of the light-matter interaction is given by the Rabi frequency $\Omega(t) = \frac{d_{vc}E(t)}{\hbar}$ with the electrical field $E(t) = E_0 \exp\left(-\frac{t^2}{2\sigma^2}\right)$ and the interband dipole moment d_{vc}, which is set to $0.6\,e_0$nm according to experimental data. The amplitude E_0 determines the pulse area Θ (expressed in units of π)

$$\Theta \equiv \int \Omega(t)dt = \frac{d_{vc}\sqrt{2}\sigma}{\hbar\sqrt{\pi}}E_0 \quad\Longrightarrow\quad E_0 = \frac{\hbar\sqrt{\pi}}{d_{vc}\sqrt{2}\sigma}\Theta \,. \tag{4.16}$$

This definition goes back to the generation of Rabi flops [48]. For a pulse area of $\Theta = 2\pi$, the populations ρ^e and ρ^h are inverted corresponding to one complete Rabi flop. The pump-probe experiment is modeled with two sets of Bloch equations: i) including only the pump pulse and ii) including both the pump and the probe pulse. The length of both pulses is set to $150\,\mathrm{fs}$, and their intensity ratio is $I_{probe}/I_{pump} = 0.01$ in agreement with our experimental setup (see section 1.4 for details).

In general, eqs. (4.12)-(4.14) cannot be solved analytically. The Bloch equations are evaluated numerically using the Runge-Kutta method. In agreement with our experiment, the gain dynamics is calculated for the case that the pulse is in resonance to the quantum dot ground state energy $\omega = \omega_{qd}$, i.e. the gain is given as a function only of the delay time τ. In addition, it is normalized to the value at times long before the pump pulse arrives. In the following the gain dynamics will be discussed and shown in dependence of the temperature T, the wetting layer carrier density w_b, the pulse area Θ, and the dephasing time T_2.

4.2.1 Temperature and wetting layer carrier density dependence

In fig. 4.4 (b) and fig. 4.6 (a) experimental pump-probe curves are shown depending on the temperature and on the injection current respectively. Since the evaluation of the Bloch equations for different temperatures and wetting layer carrier densities is available a comparison with theoretical results is achievable. In fig. 4.4,

the normalized gain is plotted as a function of the pump-probe delay time τ for different temperatures.
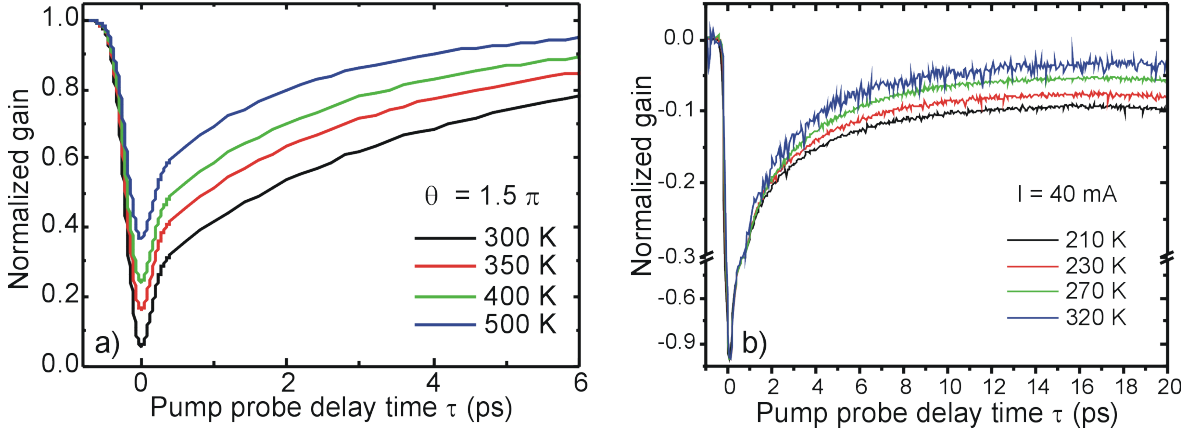

Figure 4.4: Normalized gain as a function of the pump-probe delay time τ for different temperatures. (a) Theoretical calculation for a fixed wetting layer carrier density of $w_e = 5.7 \times 10^{12}\,\mathrm{cm}^{-2}$ (corresponding to the density at which the electron in-scattering S^{in} is maximal). The pulse area is fixed to $\Theta = 1.5\pi$. The gain is calculated for a realistic situation, where the T_2 time varies with the temperature, see Sec. 4.1.1. The T_2 times are 25, 20, 17 and 13. (b) Experimental data taken while controlling the temperature externally.

Taking a look at the general shape of the gain curves the behavior in the first 200 fs is interesting. At first there is a minimum followed by an ultrafast gain recovery on a femtosecond time scale. This effect cannot be explained by Coulomb induced refilling processes, since they are on a picosecond time scale. We explain this characteristic feature of the gain can by the so-called *coherent artifact*, a coherent effect describing the interference between the pump and the probe pulse. The overlap generates a grating in the absorption which scatters a part of the pump pulse in the probe direction. As a result, the probe signal is enhanced. This effect turns out to be sensitive to the dephasing time (following in the next but one section).

In terms of temperature dependence figure 4.4 shows that the gain recovery time is reduced with increasing temperatures for both, experiment and theory. The faster gain recovery can be attributed to the stronger scattering rates at higher temperatures, as shown in fig. 4.5. This leads to a higher efficiency of the refilling process of the quantum dot ground with carriers from the wetting layer, resulting in a shorter gain recovery time. An increase in temperature affects, in particular, the in-scattering processes, since S_b^{in} is proportional to the product of two fermi functions $f_{\boldsymbol{k}_2}^b f_{\boldsymbol{k}_3}^b$, see eq. (4.5). The Fermi distributions become broader at higher temperatures increasing the probability for the capture of charge carriers into the quantum dot ground state. This has a stronger influence on holes due to their larger effective mass and a flatter band structure. A temperature increase of $\Delta T = 200\,\mathrm{K}$ leads to a more than twice as large hole in-scattering rate S_h^{in}. The goal of using semiconductor optical amplifiers for high-speed communication applications asks for a fast gain recovery. Unfortunately an increase in

temperature is not the solution since it does not only speed up the gain recovery but reduces the gain. The optimization of the refilling of quantum dot states leads at the same time to a less pronounced gain peak.
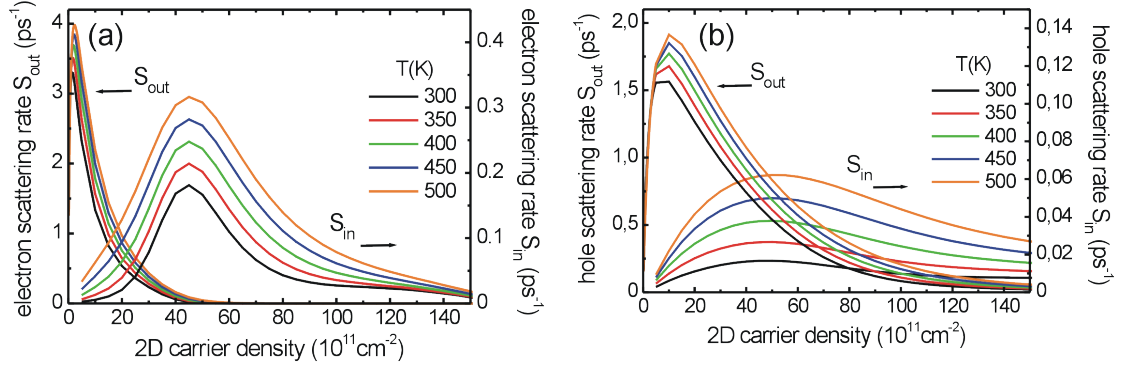

Figure 4.5: Temperature dependence of Coulomb in- out-scattering rates for (a) electrons and (b) holes. Generally, the scattering becomes more efficient with increasing temperatures.

The difference in gain depletion is reduced by approximately 30% at a temperature increase of $\Delta T = 200$ K. This effect is not visible in the experimental data due to a different normalization process. Note that the gain depletion depends only indirectly on the temperature. It is the change of the dephasing time T_2 with the temperature that causes the reduction of the gain depletion (see [20] fig. 4.15 b).
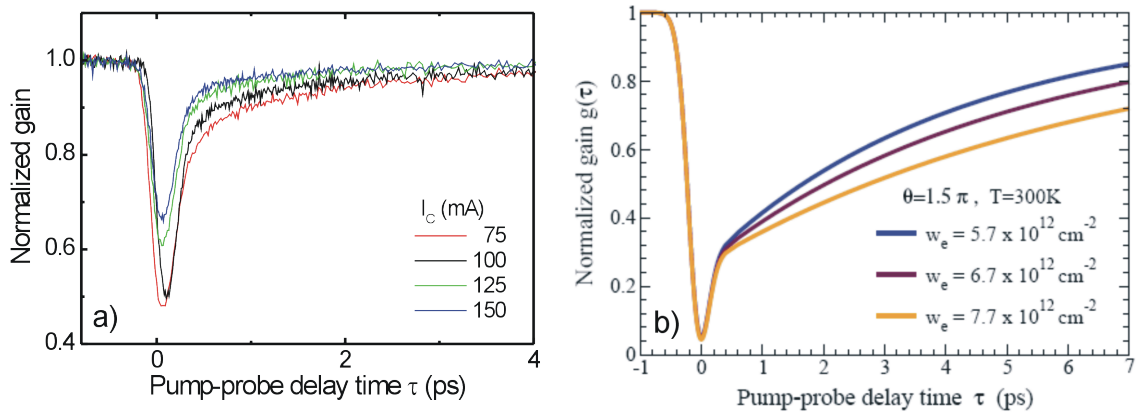

Figure 4.6: Normalized gain as a function of the pump-probe delay time τ. (a) Experimental data for different injection currents I. Unfortunately the injection current changes not only the carrier density but also strongly the temperature as was shown in section 1.4. (b) Theoretical calculation for different wetting layer carrier densities (for a fixed temperature of $T = 300$ K)[20].

The change in temperature for measuring the data in fig. 4.4 (a) was achieved

by controlling the temperature of the device directly. However as shown in sec. 1.4 the increasing injection current changes the temperature as well. This effect, namely the increase of the wetting layer carrier density, is shown in fig. 4.6. Here, the dependence of the normalized gain on the wetting layer carrier density w_e is illustrated and compared with experimental data showing the normalized gain for different injection currents.

The theoretical result feels unexpected at first, with rising w_e, the gain recovery becomes slower. One would expect higher wetting layer carrier densities to be advantageous for a fast gain recovery. However, as already seen in fig. 4.5 the scattering rates have a complex dependence on w_b. At the wetting layer electron density $w_e = 5.7 \times 10^{12}\,\mathrm{cm}^{-2}$, the electron in-scattering rate S_e^{in} has its maximum. For $w_e = 6.7 \times 10^{12}\,\mathrm{cm}^{-2}$ and $w_e = 7.7 \times 10^{12}\,\mathrm{cm}^{-2}$, the capture of electrons via Auger processes is already reduced. The scattering rates increase with increasing wetting layer carrier densities up to a certain value, then they decrease due to Pauli blocking. As a result, fig. 4.6 reflects how efficient the refilling of the quantum dot ground state is. The gain recovery is fastest at $w_e = 5.7 \times 10^{12}\,\mathrm{cm}^{-2}$, where the electron in-scattering is maximal. This effect is not visible in the experimental data due to the fact, that the injected current leads to a strong heating effect (as shown in section 1.4) that masks the effect of pure carrier injection.
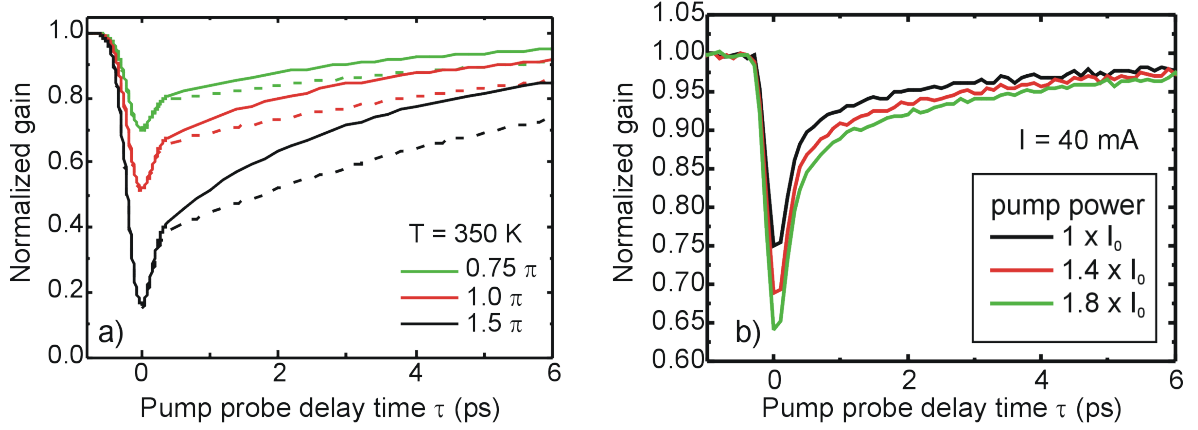
4.2.2 Pulse area dependence

Figure 4.7: Normalized gain as a function of the pump-probe delay time τ. (a) Theoretical calculation for different pulse areas Θ (for a fixed temperature of $350\,\mathrm{K}$ and the wetting layer carrier density $w_e = 5.7 \times 10^{12}\,\mathrm{cm}^{-2}$). In addition the importance of the hole dynamics is illustrated. The dashed lines show the normalized gain under the condition that only the electron dynamics is taken into account. It is clearly seen how important the holes are for a correct simulation of ultrafast gain dynamics. (b) Experimental data for different powers of the probe-beam at a fixed injection current of I=40mA.

Another factor influencing the gain dynamics is the pulse area Θ as defined by eq. 4.16. In fig. 4.7 (a), the normalized gain is shown as a function of the pump-probe delay time τ for three different pulse areas $\Theta = 0.75\pi, 1.0\pi$, and 1.5π. The wetting layer carrier density is fixed to $w_e = 5.7 \times 10^{12}\,\mathrm{cm}^{-2}$, corresponding to the density at which the electron in-scattering S^{in} is maximal. The temperature is set to $350\,\mathrm{K}$ and the corresponding dephasing time T_2 is 20 fs. Figure 4.7 (b) shows experimental data depending on the power of the input-beam that is directly related to the pulse-area. The figure illustrates that the gain depletion is strongly dependent on the input power/ pulse area. Increasing Θ from 0.75π to 1.5π enhances the amplitude of the renormalized gain approximately by a factor of three. Unfortunately, at the same time, the gain recovery is slowed down. Both effects can be seen in the experimental data as well. As with the temperature dependence a choice has to be made between speeding up the gain recovery and reducing the total gain. The optimization of a semiconductor optical amplifier turns out to be a balancing act once again. Note that the absolute refilling time of the quantum dot ground state does not depend on the pulse area. The system needs longer to recover, since the gain reduction at large pulse areas is high.

In addition fig. 4.7 (a) illustrates the importance of taking the dynamics of both electrons and holes into account. The dashed curves show a pure electron dynamics. Considering only electrons leads to strongly reduced in-scattering processes. The capture of electrons described by S_e^{in} is one order of magnitude weaker at the considered wetting layer carrier density of $w_e = 5.7 \times 10^{12}\,\mathrm{cm}^{-2}$ due to the missing efficient electron-hole processes. Consequently, the gain recovery is considerably slowed down. This shows again the importance of holes for the

acceleration of the gain dynamics, which is made allowance for by the p-doping of our device.
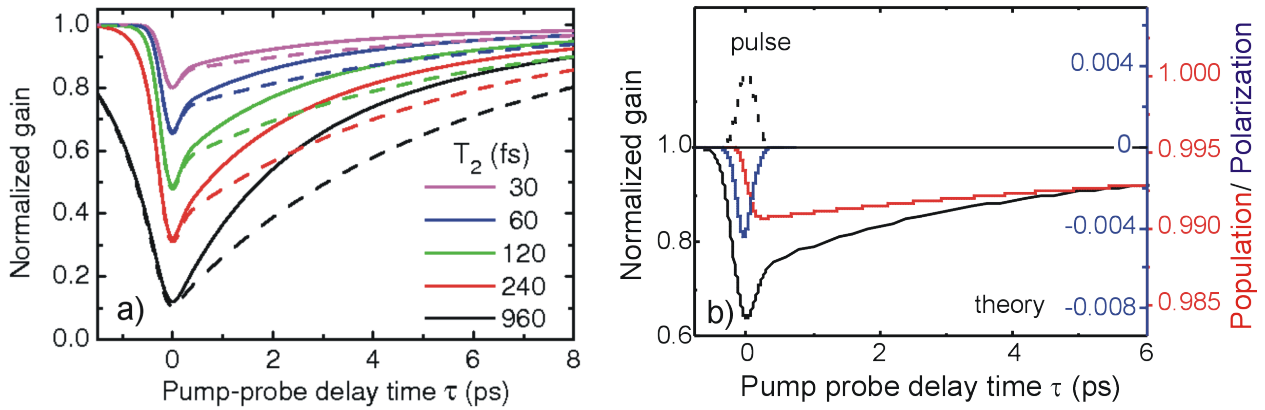

Figure 4.8: (a) Theoretical calculation of the normalized gain as a function of the pump-probe delay time τ for different dephasing times T_2 showing that the characteristic gain peak disappears for long T_2 times. The behavior for negative delay times is ascribed to the optical Stark effect. (b) Illustration of the coupled population and coherence dynamics and their influence on the characteristic gain peak. In the first 200 fs, the gain dynamics is dominated by the coherence, then, the population dynamics is crucial.

Furthermore, fig. 4.7 (a) illustrates that holes have no influence on the gain depletion since the first peak is equal for either solid or dashed lines.
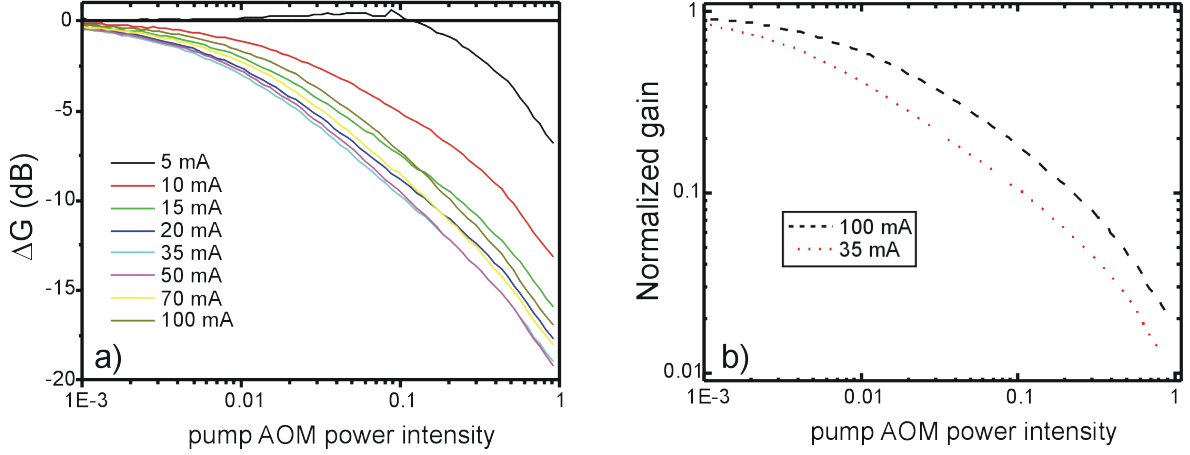
4.2.3   Dephasing time dependence

Figure 4.9: (a) Gain at a delay time of $\tau=0$ (pump and probe arriving at the same time) as a function of the intensity of the pump-beam for different injection currents. (b) Normalized gain at $\tau=0$ as a function of the pump-beam intensity.

The influence of the dephasing time T_2 on the gain dynamics is strongly related with the behavior of the gain curve within the first 200 fs after the arrival of the pump pulse. As can be seen in fig. 4.8 (b), the gain dynamics is composed of a population part and a polarization part. The curve follows the microscopic polarization as long as the pump pulse is present, then it reflects the population dynamics. The gain peak right after the arrival of the pump pulse is strongly influenced by the T_2 time, while the gain recovery time is determined by the $T_{1,e/h}$ times. The interference effects between the pump and the probe pulse at very short pump-probe delay times create the characteristic gain peak that depends strongly on the dephasing time T_2, as shown in fig. 4.8 (a). The pronounced minima only appears if the T_2 time is low enough, i.e. in the order of some femtoseconds - the time scale of the coherence artifact.

After the peak the gain curve possesses a turning point after a delay time of approximately 200 fs, when the influence of the pump pulse is elapsed and the population related gain recovery starts with the capture of carriers from the wetting layer states. The gain peak has been discussed controversially in literature.[52] One widely spread explanation is obtained by including the two-photon absorption. This assumption accounts for the quadratic-like dip in the gain curve within a rate equation approach. However, the dependence of the gain depletion on the injection current does not support this explanation. Furthermore, experiments show that the normalized gain has a linear dependence on the optical pump power over a wide range (see fig. 4.9).

Chapter 5

The rate equation approach

Since the model based on Bloch equations introduced in the last chapter is difficult to connect to experiments due to the lag of being able to measure scattering rates directly the idea of adapting a more simple laser-like rate equation system to the conditions of our experiment arose. We were curious how adequately such a model would reproduce the different time domains of the recovery process.

In the first part of this chapter the model is described in detail. The applied rate equation model describes pump-probe experiments as transient recovery of a steady-state situation after an external optical perturbation. Our goal is to achieve a consistent agreement between laser-theory and optically measured experimental rates. Propagation effects (section 5.1.1) were taken into account and we describe the active medium as a population-inverted system that is forced into a state of non-equilibrium (section 5.1.2). In the second part of the chapter I will explain the analysis of the corresponding experimental results.

5.1   Rate equation model

Our goal was to adjust rate equations developed for the description of lasers and amplifiers to our heterodyne pump-probe measurements with medium to high optical excitation and simultaneous electrical carrier injection. We are mainly interested in a quantitative model of the gain recovery dynamics in a time frame of the first few picoseconds, i. e. the typical region where Coulomb-scattering takes place [38, 53]. We neglected the dynamics of the very first picosecond, that matches the temporal width of the incoming pulse, as well as the late dynamics that correspond to the carrier recombination. For achieving a qualitative description of the ultrafast gain recovery, we developed a simple rate equation system based on the evolution of the carrier population of the confined quantum dot levels and the surrounding 2D-reservoir of carriers formed by the well and the wetting layer. The model emphasizes in addition the following peculiarities of the experimental systems:

Propagation-effects in the waveguide. The intensity of the incoming pulses grows during its guided propagation through the device in gain-mode. Therefore the population is depleted irregularly along the propagation direction.
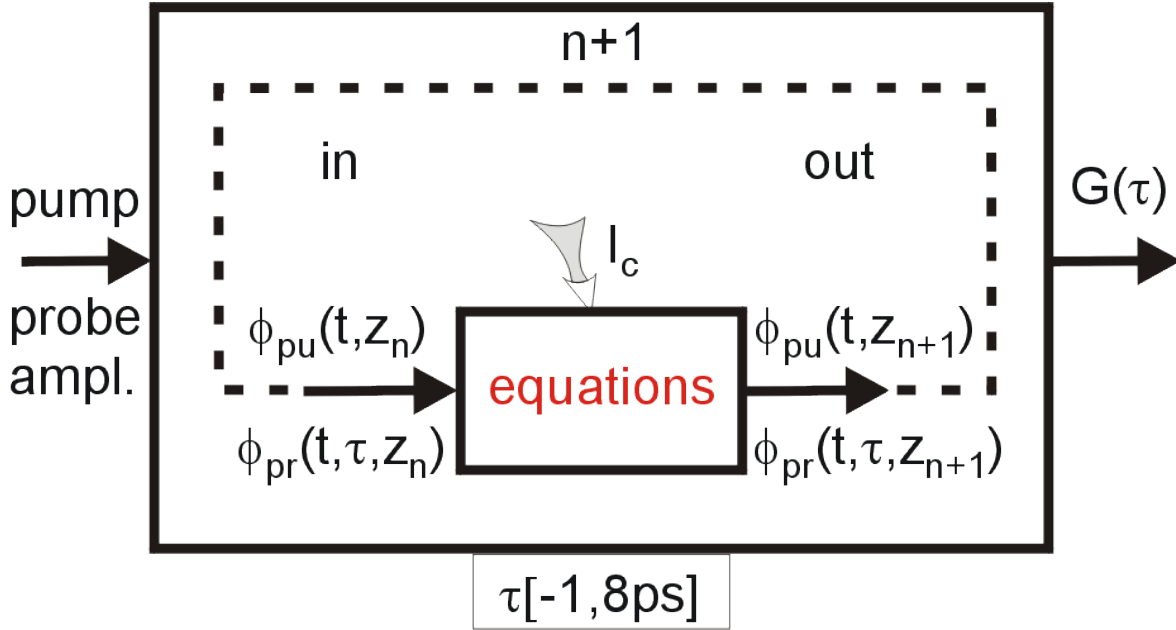
Figure 5.1: Diagram of the iterative numerical treatment used in the proposed model.

The pump-probe experiment is described as *return to the steady-state situation* in an electrical *inverted system* after a perturbation by an external electro-magnetic field.

5.1.1   Propagation effects

Taking into account the inhomogeneous absorption profile we included propagation effects to our model as follows: We divided the waveguide in 200 slices each 5 μm thin perpendicular to the propagation direction. We calculated for a given photon flux through each slice z_n the temporal evolution and the resulting outcoming photon flux ($\phi(t, z_{n+1})$). Subsequently we used the transmitted and amplified photon flux as incoming pulse for the next slice z_{n+1}.

   We took into account two different photon fluxes, pump ($\phi_{pu}(t, z_n)$) and probe ($\phi_{pr}(t, z_n, \tau)$). The initial pump photon flux $\phi_{pu}(0, z_n)$ contains a sum of temporal Gaussians corresponding to the pulse-train experiment. The first Gaussian ist centered at $t = 0$ and provides thus the temporal origin for the simulation.

   The initial probe photon flux, $\phi_{pr}(0, z_n, \tau)$, contains a single Gauss pulse centered at $t = \tau$, i. e. the distance between pump- and probe-pulse. For a fixed delay time τ in an interval τ=[-1, 8], we calculated 30 ps (from t=-1 ps to t=29 ps) of temporal evolution for all 200 slices, following the integration procedure sketch in figure 5.1.

   The experimental result of a pump-probe experiment is the gain (or absorption) achieved by the probe-beam. We calculated this gain $G(\tau)$ following

$$G(\tau) = \frac{\phi_{pr}(\mathrm{n} \cdot l, z_{200}, \tau)}{\phi_{pr}(0, z_0, \tau)} \tag{5.1}$$

where n is the refractive index of GaAs and l the length of the device. This calculation represents in principal the ratio of the transmitted and the initial probe-pulse as a function of the delay time τ. The result is a normalized gain value G_{norm} that can be compared directly with the experimental gain curves once they have been normalized.

5.1.2 Steady-state limit in the inverted quantum dot system

The population inversion in a quantum dot system is determined by the applied injection current, i. e. for a given I_c the carrier distribution of the system is given by the *steady-state equilibrium* between capture-, escape- and spontaneous and stimulated radiative rates among the energy levels. This forced thermal equilibrium induced by I_c is stable and unchanged as long as I_c stays fixed. The short pulse of the probe beam perturbs the equilibrium and forces the electrically inverted population out of the steady-state situation. The pump-probe experiment monitors the return process to the steady-state situation. In our simulation we first calculated the steady-state population without transmission of external light through the device for a fixed injection current I_c. Subsequently we determined the temporal evolution of the pump-probe experiment choosing the initial state of the individual slices to be the one of the steady-state population.

To simplify the model we abstain from using quantum dot Bloch equations instead of rate equations for describing the quantum dot system. We only take into account the population dynamics and neglect the coupled polarization development that takes place in the fs range at room temperature. In the last chapter the polarization dynamics was described using quantum dot Bloch equations.

We defined two subensembles of quantum dots, one with the ground respectively excited state of the quantum dots resonant (rs) and the other one nonresonant (nr) to the energy of the pump and probe pulses. We took the percentage of rs quantum dots from the overlap between the ASE and the pulse spectrum. Both subensembles are usually isolated from each other however they can be thermally coupled through the 2D-reservoir they share. The p-doping of the device gives rise to an excess of holes close to the quantum dots and a built-in population of holes in the quantum dot [54]; therefore we assume that the overall dynamic is governed by the electrons. We created different population equations for both subensembles ($n_{G,E}^{rs,nrs}$). The core of our system is given by the following equation system:

$$
\begin{aligned}
\frac{dn_{2D}}{dt} \;=\; & I_{ec} + S_{G2D}n_G^{rs,nrs} - S_{2DG}\left(2N_{QDs} - n_G^{rs,nrs}\right) \\
& + S_{E2D}n_E^{rs,nrs} - S_{2DE}\left(4N_{QDs} - n_E^{rs,nrs}\right) \\
& - S_{r2D}n_{2D}\,,
\end{aligned} \tag{5.2}
$$

$$\frac{dn_E^{rs,nrs}}{dt} = S_{2DE}(4N_{QDs} - n_E^{rs,nrs}) - S_{E2D}n_E^{rs,nrs}$$

$$- S_{EG}n_E^{rs,nrs}\left(1 - \frac{n_G^{rs,nrs}}{2N_{QDs}}\right)$$

$$+ S_{GE}n_G^{rs,nrs}\left(1 - \frac{n_E^{rs,nrs}}{4N_{QDs}}\right) - S_r n_E^{rs,nrs}, \qquad (5.3)$$

$$\frac{dn_G^{rs,nrs}}{dt} = S_{2DG}(2N_{QDs} - n_G^{rs,nrs}) - S_{G2D}n_G^{rs,nrs}$$

$$- S_{GE}n_G^{rs,nrs}\left(1 - \frac{n_E^{rs,nrs}}{4N_{QDs}}\right)$$

$$+ S_{EG}n_E^{rs,nrs}\left(1 - \frac{n_G^{rs,nrs}}{2N_{QDs}}\right) - S_r n_E^{rs,nrs}$$

$$+ S_{\phi G}(n_G^{rs} - N_{QDs})\phi - S_{coh}n_G^{rs}\phi, \qquad (5.4)$$

$$\frac{d\phi}{dz} = S_{\phi G}(n_G^{rs} - N_{QDs})\phi - S_{coh}n_G^{rs}\phi - \alpha\phi. \qquad (5.5)$$

$n_G^{rs,nrs}$, $n_E^{rs,nrs}$, n_{2D} are the electron population of the ground and excited state as well as the 2D-reservoir population. N_{QDs} is the total number of quantum dots in the observed volume and ϕ corresponds to the entire photon flux traveling through the device. The term I_{ec} stands for the effective induced current that describes the actual part of carriers transmitted into the system formed by the quantum dots and the 2D-reservoir contrary to the total current injected into the device I_c.

Figure 5.2 shows a diagram of the energy levels taken into account in our model. The physical processes marked in figure 5.2 by arrows are represented as rates ($S_{InitialFinal}$, with Initial, Final=G(GS), E(ES) and 2D(2D Reservoir)) in the differential equations system. The particular calculation of the scattering rates was shown in the last chapter including a microscopic approach that takes into account the actual carrier density of the included energy levels [55, 53, 38]. The effective times τ are defined here in relation to the rates S and are used as free parameters for the fitting procedure of the experimental data. Since we were interested mainly in the dynamics of the first picoseconds after the pulse, we treated coherent phenomena that appear during or directly after the pulse arrival as a coherent offset (S_{coh}) in the rate equations. This offset is proportional to the photon flux (ϕ). This simplification bases in the low dephasing time (T_2) that quantum dots experience at temperatures equal or higher than room temperature [56, 50].

S_r is the inverse of the radiative life time τ_r of ground and excited state (suggested to be equal for both states), while S_{r2D} is the inverse of the effective residence time τ_{2D} of the 2D-reservoir.

The capture rates from the 2D-reservoir to the ground state (excited state), $S_{2DG(E)}$, depend on the available electron population in the 2D-reservoir (n_{2D}).
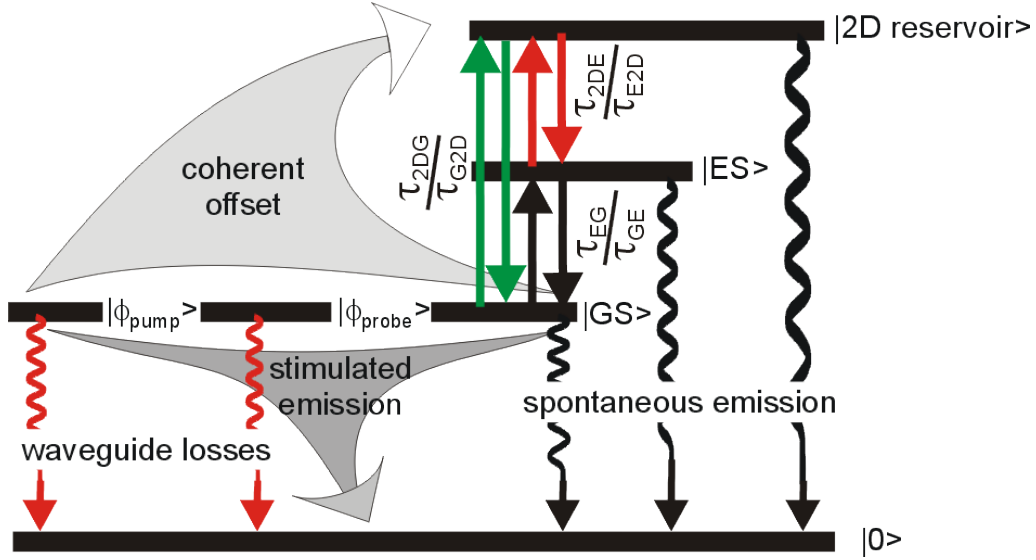
Figure 5.2: Scheme of the InGaAs QD-in-a-well based SOA energy states included in the modelling.

In rate equation models concentrating on regions with low signals and injection currents this term is expressed as $\frac{n_{2D}}{\tau_{2DG(E)}\epsilon N_{QDs}}$, where $\epsilon = 2, 4$ for the ground respectively excited state and $\tau_{2DG(E)}$ represents the capture time from the 2D-reservoir to the ground state (excited state). For high currents however this term leads to rates higher than one ($n_{2D} \gg N_{QDs}$), therefor we approximated the term by

$$S_{2DG} = \frac{1}{\tau_{2DG}}\left(1 - e^{\frac{-n_{2D}}{2N_{QDs}}}\right) \tag{5.6}$$

$$S_{2DE} = \frac{1}{\tau_{2DE}}\left(1 - e^{\frac{-n_{2D}}{4N_{QDs}}}\right) \tag{5.7}$$

This term tends to become 1 for $n_{2D} \gg N_{QDs}$, but recovers the standard form for $n_{2D} \ll N_{QDs}$.

The thermal redistribution of carriers is considered by the escape rates $S_{G(E)2D}$ and S_{GE}. We connected them with the capture rates by introduction of the Boltzmann factor $e^{\frac{\Delta E_{InitialFinal}}{k_B T_c}}$, where T_c is the carrier temperature not to be mistaken wit the device temperature [57, 58, 59].

$$S_{G2D} = \frac{1}{\tau_{2DG}}e^{\frac{\Delta E_{G2D}}{k_B T_c}} \tag{5.8}$$

$$S_{E2D} = \frac{1}{\tau_{2DE}}e^{\frac{\Delta E_{E2D}}{k_B T_c}} \tag{5.9}$$

$$S_{GE} = \frac{1}{\tau_{EG}}e^{\frac{\Delta E_{GE}}{k_B T_c}} \tag{5.10}$$

This terms lead to a thermal steady-state situation as described at the beginning of this section.

The gain-/absorption rate , $S_{\phi G}$, is finally written as:

$$S_{\phi G} = \left(1 - e^{g \cdot \phi}\right) \tag{5.11}$$

with g being the gain/absorption per slice of thickness dz. For $\phi \ll N_{QDs}$ the term represents the usual form $(g \cdot \phi)$ and provides for high photon fluxes no gain rates higher than n_G (after multiplication with the rest of the term), that allows for reproducing the region of high photon luxes given in our experiments.

5.2 Comparison of model and experiment

In this section the rate equation model defined in the last section was applied to systematically analyze the gain dynamics of single-, double- and four-pulse experiments with repetition rates of the input-pulse up to 1 THz. We chose the experimental conditions for the multi-pulse experiments in a way that the energy per pulse was equal for all pulses of the incoming pulse-train at constant I_c. Therefore we were able to fit groups of data (1, 2 and 4 pulse-curves, measured for the same I_c) with a shared parameter-set in a global least-squared minimization routine. This limited the fit to consistent parameter values that can reproduce the observed after-pulse-dynamics.

Part of the parameters used for the simulation were defined by the experimental settings (lower part of table 5.1). We split the analyzes of the experimentally determined data in two parts. In the first one we fitted the data for fixed I_c=35 mA and identified the best fit-parameters (figure 5.3). Table 5.1 shows an overview of these acquired parameter set. After discussing these parameters, we fitted in a second part the remaining measured I_c curves basing on the results of the first part.

Parameter	Value (Units)
τ_{2DG},τ_{2DE}	100 fs
τ_{EG}	500 fs
τ_{rG}, τ_{rE}	445 ps
τ_{r2D}	0.7 ps
Effective injected current I_ec	5 mA
Carrier temperature T_c	403 K
ΔE_{EG}	45 meV
ΔE_{2DG}	210 meV
g (gain in 5μm)	0.125 photons^{-1}
waveguide losses α	5 cm^{-1}
Pump Intensity	0.1 pJ per pulse
Probe Intensity	0.001 pJ per pulse

Table 5.1: Best fit (upper panel) and abinitio fixed (lower panel) parameters used to fit the experimental normalized gain at fixed $I_c = 35$ mA (figure 5.3). $\tau_{InitialFinal}$, where Initial, Final=G(GS), E(ES) and 2D(2D reservoir), are the time constants associated to the process connecting the initial and final energy levels. $\Delta E_{InitialFinal}$, is the energy splitting between the initial and final electron levels.

The fast capture rates τ_{2DG} and τ_{2DE}, i. e., constant relaxation times from the 2D-reservoir to the ground and excited state, are similar to the τ_1 parameter, determined beforehand as the fast component of the multi-exponential fitting routine that is shown in fig. 3.6 in the last section of chapter three. If using rate equations for description, i. e. neglecting polarization dynamics and focusing only to population dynamics, then the fastest time constant requires to consist with the rate of the direct capture from the 2D-reservoir into the confined states of the quantum dots. The most remarkable result we achieved with our analy-
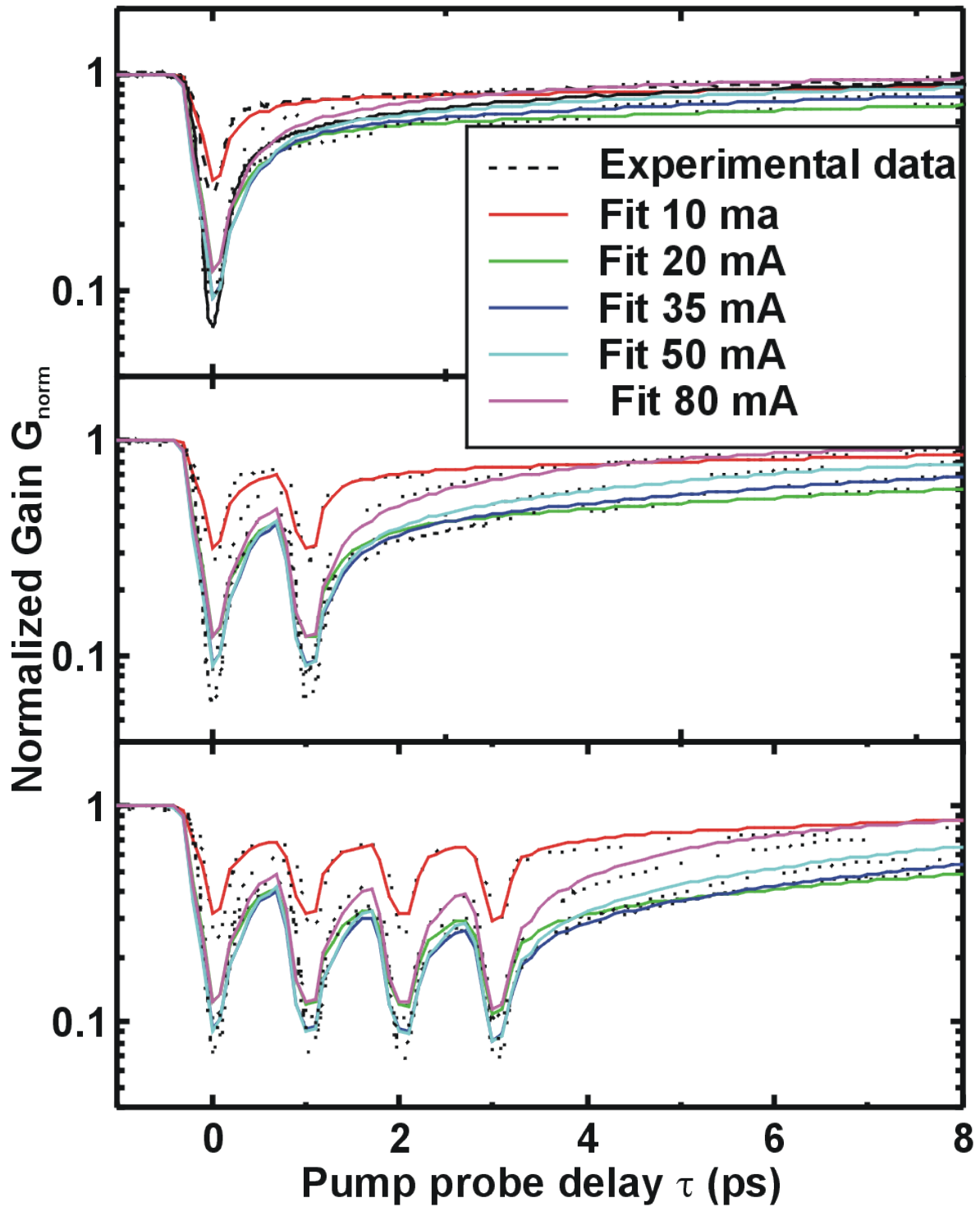
Figure 5.3: Normalized gain curves as a function of I_c measured for 1, 2 and 4 pulses in the train. Solid lines show the corresponding model simulations.

sis is however the fact that a fast τ_{2DG} constant is mandatory to reproduce the experimentally achieved gain recovery of several pulse trains. The continual lowering predicted after multiple pulse trains [3] decreases, if a direct capture into the quantum dot ground state is considered additionally. The time constant τ_{EG}, the relaxation time of the carriers into the quantum dot, is bigger than τ_{2DG} and τ_{2DE}. This fact leads us again to the conclusion that scattering processes that involve carriers not confined at the quantum dots dominate.

Finally I would like to emphasize that the variation of the temperature is important to achieve a satisfying fit, which is a clear hint to a thermal non-equilibrium situation. The calculated values are higher than the temperature of the device (figure 1.19), as could be expected for an electrically pumped system. Nevertheless, this needs further studies. Maybe the thermalization in pulsed experiments is for short times below the recombination lifetime not complete and $T_{carriers} > T_{equilibrium}$ holds within the device.

The time constants τ_{rG} and τ_{rE} are compatible with typical radiative quantum dot lifetimes but their value can be influenced by the amplification processes the spontaneous emission experiences in the waveguide. In addition the fitting showed that only $\sim 15\%$ of the total injected current enters the quantum dot 2D-reservoir system. The main parameter to reproduce the experimental variation of I_c is obviously the effective current I_{ec}.

A variation of the injection current I_c has further effect on the device properties:

The temperature of the device depends on I_c, as can be seen in figure 1.19 and leads to an non-equilibrium situation of the carrier temperature T_c.

The effective residence time of the carriers in the 2D-reservoir τ_{r2D} depends on the current-induced carrier drift and the related change in the wetting layer degeneracy, that is a function of the temperature too [60].

I_c affects τ_{2DG}, τ_{2DE} and τ_{EG} by change of the carrier density (n_G, n_E and n_{2D}).

To study the influence of I_c to the experimental results more carefully, we simulated the gain curves for several different injection currents I_c using only three free parameters: I_{ec}, T_c and τ_{r2D} whereas τ_{2DG}, τ_{2DE} and τ_{EG} were fixed at the values achieved for I_c=35 mA (table 5.1). Fits for 1, 2 and 4 pulse trains are shown in figure 5.3 for different injection currents. It is quite visible that our model satisfyingly represents the pulse amplification process of the semiconductor optical amplifier; this taking into account only experimental data of the ultrafast experiment and a small amount of parameters that represent the actual operation of the device. Note that our model does not reproduce half of the first picosecond after pulse arrival because we treated coherent processes from the start just as an coherent offset. A much more detailed discussion of the early time region can be found in the last chapter based on semiconductor quantum dot Bloch equations and specific T_2 measurements as a function of I_c.

Figure 5.4 shows the best-fit parameters of our systematic analysis. Apparently our model provides further valuable informations, as e. g. the average population of the thermal equilibrium, i. e. in advance of the arrival of the optical probe beam (pump-probe delay $\tau < 0$). We achieved the average population
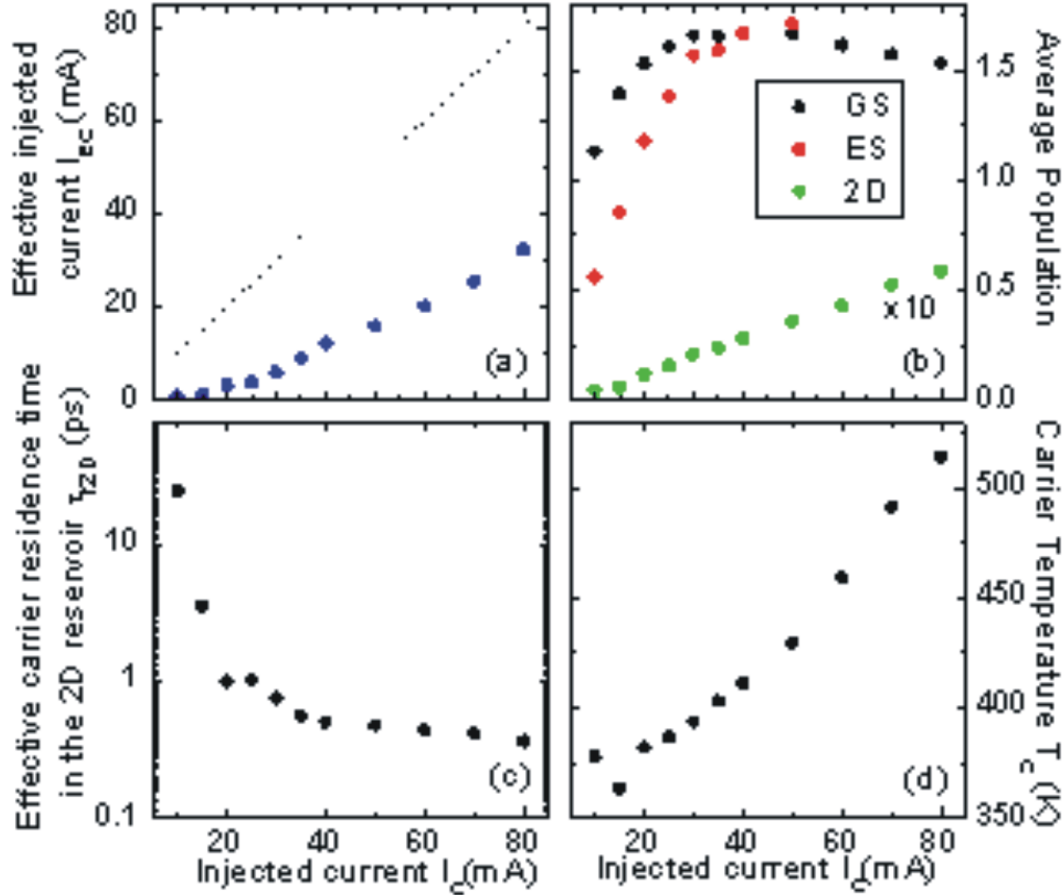
Figure 5.4: (a) Effective injected current I_{ec} (scattered points), (b) Average population per quantum dot in the system (n_G, n_E and n_{2D}), (c) Effective lifetime in the 2D reservoir τ_{r2D} and (d) Carrier Temperature T_c, versus the experimental injected current I_c to the device. Dashed dot line in (a) is an eye-guideline $y = I_c$

of the ground state n_G as well, that increases with the current but saturates at 1.5 excitons per dot (2 corresponds to the maximum degeneracy of the ground state). The thermal carrier redistribution reduces the maximum achievable gain [61]. The general trend of the data approves that the dynamics is governed by the total injected current rather than by the average population of the highest energy level. As expected we can describe the normalized gain evolution qualitatively by adjusting the induced current and its effect to the device.

Though the rate equation approach looks appropriate as a first approximation, I want to point out that scattering rate calculations, accomplished for similar 2D-reservoir carrier densities, predict slightly lower values for this process [46]. This can be attributed to the neglect of the dephasing that was taken into ac-

count in the model of the previous chapter. In that model on the other hand no propagation effects were included, i.e. the population was assumed to be homogeneous throughout the length of the device. It is obvious that there is plenty of improvement to be done yet for both models that will be accomplished in future work.

Summary and outlook

In the framework of this thesis the gain recovery of a quantum dot semiconductor optical amplifier was studied using ultrafast pump-probe spectroscopy. We were able to show that the device we used suffices the needs of modern optical communication networks speaking in first place of the speed of pulse-transmissions.

Extended measurements of up to four-pulse-trains measurements were performed and different methods to achieve such trains were shown starting from simple pulse shapers over amplitude modulation with a phase mask to a two-stage Michelson interferometer.

We proved the complete gain recovery of the quantum dot ground state after the amplification of a 200 GHz double pulse. This shows that there are no physical obstacles for high rate operations of semiconductor optical amplifiers. The results indicate that the relaxation dynamics is guided by direct capture processes from the environment of the quantum dot, i.e. the well and the wetting layer.

A model using optical Bloch equations as well as a laser-like rate-equation model were used to discuss the experiments. The first is a microscopic description with coupled polarization- and population-dynamics in a thermal non-equilibrium situation. It uses semiconductor quantum dot Bloch equations including microscopically calculated Coulomb scattering rates. The latter describes the population dynamics as a recovery process of a forced steady-state situation after an optical induced perturbation.

It is confirmed that the gain dynamics is governed by the overall injected current rather than by the population of the higher energy states. We found that phonon-induced dephasing and a heated carrier population in the 2D-continuum are crucial for the quantum dot-gain recovery and that the initial subpicosecond dynamics is governed by the optical pump-pulse area and small T_2 times as well.

The necessity for rebuilding our setup gives us the opportunity to create it in a way that lets us take influence in the pump- and probe-arm of the setup separately allowing for example two color-experiments, i.e. having a different wavelength for pump- and probe-beam. In addition it gives us the possibility of creating pulse-trains only as a pump leaving us a higher range of power to experiment with. We also plan on doing polarization-dependent measurements

and more temperature related studies are up to come.

A combination of the effects taken into account by each of the two models presented in this work could lead to a great improvement in the agreement between experiment and theory. Of course we will provide the data for comparison, looking forward to deeper understanding of coherent and incoherent processes related to gain dynamics.

The knowledge gained for improving devices by e.g. p-doping will provide us with a new generation of amplifiers on our way to contribute in creating whole optical communication networks for the future applications.

Bibliography

[1] N. G. Basov, O. N. Kroklin, and Y. M. Popov. Production of negative-temperature states in p-n-junctions of degenerate semiconductors. *JETP Lett.*, 78(3):276, 1961.

[2] R. N. Hall, G. E. Fenner, J. D. Kingsley, T. J. Soltys, and R. O. Carlson. Choherent light emission from GaAs junctions. *Phys. Rev. Lett.*, 9:366, 1962.

[3] Tommy W. Berg, Svend Bischoff, Ingibjorg Magnusdottir, and Jesper Mørk. Ultrafast gain recovery and modulation limitations in self–assembled quantum–dot devices. *IEEE Photon. Techn. Lett.*, 13(6):541–543, 2001.

[4] J. Bloch, J. Shah, W. S. Hobson, J. Lopata, and S. N. G. Chu. Room–temperature $1.3\mu m$ emission from InAs quantum dots grown by metal organic chemical vapor deposition. *Appl. Phys. Lett.*, 75:2199, 1999.

[5] Kenichi Nishi, Hideaki Saito, Shigeo Sugou, and Jeong-Sik Lee. A narrow photoluminescence linewidth of 21meV at $1.35\,\mu m$ from strain reduced InAs quantum dots covered by $in_{0.2}ga_{0.8}as$ grown on GaAs substrates. *Appl. Phys. Lett.*, 74:1111, 1999.

[6] Gyoungwon Park, Oleg B. Shchekin, Diana Huffaker, and Dennis G. Deppe. Low-threshold oxide-confined 1.3-μm quantum-dot laser. *IEEE Photon. Tech. Lett.*, 13:230, 2000.

[7] G.Eliseev, H. Li, G. T. Liu, A. Stintz, T. C. Newell, L. F. Lester, and K. J. Malloy. Gound-state emission and gain in ultralow-threshold InAs-InGaAs quantum-dot lasers. *IEEE J. Sel. Topics Q. El.*, 7:135, 2001.

[8] N. Kirstaedter, O. G. Schmidt, N. N. Ledentsov, D. Bimberg, V. M. Ustinov, A. Yu. Egorov, A. E. Zhukov, M V. Maximov, P. S. Kop'ev, and Zh. I. Alferov. Gain and differential gain of single layer InAs/GaAs quantum dot injection lasers. *Appl. Phys. Lett*, 69:1226, 1996.

[9] Landolt-börnstein, zahlenwerte und funktionen aus naturwissenschaft und technik. In O. Madelung, editor, *Neue Serie, Gruppe III und III-V Halbleiter*, volume 17 a. Springer Verlag, Berlin, Heidelberg, New York, 1982.

[10] Y. Masumoto and T. Takagahara. *Semiconductor Quantum Dots.* Springer Verlag, Berlin, Heidelberg, New York, 2002.

[11] A. E. Zhukov, A. R. Kovsh, N. A. Maleev, S. S. Mikhrin, V. M. Ustinov, A. F. Tsatsul'nikov, M. V. Maximov, B. V. Volovik, D. A. Bedarev, Yu. M. Shernyakov, P. S. Kop'ev, Zh. I. Alferov, N. N. Ledentsov, and D. Bimberg. Long–wavelength lasing from multiply stacked InAs/InGaAs quantum dots on GaAs substrates. *Appl. Phys. Lett.*, 75:1926, 1999.

[12] P. Borri, W. Langbein, J. Mørk, and J. M. Hvam. Heterodyne pump–probe and four–wave mixing in semiconductor optical amplifiers using balanced lock–in detection. *Optics Commun.*, 169:317, 1999.

[13] K. L. Hall, G. Lenz, E. P. Ippen, and G. Raybon. Heterodyne pump-probe technique for time-domain studies of optical nonlinearities in waveguides. *Optics Letters*, 17(14):874, 1992.

[14] A. Yariv. *Quantum Electronics*. John Wiley & Sons, Inc, 1988.

[15] B. L. Schumaker. Noise in homodyne detection. *Optics Lett.*, 9:189, 1984.

[16] S. Schneider. *Carrier dynamics in electrically pumped semiconductor quantum dot amplifiers*. PhD thesis, Universität Dortmund, 2004.

[17] T. Kuhn. *Density Matrix Theory of Coherent Ultrafast Dynamics in Theory of Transport Properties of Semiconductor Nanostructures, ed. by E. Schöll.* Champman & Hall, 1998.

[18] P. Meystre and M. Sargent. *Elements of Quantum Optics*. Springer, 1990.

[19] C. Cohen-Tannoudji, B. Diu, and R. Laloe. *Quantum Mechanics*, volume 1. Wiley, 1977.

[20] E. Malic. *Many-particle theory of optical properties in low-dimensional nanostructures. Dynamics in single-walled carbon nanotubes and semiconductor quantum dots*. PhD thesis, Technische Universität Berlin. Institut für Theoretische Physik, 2008.

[21] W. Nolting. *Quantenmechanik*, volume 5.2. Zimmermann-Neufang, 1993.

[22] M. Lindberg and S. W. Koch. Effective bloch equations for semiconductors. *Phys. Rev. B*, 38(5):3342, 1988.

[23] J. Fricke. Transparent equations including many-particle correlations for an arbitrary quantum system: A general formalism. *Annals of Physics*, 252(142):478–498, 1996.

[24] J. Förstner I. Waldmüller and A. Knorr. *Self-Consistent Projection Operator Theory of Intersubband Absorbance in Semiconductor Quantum Wells, ed. by E. Schöll.* Springer, 2004.

[25] H. Haken. *Light and Matter*, volume 2. BI Wissenschaftsverlag, 1995.

[26] W. W. Chow, S. W. Koch, and M. Sargent. *Semiconductor-Laser Physics*. Springer, 1994.

[27] Yu. A. Il'inskii and L. V. Keldysh. *Electromagnetic Response of Material Media.* Springer, 2007.

[28] E. Hecht. *Optik.* Oldenbourg, 2001.

[29] Phasenmaske SLM-S 640/12. *Software Documentation.* Jenoptik, 2001.

[30] D. Meshulach, D. Yelin, and Y. Silberberg. Adaptive real-time femtosecond pulse shaping. *J. Opt. Soc. Am. B*, 15:1615, 1998.

[31] J. Urayama, T. B. Norris, J. Singh, and P. Bhattacharya. Observation of phonon bottleneck in quantum dot electronic relaxation. *Phys. Rev. Lett.*, 86:4930, 2001.

[32] K. L. Hall, G. Lenz, A. M. Darwish, and E. P. Ippen. Subpicosecond gain and index nonlinearities in InGaAsP diode lasers. *Optics Commun.*, 111(5-6):589, 1994.

[33] P. Borri, W. Langbein, J. M. Hvam, F. Heinrichsdorff, M.-H. Mao, and D. Bimberg. Ultrafast gain dynamics in InAs/InGaAs quantum dot amplifiers. *IEEE Photon. Technol. Lett.*, 12(6):594, 2000.

[34] P. Borri, W. Langbein, J. M. Hvam, F. Heinrichsdorff, M.-H. Mao, and D. Bimberg. Spectral hole-burning and carrier-heating dynamics in quantum-dot amplifiers. *IEEE J. Sel. Topics Quantum Elect.*, 6(3):544, 2000.

[35] A. Wacker R. Wetzler and E. Schöll. Coulomb scattering with remote continuum states in quantum dot devices. *J. Appl. Phys.*, 95(12):7966–7970, 2004.

[36] et al. M. Lorke. Influence of carrier-carrier and carrier-phonon correlations on optical absorption and gain quantum-dot systems. *Phys. Rev. B*, 73:085324, 2006.

[37] D. Bimberg, M. Grundmann, and N. N. Ledentsov. *Quantum Dot Heterostructures.* John Wiley and Sons, Chichester, 1999.

[38] P. Gartner T. Nielsen and F. Jahnke. Many-body theory of carrier capture and relaxation in semiconductor quantum-dot lasers. *Phys. Rev. B*, 69(23):235314, 2004.

[39] M. Grundmann O. Stier and D. Bimberg. Electronic and optical properties of strained quantum dots modeled by 8-band k.p theory. *Phys. Rev. B*, 59(8):5688–5701, 1999.

[40] S. Fafard A. Wojs, P. Hawrylak and L. Jacak. Electronic structure and magneto-optics of self-assembled quantum dots. *Phys. Rev. B*, 54(8):5604–5608, 1996.

[41] W. W. Chow H. C. Schneider and S. W. Koch. Influence of coupling between localized and continuum states in ingan quantum-dot systems. *Phys. Status Solidi (b)*, 238(3):589–592, 2003.

[42] F. Rossi and T. Kuhn. Theory of ultrafast phenomena in photoexcited semi-conductors. *Rev. Mod. Phys.*, 74(3):895, 2002.

[43] M. Mosko and A. Moskova. Echange carrier-carrier scattering of spin-polarized 2-dimensional electron-hole plasma - monte carlo study. *Semicond. Sci. Technol.*, 9(5):478–481, 1994.

[44] H. Haug and S. W. Koch. *Quantum Theory of the Optical and Electronic Properties of Semiconductors*. World Scientific, 2004.

[45] W. T. Vetterling W. H. Press, S. A. Teukolsky and B. P. Flannery. *Numerical Recipes in C: The Art of Scientific Computing*. Cambridge University Press, 1992.

[46] E. Malic P. Hoevel M. Kuntz D. Bimberg A. Knorr K. Luedge, M. J. P. Born-mann and E. Schoell. Turn-on synamics and modulation response in semi-conductor quantum dot lasers. *Phys. Rev. B*, 78:35316, 2008.

[47] J. Kim, Ermin Malić, Marten Richter, and Andreas Knorr. in preparation, 2008.

[48] J. Danckwerts J. Förstner, C. Weber and A. Knorr. Phonon-assisted damp-ing of rabi oscillations in semiconductor quantum dots. *Phys. Rev. Lett.*, 91:127401, 2003.

[49] T. Kuhn I. D'Amico B. Krummheuer, V. M. Axt and F. Rossi. Pure de-phasing and phonon dynamics in GaAs- and GaN-based quantum dot struc-tures: Interplay between material parameters and geometry. *Phys. Rev. B*, 71(23):235329, 2005.

[50] S. Schneider U. Woggon R. L. Sellin D. Ouyang P. Borri, W. Langbein and D. Bimberg. Exciton relaxation and dephysing in quantum-dot amplifiers from room to cryogenic temperature. *IEEE J. Sel. Top. Quatum Electron.*, 8(5):984, 2002.

[51] T. Renger M. Richter and A. Knorr. A bloch equation approach to intensity dependent optical spectra of light harvesting complex ii. *Photosynth. Res.*, 95:119–127, 2008.

[52] J Mork and A. Mecozzi. Theory of the ultrafast optical response of active semiconductor waveguides. *J. Opt. Soc. B*, 13(8):1803–1816, 1996.

[53] M. Kuntz D. Bimberg A. Knorr E. Malic, M. J. P. Bornmann and E. Schoell. Coulomb damped relaxation oscillations in semiconductor quantum dot lasers. *IEEE J. Sel. Topics in Quantum Electron.*, 13(5):1242, 2007.

[54] B. C. Lee K. W. Sun, A. Kechiantz and C. P. Lee. Ultrafast carrier capture and relaxation in modulation-doped inas quantum dots. *Appl. Phys. Lett.*, 88(16):163117, 2006.

[55] M. J. P. Bornmann P. Hoevel E. Schoell A. Knorr M. Kuntz E. Malic, K. J. Ahn and D. Bimberg. Theory of relaxation oscillations in semiconductor quantum dot lasers. *Appl. Phys. Lett.*, 89(10), 2006.

[56] S. Schneider U. Woggon R. L. Sellin D. Ouyang P. Borri, W. Langbein and D. Bimberg. Rabi oscillations in the excitonic ground-state transition of ingaas quantum dots. *Phys. Rev. B*, 66(8), 2002.

[57] H. Jiang and J. Singh. Nonequilibrium distribution in quantum dot lasers and influence on laser spectral output. *J. Appl. Phys.*, 85(10):7438, 1999.

[58] O. Gauthier-Lafaye J. Provost C. Paranthoen A. Markus, J. Chen and A. Fiore. Impact of intraband relaxation on the performance of a quantum-dot laser. *IEEE J. Sel. Topics in Quantum Electron.*, 9(5):1308, 2003.

[59] A. Bilenca and G. Eisenstein. On the noise properties of linear and non-linear quantum-dot semiconductor optical amplifiers: The impact of inhomogeneous broadened gain and fast carrier dynamics. *IEEE J. Quantum Electron.*, 40(6):690, 2004.

[60] D. Deppe and H. Huang. Fermi's golden rule, nonequilibrium electron capture from wetting layer and the modulation response in p-doped quantum-dot lasers. *IEEE J. Quantum Electron.*, 42(3-4):324, 2006.

[61] D. R. Matthews, H. D. Summers, P. M. Smowton, and M. Hopkinson. Experimental investigation of the effect of wetting layer states on the gain-current characteristics of quantum-dot lasers. *Appl. Phys. Lett.*, 81(26):4904, 2002.

Acknowledgments

For different reasons I have to thank namely Dr. Michael Gerbracht, Peter Karbach, Pilar Descalzo López, Dr. Stephan Schneider and Dr. Gerhard Ordner.

A special thank goes to my family, who helped me a lot in finding my own way and finally reaching this important step in my live. Danke an meine Eltern Elisabeth und Detlef Dommers, meine Schwester Andrea Baldus, an Gerti Sprock, Walli und Heinz Dommers, Barbara Wolff, Barbara und Georg Sprock, Michael und Dagmar Dommers, Rosi und Detlef Liebchen, Rene Baldus, Christian, Chrissy, Steffi, Danny und Carl.

Last but not least I want to thank my husband Stefan Völkel for sharing this part of my live with me and supporting me all the time. I hope to be able to give something back.